PART I

TEMPERATURE DEPENDENCE OF SINGLE CRYSTAL SPINEL ($MgAl_2O_4$) ELASTIC CONSTANTS FROM 293K TO 423K MEASURED BY LIGHT-SOUND SCATTERING IN THE RAMAN-NATH REGION

PART II

EFFECT OF ANELASTICITY ON PERIODS OF EARTH'S FREE OSCILLATION (TOROIDAL MODES)

Thesis by

Hsi-Ping Liu (劉希平)

In Partial Fulfillment of the Requirements

For the Degree of

Doctor of Philosophy

California Institute of Technology

Pasadena, California

1974

(Submitted April 4, 1974)

ACKNOWLEDGMENTS

First of all, the author wishes to acknowledge the constant support given to him by Professor Don L. Anderson during the entire course of this work. Professor Amnon Yariv's course on Quantum Electronics and Dr. Richard MacAnally's course on Modern Optics Laboratory provided the author with the basic tools for the experiment. Discussions with Dr. Richard MacAnally also helped the author in forming the basic method of the measurements. Professor Nicholas George provided the use of a Joyce-Loebl microdensitometer for data readout. Professor W. B. Daniels of Princeton University kindly permitted the author to build a 10 kb handpump originally designed by him. Professor William T. Doyle of Dartmouth College, the author's former Master's thesis advisor, provided the detailed drawings for this handpump. Dr. R. N. Schock of the University of California Lawrence Livermore Laboratory generously loaned the author the optical cell for the pressure dependence measurement. The author benefited in learning some high pressure techniques while working with him to seal the optical cell. Dr. Schock also did the data readout for the pressure dependence measurements. Professor Hiroo Kanamori checked the final results as well as the readout procedure of the experiment. Professor E. K. Graham of Pennsylvania State University oriented the spinel sample for his ultrasonic measurements while a research fellow at Caltech, and supplied the author with the X-ray orientation data. Encouragement from Dr. Charles G. Sammis, now at Pennsylvania State University, also benefited the author. Professor Charles B. Archambeau suggested the topic for the

second part of this thesis and checked the results of derivations and numerical calculations. Dr. Thomas Jordan, now at Princeton University, provided the author with the computer program calculating displacement field and angular frequency of Earth's toroidal oscillations. The author wishes to express sincere thanks to the various assistances provided by these individuals.

Equal thanks are due to the competent technical staff at the Seismological Laboratory, notably the machine shop crew, Messrs. Mott Hudson and Dick Wicks, headed by Mr. Elmer Steffensen, with whom the author has worked closely. Messrs. Jo Galvan, Bill Barber and Laszlo Lenches drafted the figures and Mrs. Ruth A. Stratton typed the manuscript.

The research was supported by NASA under Grant #NGL05-002-069, Sup. 5, and by American Petroleum Institute under API Research Project III.

ABSTRACT

Part I

The temperature dependence of single-crystal elastic constants of synthetic stoichiometric $MgAl_2O_4$ spinel has been measured by the light-sound scattering technique in the Raman-Nath region. The crystal is set into forced vibration by a single crystal $LiNbO_3$ transducer coupled to one crystal face. A He-Ne laser beam is diffracted by the stress-induced birefringence inside the crystal. The diffraction angle is determined from the distance of two spots exposed on a photographic plate by the first order diffracted beams as measured by a microdensitometer. The sound wavelength inside the crystal is then inferred from the laser diffraction angle. Combining the sound wavelength with the measured transducer driving frequency, the velocity inside the crystal is determined typically to a precision of 0.05%. In this method, the measurement of velocity is not dependent on either the determination of sample length or on phase shifts at sample-transducer interface. Velocities of four pure modes, L//[001], T//[001], L//[110], and T//[110] (P//[1$\bar{1}$0]) are measured in the temperature range between 293K and 423K. A linear temperature dependence is fit to the data by a least square method. Values obtained at 25°C from this linear fit are $V_p[001] = 8.869 \pm 0.013$ km/sec, $(\frac{\partial V}{\partial T})_p = -(3.14 \pm 0.13) \times 10^{-4}$km/sec-K; $V_s[001] = 6.5666 \pm 0.0055$ km/sec, $(\frac{\partial V}{\partial T})_p = -(1.47 \pm 0.10) \times 10^{-4}$km/sec-K; $V_p[110] = 10.199 \pm 0.011$ km/sec, $(\frac{\partial V}{\partial T})_p = -(3.20 \pm 0.15) \times 10^{-4}$km/sec-K; $V_s[110][P//[1\bar{1}0]) = 4.2101 \pm 0.0043$ km/sec, $(\frac{\partial V}{\partial T})_p = -(2.07 \pm 0.06) \times 10^{-4}$km/sec-K. The temperature

dependence of the adiabatic elastic constants and bulk and shear (VRH average) moduli is computed using the density and literature value of thermal expansion coefficient. Values obtained are: $C_{11}^S = 2814 \pm 8$ kb, $(\frac{\partial C_{11}^S}{\partial T})_p = -0.258 \pm 0.018$ kb/K; $C_{12}^S = 1546 \pm 9$ kb, $(\frac{\partial C_{12}^S}{\partial T})_p = -0.107 \pm 0.019$ kb/K; $C_{44}^S = 1543 \pm 3$ kb, $(\frac{\partial C_{44}^S}{\partial T})_p = -0.101 \pm 0.010$ kb/K; $K_S = 1969 \pm 6$ kb, $(\frac{\partial K_S}{\partial T})_p = -0.157 \pm 0.014$ kb/K; $\mu_{VRH} = 1080 \pm 5$ kb, $(\frac{\partial \mu_{VRH}}{\partial T})_p = -0.094 \pm 0.008$ kb/K . A comparison with previous measurements by pulse superposition and ultrasonic interferometry methods is made. Disagreement, when present, is discussed in terms of the separate measuring techniques. An attempt has also been made to measure the pressure dependence of elastic constants of spinel with the same technique. It failed because of the large spurious diffraction introduced by the fluctuation in index of refraction of the pressure fluid. A method to eliminate this spurious effect is discussed. An optical interferometry method is devised to measure the pressure window distortion effect in the pressure dependence measurement. Finally, the present method with its possibility for further improvement is evaluated as a new method to measure temperature and pressure dependence of elastic constants. Other methods using light-sound scattering to measure sound velocities are also reviewed.

Part II

It is known that the anelastic properties of the earth characterized by a "Q" structure will affect the periods of free oscillation. It is generally considered that the effect is negligible compared to

the other perturbing effects due to rotation, ellipticity, and lateral inhomogeneities. Nevertheless, it is of some interest to investigate the precise magnitude of this effect for the observed free oscillation modes since it could provide us with another constraint in the determination of the Q structure of the Earth. An application of perturbation theory provides us with a good estimate of the magnitude of the changes in the periods of an elastic model due to inclusion of anelastic effects. Calculations based on currently accepted elastic and anelastic models for the Earth show that the shift in period due to anelasticity is at most 0.023 percent for the toroidal modes from ${}_oT_2$ to ${}_oT_{99}$, the maximum occurring near ${}_oT_{60}$. This is smaller by a factor of five than the present observational accuracy. Compared to the other perturbing effects, the anelastic effect, when important, is larger than the effect of ellipticity considered alone but smaller by an order of magnitude when compared with ellipticity and rotational effects coupled together or with the continent-ocean lateral inhomogeneity. Since the frequency shift due to anelasticity is scaled by $(1/Q)^2$, the anelastic effect can be within observational accuracy and comparable to other perturbing effects for more extreme, yet acceptable, Q models.

Table of Contents

Part I

Temperature Dependence of Single Crystal Spinel ($MgAl_2O_4$) Elastic Constants from 293K to 423K Measured by Light-Sound Scattering in the Raman-Nath Region

Part II

Effect of Anelasticity on Earth's Free Oscillation Periods (Toroidal Modes)

PART I

TEMPERATURE DEPENDENCE OF SINGLE CRYSTAL SPINEL ($MgAl_2O_4$) ELASTIC CONSTANTS FROM 293K to 423K MEASURED BY LIGHT-SOUND SCATTERING IN THE RAMAN-NATH REGION

1. Introduction

The most accurately determined local parameters in the interior of the Earth are density, compressional velocity, and shear velocity. These are found by inversion of body wave, surface wave, and free oscillation data, e.g., Jordan and Anderson (1974). From the density profile, the pressure at different depths can be calculated using straightforward integration. Temperature estimates for the Earth's interior depend upon assumptions regarding the distribution of heat source, conductivity, and initial and boundary conditions, and are not well determined.

The purpose of laboratory experimental geophysics is to reproduce the pressure and temperature conditions inside the Earth in order to measure the physical properties of various minerals. Together with experimental petrological studies, constraints can then be put on the composition and crystal structures of the material at various depths inside the Earth.

Since sound wave velocities in the Earth are so well determined from seismology, measurement of sound velocities is an important program in experimental geophysics.

Unfortunately, direct measurement of velocities as a function of temperature and pressure is possible only over a limited range of these parameters. To date, the practical limit of pressure measurement is 30 kb (Christensen 1974) and that of simultaneous pressure and temperature measurement is 10 kb and 800K (e.g., Spetzler 1970); the latter condition corresponds roughly to a depth of 30 km.

In order to use measurements of such limited experimental range, averaging schemes to determine sound velocities of aggregates from measured component minerals, extrapolation using lattice dynamics (Sammis 1972), and finite strain theories (Anderson, Sammis and Jordan 1972) must be employed to infer the physical and chemical states at greater depths. As extrapolation is involved in this procedure, the measurement of pressure and temperature dependence of sound velocities must be precise enough to yield meaningful constraints at greater depths. To date, the method with the highest precision for measuring pressure and temperature dependence of sound velocities in solids is by ultrasonic interferometry (McSkimin 1961; McSkimin and Andreatch 1962; Spetzler 1970). Natural rocks, because of porosity and grain boundary scattering of ultrasonic pulse trains, cannot be subjected to this method of measurement. Some artificially sintered polycrystalline samples, notably Al_2O_3 and MgO polycrystalline aggregates, although measurable by this method, show hysteresis when cycled in pressure and temperature. It seems that single crystals are the only samples that can be measured reliably by the method of ultrasonic interferometry, and data on various geophysically important minerals measured by this method already exist (Anderson, Schreiber, Liebermann and Soga 1968; Graham and Barsch 1969; Spetzler 1970; O'Connel and Graham 1971; Frisillo and Barsch 1972; Chang and Barsch 1973).

Although the method of ultrasonic interferometry has very high precision, systematic errors arising from the boundary condition at the crystal-transducer or crystal-buffer rod interface are difficult to

ascertain and measurements on pressure and temperature dependence of sound velocities from different laboratories on the same mineral differ sometimes by as much as 25%. Clearly, this is a basic limitation on extrapolation of laboratory measurements to mantle conditions.

The present work is an attempt to use an independent method, the method of light-sound scattering in the Raman-Nath region, to measure the pressure and temperature dependence of single crystal sound velocities.

The interaction of light and sound in the Raman-Nath region was first observed in liquid by Debye and Sears (1932) and in solid by Schaefer and Bergmann (1934). This method was employed at that time to determine the elastic constants of various crystals and the results are summarized in Bergmann (1954). Their experimental accuracy was limited by the technology at that time which lacked a coherent laser light source, a fast and high resolution photographic plate, and a photographic density readout instrument with high positional accuracy. As a consequence, neither temperature nor pressure dependence of single crystal elastic constants has ever been measured by this technique until the present work.

Temperature dependence of sound velocities in single crystal spinel ($MgAl_2O_4$), chosen because of the availability of high quality synthetic spinel crystal, the existence of previous measurements by ultrasonic interferometry methods, and its geophysical importance, was successfully measured in the present experiment. The temperature dependence of the elastic constants was determined from these data.

The methods and results of these measurements will be described in detail in Sections 3 and 5. Pressure dependence measurements on the same crystal, on the other hand, showed much scatter. The methods used in the pressure measurements, the reasons for the scatter, and a possible technique to reduce the experimental scatter, will be presented in Section 7.

2. Interaction between Light and Sound--A Theoretical Background

The index of refraction ellipsoid in its general form is (Yariv 1968)

$$\left(\frac{1}{n^2}\right)_{xx} x^2 + \left(\frac{1}{n^2}\right)_{yy} y^2 + \left(\frac{1}{n^2}\right)_{zz} z^2 + 2\left(\frac{1}{n^2}\right)_{yz} yz + 2\left(\frac{1}{n^2}\right)_{zx} zx + 2\left(\frac{1}{n^2}\right)_{xy} xy = 1 \quad \text{(I.2-1)}$$

Let $B_{11} \equiv \left(\frac{1}{n^2}\right)_{xx}$, $B_{22} \equiv \left(\frac{1}{n^2}\right)_{yy}$, $B_{33} \equiv \left(\frac{1}{n^2}\right)_{zz}$, $B_{23} \equiv \left(\frac{1}{n^2}\right)_{yz}$, etc., and use the notation $x \to x_1$, $y \to x_2$, $z \to x_3$, $11 \to 1$, $22 \to 2$, $33 \to 3$, $23 \to 4$, $31 \to 5$, $12 \to 6$. Assume also that the indicatrix is diagonalized in the absence of external stress.

In the presence of external stress, the change in $B_{j\ell}$ is

$$\delta B_{j\ell} = \pi_{j\ell mn}\, \sigma_{mn} = p_{j\ell mn}\, \varepsilon_{mn} \quad \text{(I.2-2)}$$

where σ_{mn}: stress tensor, ε_{mn}: strain tensor

$\pi_{j\ell mn}$: piezo-optical coefficients,

$p_{j\ell mn}$: elasto-optical coefficients

Spinel, a cubic crystal belonging to space group O_h^7(Fd3m), has piezo-optical coefficients of the form (Nye 1957)

$$(\pi_{j\ell mn}) = \begin{pmatrix} \pi_{11} & \pi_{12} & \pi_{12} & & & & \\ \pi_{12} & \pi_{11} & \pi_{12} & & & & \\ \pi_{12} & \pi_{12} & \pi_{11} & & & & \\ & & & \pi_{44} & & & \\ & & & & \pi_{44} & & \\ & & & & & \pi_{44} & \end{pmatrix} \qquad \text{(I.2-3)}$$

For example, a uniaxial compressional stress of magnitude σ applied in the x_1-direction would give the change in $(B_{j\ell})$ as

$$\begin{pmatrix} \delta B_1 \\ \delta B_2 \\ \delta B_3 \\ \delta B_4 \\ \delta B_5 \\ \delta B_6 \end{pmatrix} = \begin{pmatrix} \pi_{11} & \pi_{12} & \pi_{12} & & & & \\ \pi_{12} & \pi_{11} & \pi_{12} & & & & \\ \pi_{12} & \pi_{12} & \pi_{11} & & & & \\ & & & \pi_{44} & & & \\ & & & & \pi_{44} & & \\ & & & & & \pi_{44} & \end{pmatrix} \begin{pmatrix} \sigma \\ 0 \\ 0 \\ 0 \\ 0 \\ 0 \end{pmatrix} \qquad \text{(I.2-4)}$$

which implies

$$\begin{aligned} \delta n_1 &= -\tfrac{1}{2}(n^o)^3\, \delta B_1 = -\tfrac{1}{2}(n^o)^3 \pi_{11}\sigma \\ \delta n_2 &= \delta n_3 = -\tfrac{1}{2}(n^o)^3\, \pi_{12}\sigma \\ \delta n_4 &= \delta n_5 = \delta n_6 = 0 \end{aligned} \qquad \text{(I.2-5)}$$

i.e., the crystal becomes birefringent, but the indicatrix has the same principal axes. In the more general case, the principal axes would have been rotated as well.

When the external stress has a sinusoidal dependence (a stress wave) an indicatrix variation wave also passes through the crystal. This periodic change in the index of refraction inside the crystal diffracts light as a grating and is the basis of scattering of light by sound.

The index of refraction tensor is related to the dielectric tensor by

$$\left(\frac{1}{n^2}\right)_{j\ell} = \frac{1}{\varepsilon_{j\ell}} \tag{I.2-6}$$

The displacement vector is given by (in esu units)

$$\underset{\sim}{D} = \underset{\sim}{E} + 4\pi\underset{\sim}{P} \tag{I.2-7}$$

where

$\underset{\sim}{E}$: electric vector

$\underset{\sim}{P}$: polarization vector

In the component form

$$P_j = \frac{1}{4\pi}\left(\varepsilon_{j\ell} - \delta_{j\ell}\right) E_\ell \tag{I.2-7a}$$

The change in polarization due to external stress is

$$\delta P_j = \frac{1}{4\pi}\left(\delta\varepsilon_{j\ell}\right) E_\ell \tag{I.2-8}$$

When $j = \ell$, for example, $j = \ell = 1$

$$\delta\left(\frac{1}{n^2}\right)_{11} = \delta\left(\frac{1}{\varepsilon_{11}}\right) = -\frac{\delta\varepsilon_{11}}{\varepsilon_{11}^2} = -\delta\varepsilon_{11}/\varepsilon_{11}\varepsilon_{11} \tag{I.2-9}$$

When $j \neq \ell$, the relationship between $\delta\varepsilon_{j\ell}$ and $\delta(\frac{1}{n^2})_{j\ell}$ can be derived as follows:

The index of refraction ellipsoid is derived from

$$8\pi w_e = \underset{\sim}{E} \cdot \underset{\sim}{D} = E_i \varepsilon_{ij} E_j = D_i B_{ij} D_j \qquad \text{(I.2-10)}$$

where w_e is the energy density. Therefore

$$(B_{ij}) = (\varepsilon_{ij})^{-1} \qquad \text{(I.2-11)}$$

For $i \neq j$, for example, i= 1, j= 2

$$B_{12} = - \begin{vmatrix} \varepsilon_{12} & \varepsilon_{13} \\ \varepsilon_{32} & \varepsilon_{33} \end{vmatrix} \Big/ \det(\varepsilon_{ij}) \qquad \text{(I.2-12)}$$

Assume $\varepsilon_{j\ell} \underset{j\neq\ell}{} << \varepsilon_{11}, \varepsilon_{22}, \varepsilon_{33}$, i.e., the effect of stress is small on the indicatrix

$$\delta B_{12} = B_{12} = -\varepsilon_{12}/\varepsilon_{11}\varepsilon_{22} = - \delta\varepsilon_{12}/\varepsilon_{11}\varepsilon_{22} \qquad \text{(I.2-12a)}$$

Combining equations (I.2-2), (I.2-9), and (I.2-12a)

$$\delta B_{j\ell} = \delta(\frac{1}{n^2})_{j\ell} = - \frac{\delta\varepsilon_{j\ell}}{\varepsilon_{jj}\varepsilon_{\ell\ell}} = \pi_{j\ell mn}\, \sigma_{mn} \qquad \text{(I.2-13)}$$

Equation (I.2-8) becomes, with superscript i to indicate incident light,

$$\delta P_j = - \frac{1}{4\pi} \varepsilon_{jj'\ell\ell} \pi_{j\ell mn}\, \sigma_{mn}\, E_\ell^{(i)} \qquad \text{(I.2-14)}$$

which is the nonlinear source term in Maxwell's equations that couples

sound wave σ_{mn} and incident light $E_\ell^{(i)}$ to generate the diffracted light.

The diffracted light can be represented in terms of scalar and vector potentials Φ,A respectively as

$$\underset{\sim}{E}^{(d)} = -\nabla\Phi - \frac{1}{c}\frac{\partial \underset{\sim}{A}}{\partial t} \tag{I.2-15}$$

with

$$\Phi = -\int d^3x' \int dt' \, \frac{\nabla'\cdot\delta\underset{\sim}{P}(\underset{\sim}{x}',t')}{|\underset{\sim}{x} - \underset{\sim}{x}'|}\,\delta\left(t' - t + \frac{|\underset{\sim}{x} - \underset{\sim}{x}'|}{c}\right)$$

$$\underset{\sim}{A} = \frac{1}{c}\int d^3x' \int dt' \, \frac{\partial\delta\underset{\sim}{P}(\underset{\sim}{x}',t)}{\partial t'}\,\delta\left(t' - t + \frac{|\underset{\sim}{x} - \underset{\sim}{x}'|}{c}\right)\Big/|\underset{\sim}{x} - \underset{\sim}{x}'| \tag{I.2-16}$$

Let both incident light and acoustic wave be monochromatic plane waves. (Since the diffracted light field is linear in the amplitudes of incident and acoustic fields, more general fields can be represented by superposition)

$$\underset{\sim}{E}^{(i)}(r,t) = \underset{\sim}{E}^{(i)o}\exp[i(\underset{\sim}{k}^{(i)}\cdot\underset{\sim}{r} - \omega^{(i)}t)]$$

$$\sigma_{mn} = \Sigma_{mn}\exp[i(\underset{\sim}{K}\cdot\underset{\sim}{r} - \Omega t)] \tag{I.2-17}$$

$$\underset{\sim}{E}^{(d)}(\underset{\sim}{r},t) = \underset{\sim}{E}^{(d)}\exp[i(\underset{\sim}{k}^{(d)}\cdot\underset{\sim}{r} - \omega^{(d)}t)]$$

On substituting (I.2-17) into (I.2-16), then into (I.2-15), Hope (1968) for example, showed

$$\omega^{(d)} = \omega^{(i)} + \ell\Omega$$

$$\underset{\sim}{k}^{(d)} = \underset{\sim}{k}^{(i)} + \ell\underset{\sim}{K} \quad , \quad \ell\text{: integer or zero} \qquad \text{(I.2-18)}$$

These are conservation laws of energy and pseudomomentum. The same conservation laws can also be derived by quantum mechanical means if one quantizes the acoustic and electromagnetic fields, expresses the interaction between acoustic and electromagnetic fields as a perturbation Hamiltonian, and solves the equation of motion for the boson operators. However, the classical treatment is sufficient for the present purpose.

The conservation laws hold regardless of crystal symmetry.

In isotropic crystals or in anisotropic crystals when the diffracted light has the same index of refraction as the incident light, (this would be true, for instance, when the diffracted light has the same polarization as the incident light) the light-sound scattering takes the relatively simple form of normal Bragg diffraction, and in the long acoustic wavelength limit, Raman-Nath (or Debye-Sears) scattering.

The more complicated case of scattering in an anisotropic crystal when the diffracted light experiences a different index of refraction from the incident light is discussed by Dixon (1967a) and by Hope (1968). The results are omitted here because the experimental technique of the present study is derived from Raman-Nath scattering.

The difference between normal Bragg scattering and Raman-Nath scattering has been discussed by Extermann and Wannier (1936), by

Willard (1949), and by Klein and Cook (1967). The results can be summarized as follows:

The important parameters are

$$v = 2\pi(\delta n)t/\lambda_o \ , \quad Q = \left(\frac{2\pi}{\Lambda}\right)^2 \left(\frac{\lambda_o}{2\pi}\right) t/n_o, \quad \alpha = -\frac{n_o \Lambda}{\lambda_o} \sin\theta$$

where δn: amplitude of index of refraction variation (experienced by the polarization vector)

λ_o: light wavelength in vacuum

t: width of acoustic wave column

Λ: acoustic wavelength

θ: angle between light wave vector and sound wave front

n_o: index of refraction (experienced by the polarization vector) in the absence of sound wave

The Raman-Nath region is defined by

$$Qv \leq \frac{\pi^2}{4} \qquad \text{and} \qquad Q << 2 \tag{I.2-19}$$

The normal Bragg region is defined by

$$Q \geq 4\pi \tag{I.2-20}$$

Refer to Figure 1. From energy and momentum conservations (I.2-18),

$$\sin\phi_\ell = (k \sin\theta + \ell K)/(\omega + \ell\Omega)/c = \sin\theta + \ell \frac{\lambda}{\Lambda} \tag{I.2-21}$$

since $\Omega/\omega = 3 \times 10^7 \Big/ \dfrac{3 \times 10^{10}}{0.63 \times 10^{-4}} = 0.63 \times 10^{-7} << 1$ for 30 MHz acoustic wave scattering light at 0.63 μm wavelength.

Raman-Nath region

(i) Many diffraction orders are observed, with intensities given by

$$I_\ell = J_\ell^2\left[v \frac{\sin(\frac{Q\alpha}{2})}{\frac{Q\alpha}{2}}\right] , \quad J_\ell: \text{Bessel function of order } \ell \qquad (I.2\text{-}22)$$

(ii) The diffraction intensity pattern is symmetric at all angles of incidence, since $I_\ell = I_{-\ell}$.

(iii) Oblique incidence has the effect of reducing the value of v by $\sin(Q\alpha/2)/(Q\alpha/2)$.

Normal Bragg region

Only the negative first order $\ell=-1$ is observed when $\alpha=-\frac{1}{2}$, i.e., $\sin\theta = \lambda/2\Lambda$. From equation (I.2-19)

$$\sin\phi_{-1} = -\frac{\lambda}{\Lambda} + \sin\theta = -\frac{\lambda}{2\Lambda} = -\sin\theta \qquad (I.2\text{-}23)$$

which is the familiar Bragg condition.

Transition region

Between Raman-Nath region and Bragg region, equation (I.2-19) still holds. The intensity pattern is generally asymmetric for positive and negative orders. Also no simple analytic solution can be given to the intensity of different orders of diffracted light.

Physically, the distinction between the regions is that, in the normal Bragg region, the width of the sound wave front is not negligible and no resulting diffracted light can be observed unless light scattered

from different parts of the same wave front are in phase.

Equation (I.2-19), derived from conservation principles, is valid for all ranges of variables Q, α, and v, and is the basis of the present measuring technique.

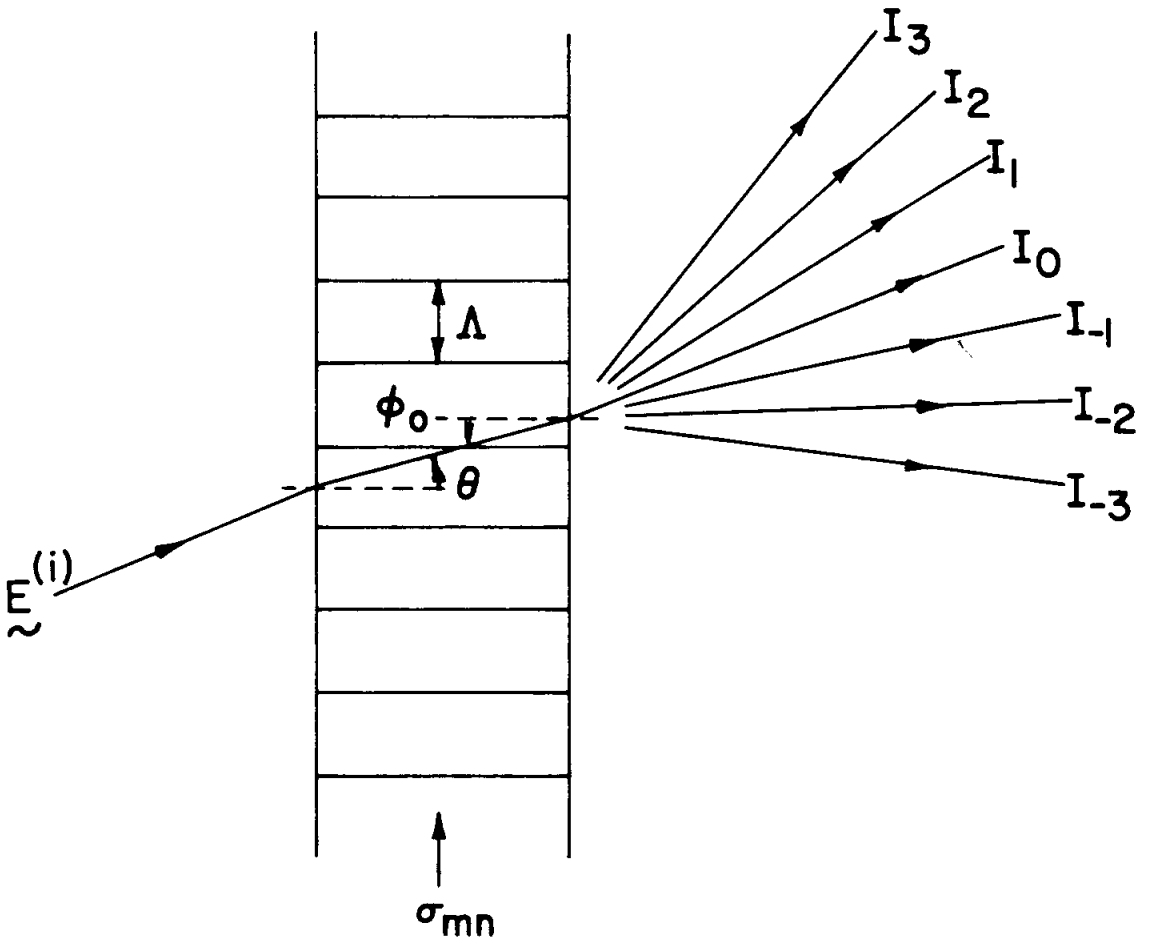

Figure I-2-1. Schematic representation of light-sound scattering in the Raman-Nath region.

3. Experimental Technique

The experimental setup is illustrated schematically in Figure I.3-1. The light source is derived from a Spectra Physics model 135-3 mW helium-neon laser (Spectra Physics, Mountain View, California) which has random polarization and operates in the TEM_{00} mode. The laser beam is spatial filtered by a Wild microscope objective (magnification 20:1, N.A. 0.45) which focuses the beam through a 25 micron pinhole. After spatial filtering, the laser beam is focused on the photographic plate by a second microscope objective (Leitz-Wetzlar, magnification 3.2:1, N.A. 0.12). The microscope objectives are mounted on angular orientation devices with horizontal and vertical rotational axes. These angular orientation devices are in turn mounted on translation stages with three degrees of translation freedom. The pinhole is mounted on two translation stages stacked to provide freedom in two directions perpendicular to the laser beam. The microscope objectives are aligned with their lens axes coinciding with the centroid of the laser beam. The reflecting mirror, flat to $1/10\lambda$, is mounted in an angular orientation device with horizontal and vertical rotation axes which is in turn mounted on a translation stage.

The sample, a spinel parallelepiped with (100) and (110) faces, is spring loaded in a sample holder. The sample holder has two parts, and is shown in detail in Figure I.3-2. The sample holder is spring loaded in a tubular furnace with one spacer block at each end. The spacer block is shown in Figure I.3-3 and components of the tubular

furnace are shown in Figure I.3-4 through Figure I.3-8. The cross-section of the furnace assembly through the two thermocouples is shown in Figure I.3-9. The furnace is latched with springs on two V-blocks (Figure I.3-10) which are bolted to a Lansing model 20.127 translation stage (Lansing Research Corporation, Ithaca, N.Y.) with translation direction perpendicular to the laser beam. Finally, the translation stage is bolted to the base plate of a vacuum tank. The translation stage and leveling screws on the base plate are used to position the crystal such that the laser beam would go through inside the crystal once it is aligned perpendicular to the crystal face. The vacuum tank, a cylinder 8 inches inside diameter and 12 inches high, is made of 304 stainless steel. Two openings 1-1/2 inches in diameter are drilled opposite to each other in the tank to weld the two short 1-1/2 inch outside diameter 304 stainless steel tubings. Flanges for O-ring seal are welded to the tank as well as to the short tubings. Details of the vacuum tank are shown in Figure I.3-11. One hole threaded with 1/8 inch pipe thread is drilled in the center of the top plate for a thermocouple vacuum gauge sensor. Fourteen holes are drilled in the base plate to solder the vacuum electrical feedthroughs. The top and base plates are shown in Figure I.3-12. The electrical feedthroughs are Fusite glass to steel hermetically sealed terminals. Two terminals are used for heater power, two for shutter control, and six are used for thermocouple feedthroughs. The thermocouple feedthroughs have a hollow tube as central electrode, while all the others have solid central electrodes. The thermocouples are fed through these tubes before being

silver soldered to them to provide for the vacuum seal. The ground electrodes of feedthrough terminals are soldered to the base plate using 50/50 lead-tin solder. An aluminum housing for the optical window is bolted and sealed by O-ring to one end of the vacuum tank extension. Details of this window housing are shown in Figure I.3-13. The window is an optical flat of fused silica two inches in diameter, half an inch thick, flat to $1/10\lambda$ and having faces parallel to better than 10 seconds of arc. A section of Cajon 321 stainless steel bellows, 3 inches long and 1-1/2 inches outside diameter (Cajon 321 x 24-3, Cajon Company, Cleveland, Ohio) welded with flanges at both ends, is bolted and sealed with O-ring to the other vacuum tank extension. A Uniblitz model 225-0 shutter (Vincent Associates, Rochester, N.Y.) is fixed by screws to the inside of one of the flanges. Details of this shutter housing are shown in Figure I.3-14. A long 304 stainless steel tubing, 1-1/2 inches outside diameter and approximately 84 inches long, is connected and sealed to the shutter end of the bellows section with O-ring and flange. The flange for a vacuum butterfly valve (Cajon CFR rotatable 1-1/2 inch flange, part no. 304L-24 CFR-275) is welded to the farther end of this long tubing. Another rotatable flange is welded to a bellows section with a photographic plate holder welded to the other end. The long tubing and the end bellows section are connected by a Nupro 1-1/2 inch O-ring sealed butterfly vacuum valve (part no. 304-24 VFO) sealed with copper gaskets (Cajon CU-CF-275-2). One hole, 1/4 inch diameter, is drilled in the long tubing and also in the end bellows section for vacuum pumping and bleed valve connections.

All optical components and vacuum system are rigidly glued to a granite table (8" x 36" x 108") by epoxy for stability.

The vacuum system is sealed at one end by the optically flat window, and at the other end by a photographic plate in the photographic plate holder. The photographic plate holder is coupled to an anchoring block by screws, and nuts are used,when pushing against the vacuum pull, to orient the photographic plate plane parallel to the sample. Details of the photographic plate holder are shown in Figure I.3-15, and the relationship between the photographic plate holder and the anchoring block in Figure I.3-16.

The purpose of the evacuated tank is to have the light path between sample and recording photographic plate under partial vacuum so as to reduce index of refraction fluctuation which would otherwise introduce random error in the data. A Duo-seal mechanical vacuum pump (Sargent-Welch Scientific Company, Skokie, Illinois) with a liquid nitrogen cold trap is used to evacuate the system. The working vacuum during the experiment is between 85 and 180 microns as measured by a type GTC-100 thermocouple vacuum gauge (Consolidated Electrodynamics, Rochester, N.Y.). The butterfly valve is employed to avoid letting air into the whole system during photographic plate change. While changing the photographic plate both butterfly valve and bleed valve no. 2 (refer to Figure I.3-1) are shut off to keep the tank and the long tubing under vacuum. Bleed valve no. 1 is then opened to let air into the end bellows section. After photographic plate change, bleed valve no. 1 is closed and only the end bellows section needs to

be pumped down. The butterfly valve is then opened to let laser beam through during the experiment.

An ultrasonic standing wave inside the sample is generated by a lithium niobate transducer (30 MHz center frequency) coupled to the sample with Nonaq stopcock grease (S-530, Fisher Scientific Company, Fair Lawn, N.J.) and spring loaded through a Webber gauge block by a leaf spring made of Vasco Max 350 high temperature steel (Teledyne Vasco Company, Latrobe, Pa.). Details of transducer loading are shown in Figure I.3-17. The sample is gold coated in a configuration shown in Figure I.3-18 to provide ground connection of the transducer through one-half of the sample holder. The RF signal is generated by a Heathkit model DX-60B variable frequency oscillator (Heath Company, Benton Harbor, Mich.), whose output frequency is synchronized to a Schomandl model ND30M frequency synthesizer (Rohde and Schwarz Sales Company, Passaic, N.J.) by coupling the synthesizer output through a 100 pf capacitor into the oscillator tube grid of the VFO. The output of the VFO is used to drive a Heathkit model DX-60B transmitter, which also quadruples the VFO frequency. The output of the transmitter is fed into the vacuum system to the transducer leads through a section of Uniform Tubes UT-250SS vacuum tight coaxial cable (Uniform Tubes, Collegeville, Pa.) which is sealed on the outside to the vacuum tank by a Swagelok SS-400-1-2 vacuum fitting (Crawford Fitting Company, Cleveland, Ohio). The frequency of the RF signal is measured by a Systron-Donner model 7018 frequency counter (Systron-Donner Corporation, Concord, Cal.).

The Uniblitz shutter is controlled by two relays and a Uniblitz model 100 power supply and drive unit. The relays control the time interval during which a 5-volt signal is applied to the switching circuit which keeps the shutter open. A DPDT switch is used to switch both the transmitter and the shutter relays. The first relay is delayed 50 msec relative to the closing of the switch. Since the transmitter has a rise time of 3/10 of a millisecond, a standing wave is well setup inside the crystal at the opening of shutter by the first relay. The shutter time can be adjusted from 10 msec to 4 sec for photographic plate exposure.

The furnace power is controlled by a Variac whose primary voltage is regulated to stay stable at 115 volts.

Temperatures inside the furnace are measured by two Alumel-Chromel thermocouples (see Figure I.3-9). These two thermocouples are located about 1 mm from the sample. During a separate calibration run, a third thermocouple is pasted with Sauereisen cement directly on the sample surface where the laser beam would leave the crystal, to measure the temperature difference at the sample and at the thermocouple sites. The calibration results are presented in Section 5. A Pace Wiancko model LRT47-8TT-1508 thermocouple reference junction is used to provide a stable 150^{o}F reference temperature. The thermocouple voltage output is read with a Hewlett-Packard 3450A multifunction meter.

During the experiment, the laser beam is aligned perpendicular to the crystal face by the angular orientation device holding the mirror. The photographic plate plane is then aligned parallel to the

crystal face by sealing the end bellows section with an optical flat (1/10λ flat, parallel to better than 10 seconds of arc) and using an auxiliary mirror behind the optical flat. The beam reflected from the auxiliary mirror is made to coincide with the incident beam. Part of the reflected beam is reflected again at the optical flat sealing the end bellows section. This reflected beam is used to guide the adjustment of the plate holder orientation screws. With relative ease, the parallelism between photographic plate and crystal surface and the perpendicularity between laser beam and crystal surface can be adjusted to within 1 milliradian.

The synthesizer frequency is adjusted approximately for standing wave condition of the sample at different temperatures. This can be judged by the intensity of the diffracted light. After the evacuation of the optical path between crystal and photographic plate, the DPDT switch is thrown and the photographic plate is exposed to the diffracted beams. The undiffracted central laser beam is blocked off before it reaches the photographic plate. The photographic plates used in the experiment are Agfa-Gavaert 8E-75 high resolution (3000 lines/mm) and 10E-75 (2800 lines/mm) photographic plate with antihalation back coating. The size of the plates is 4 inches by 5 inches. Immediately after exposure, the plate is processed in Kodak D-19 developer for 6 minutes, in glacial acetic acid stop bath for 30 seconds, in Kodak Rapid Fix for 5 minutes, and followed by washing for 30 minutes.

The distance between photographic plate and sample is measured with Starrett tubular inside micrometers model 121B, model 823B, a Starrett depth micrometer model 513, and a Brown and Sharpe 1" micrometer.

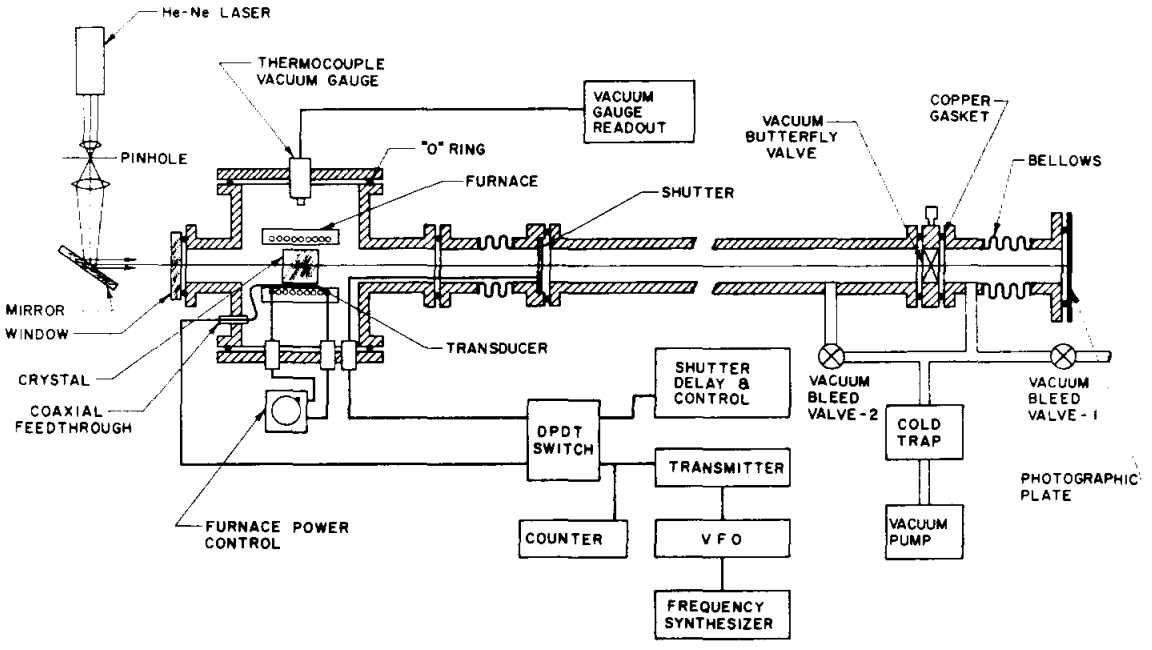

Figure I-3-1. Schematic diagram showing experimental setup for light-sound scattering measurement of temperature dependence of single crystal elastic constants.

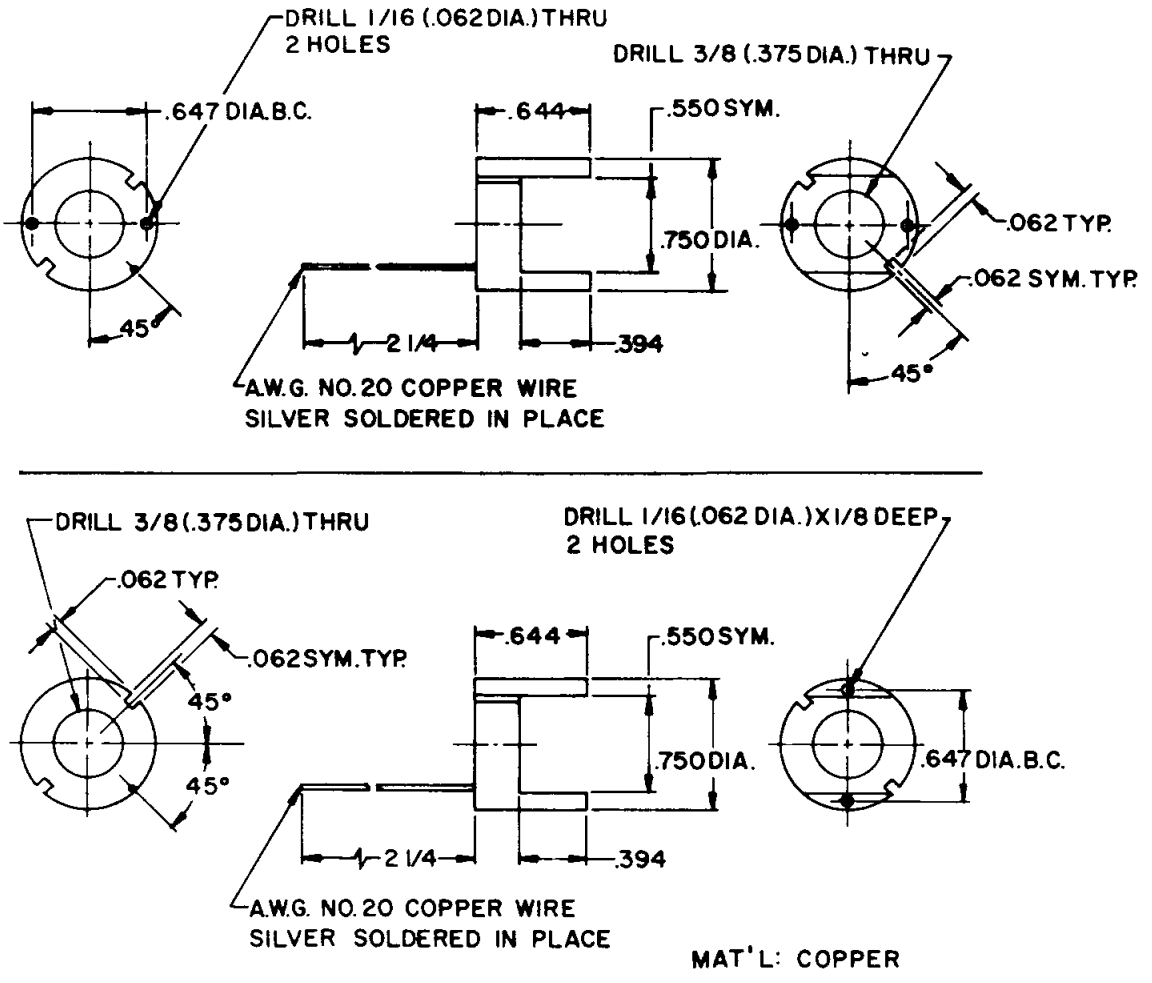

Figure I-3-2. Drawing showing two halves that comprise the sample holder. The 1/16" holes are for alumina locating pins. When assembled, the sample is surrounded by copper on all sides, except for a hole for laser beam and two slots for thermocouples. This is to reduce temperature gradient across the sample. Dimensions are in inches.

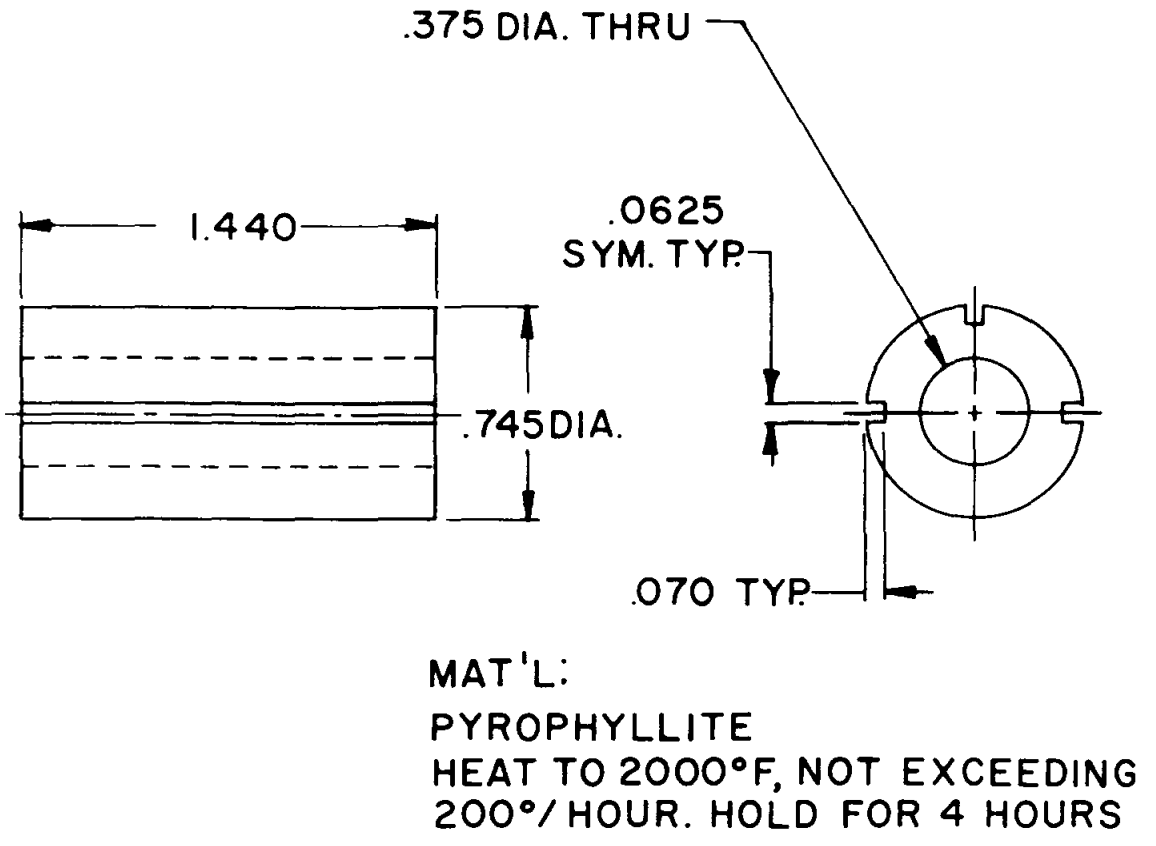

Figure I-3-3. Drawing showing pyrophyllite spacer block for sample holder. Dimensions are in inches.

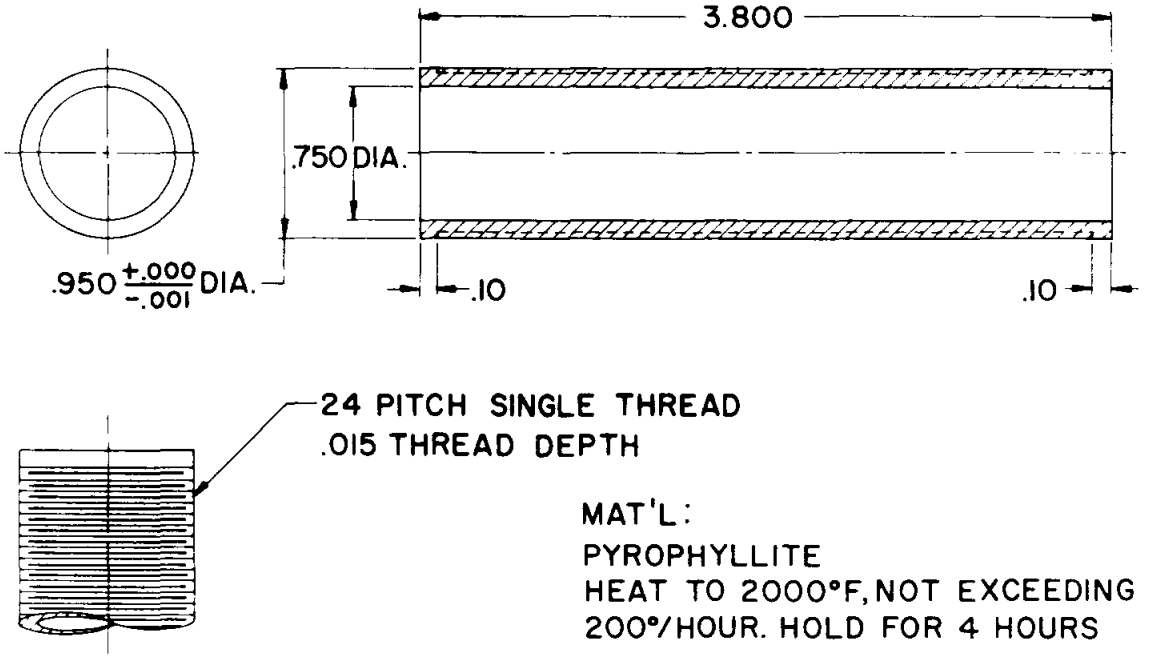

Figure I-3-4. Drawing showing furnace heater core. Dimensions are in inches.

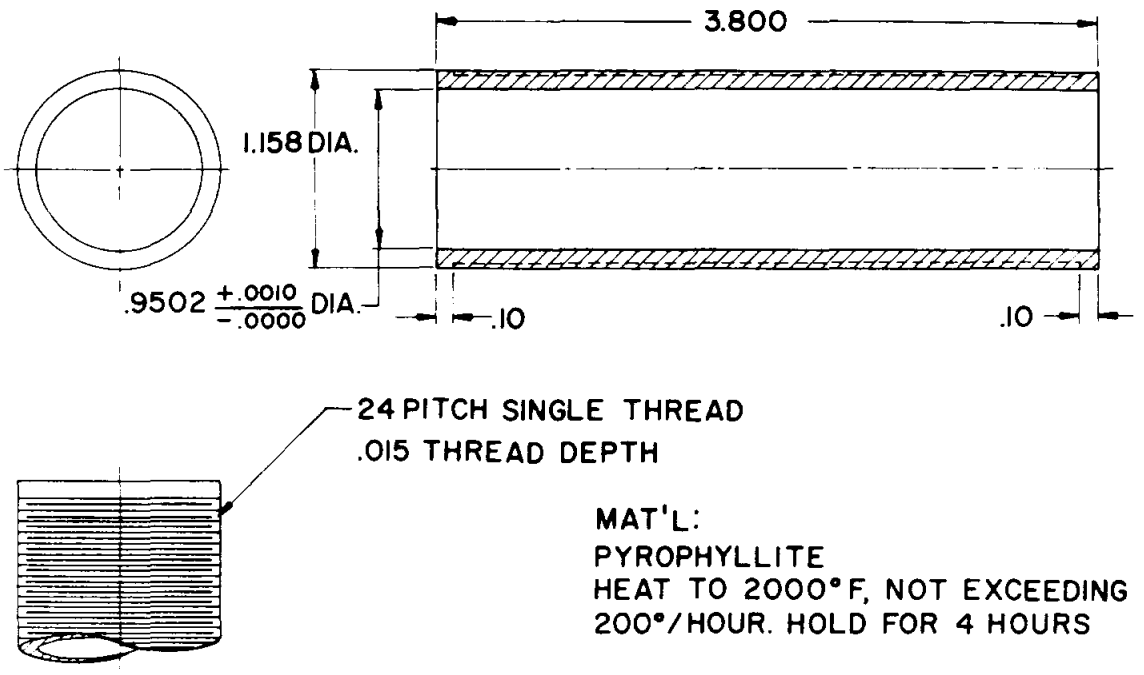

Figure I-3-5. Drawing showing furnace heater sleeve. Dimensions are in inches.

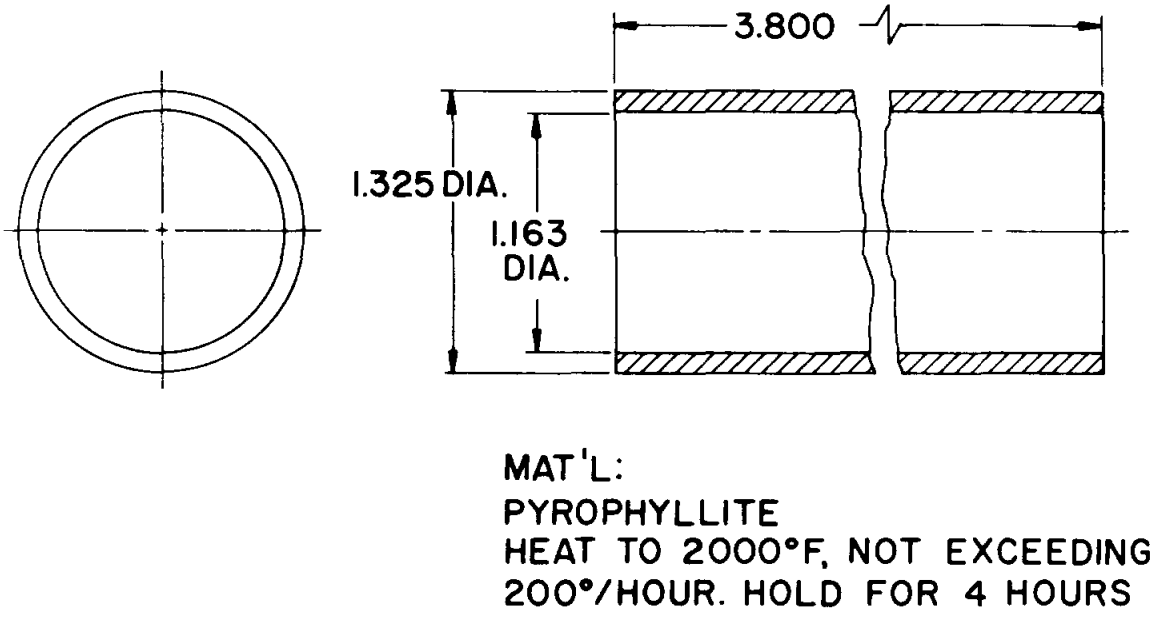

Figure I-3-6. Drawing showing heater cover. Dimensions are in inches.

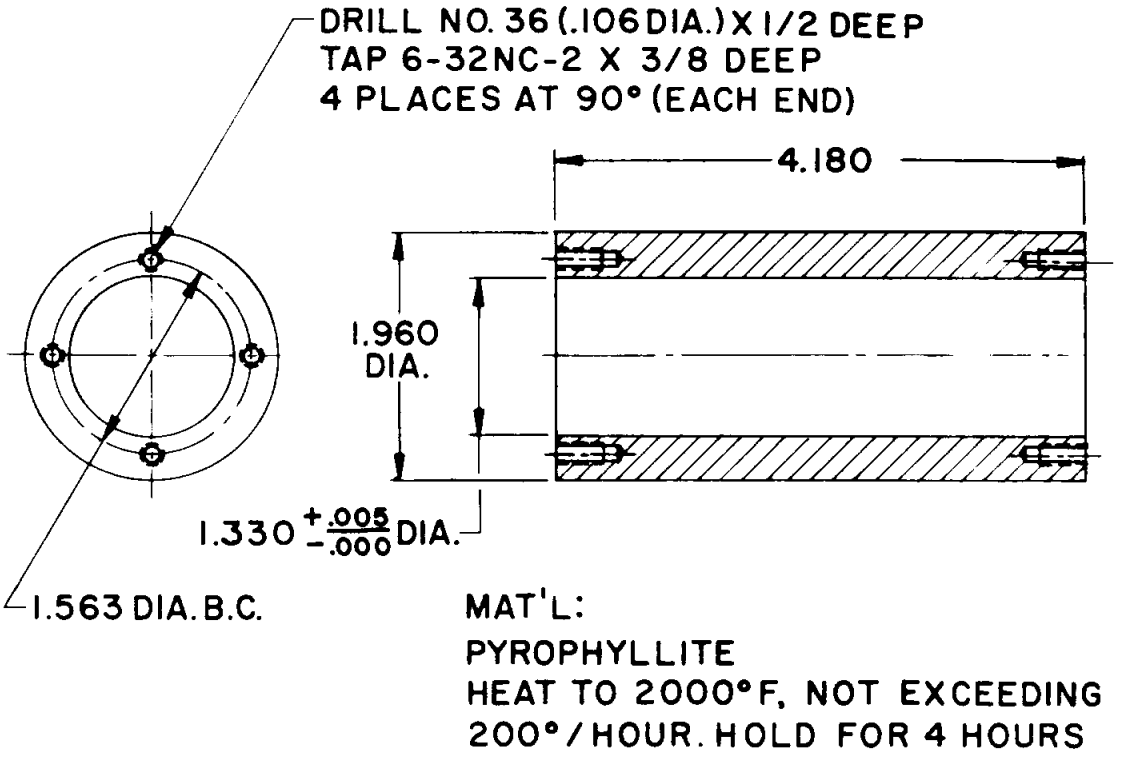

Figure I-3-7. Drawing showing furnace main body. Dimensions are in inches.

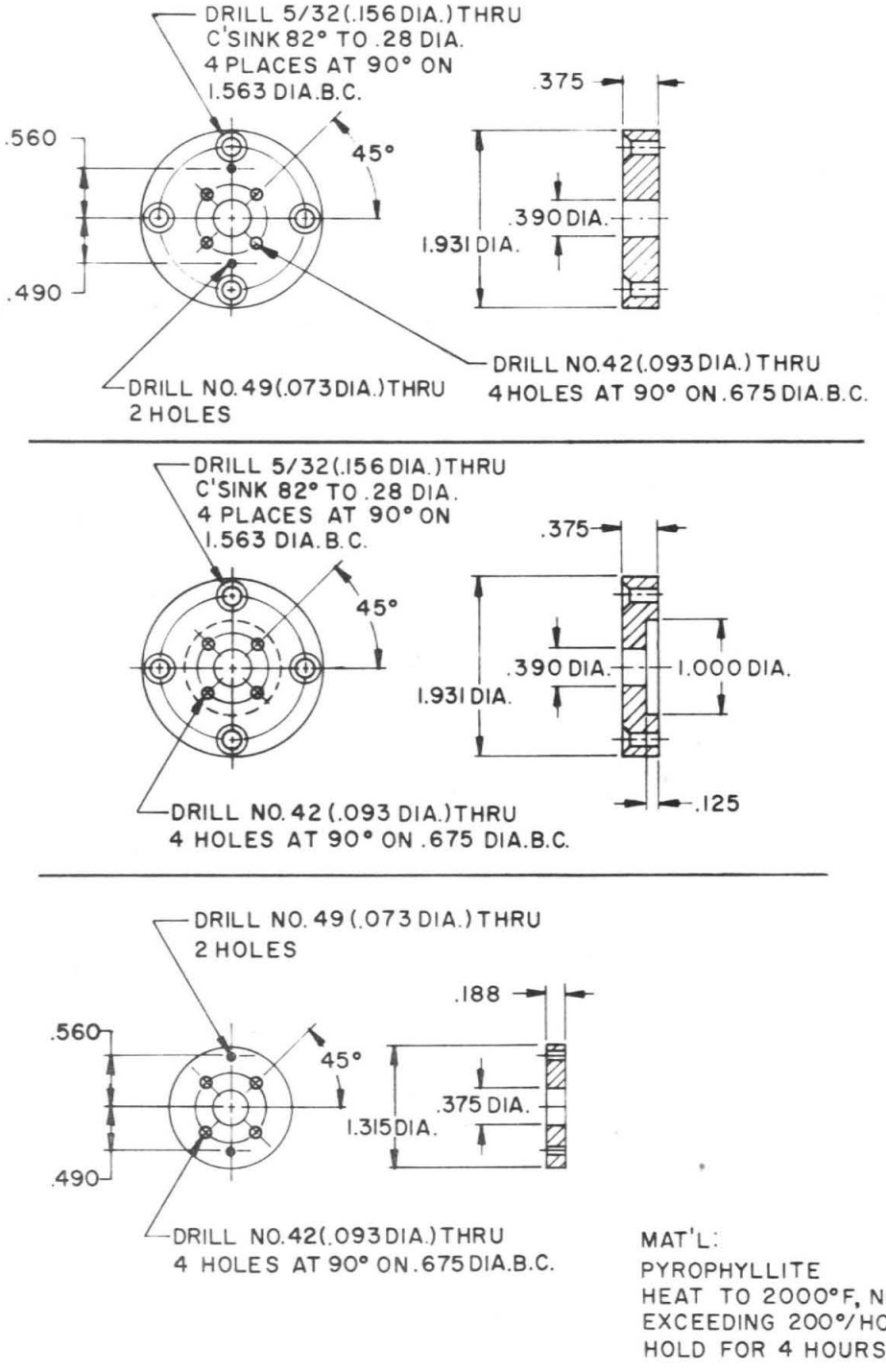

Figure I-3-8. Drawing showing furnace end caps. The step in the central cap of the figure is for spring loading. Dimensions are in inches.

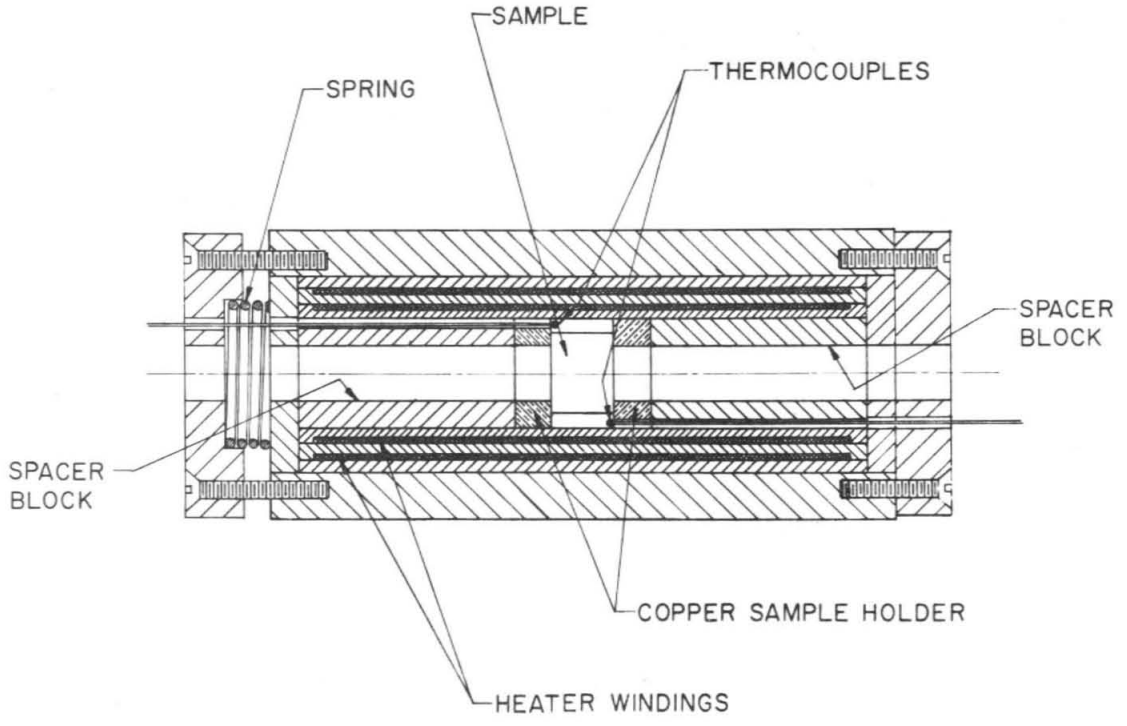

Figure I-3-9. Furnace cross-section through thermocouples with sample in place.

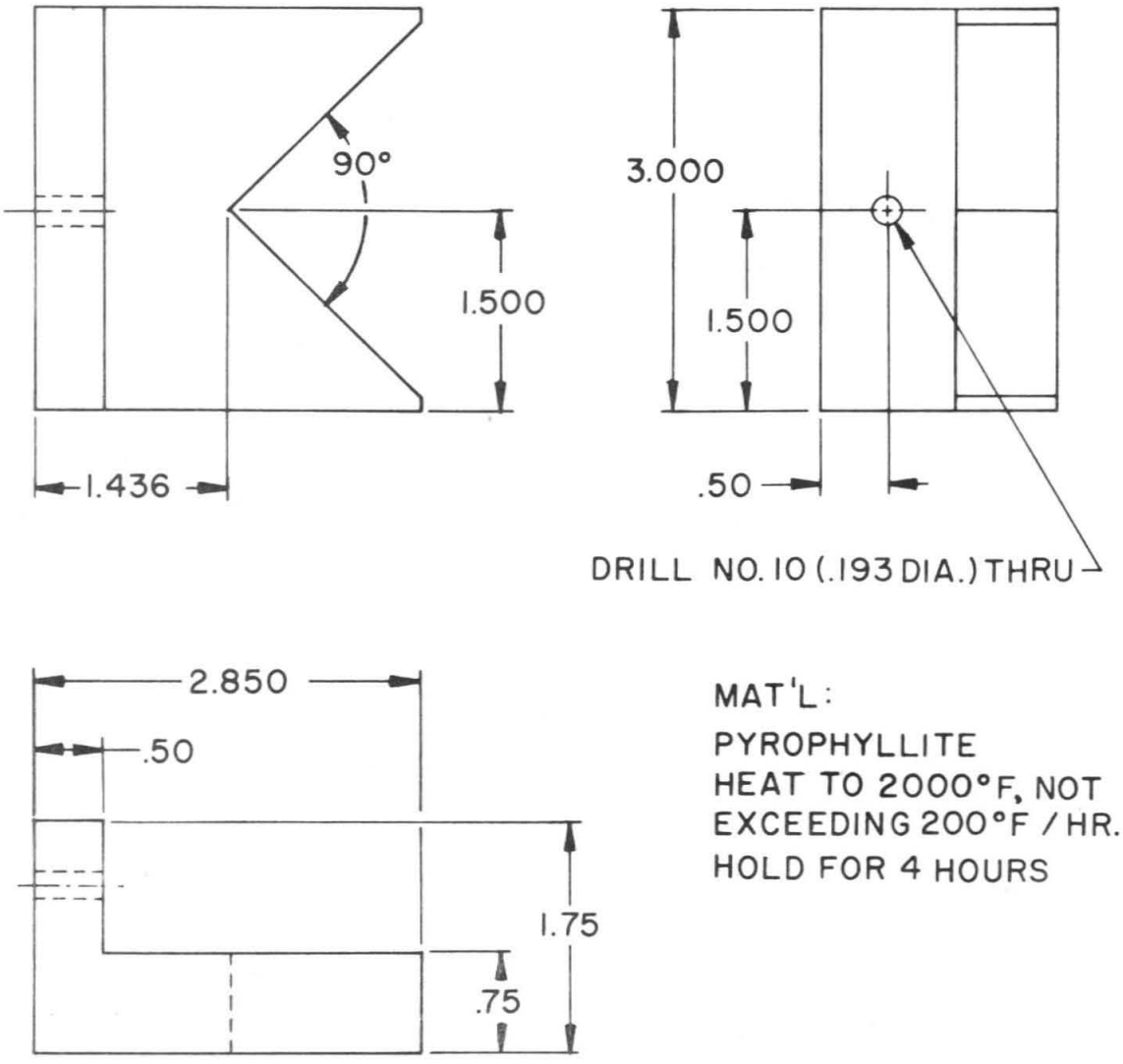

Figure I-3-10. Drawing showing furnace mounting block. Dimensions are in inches.

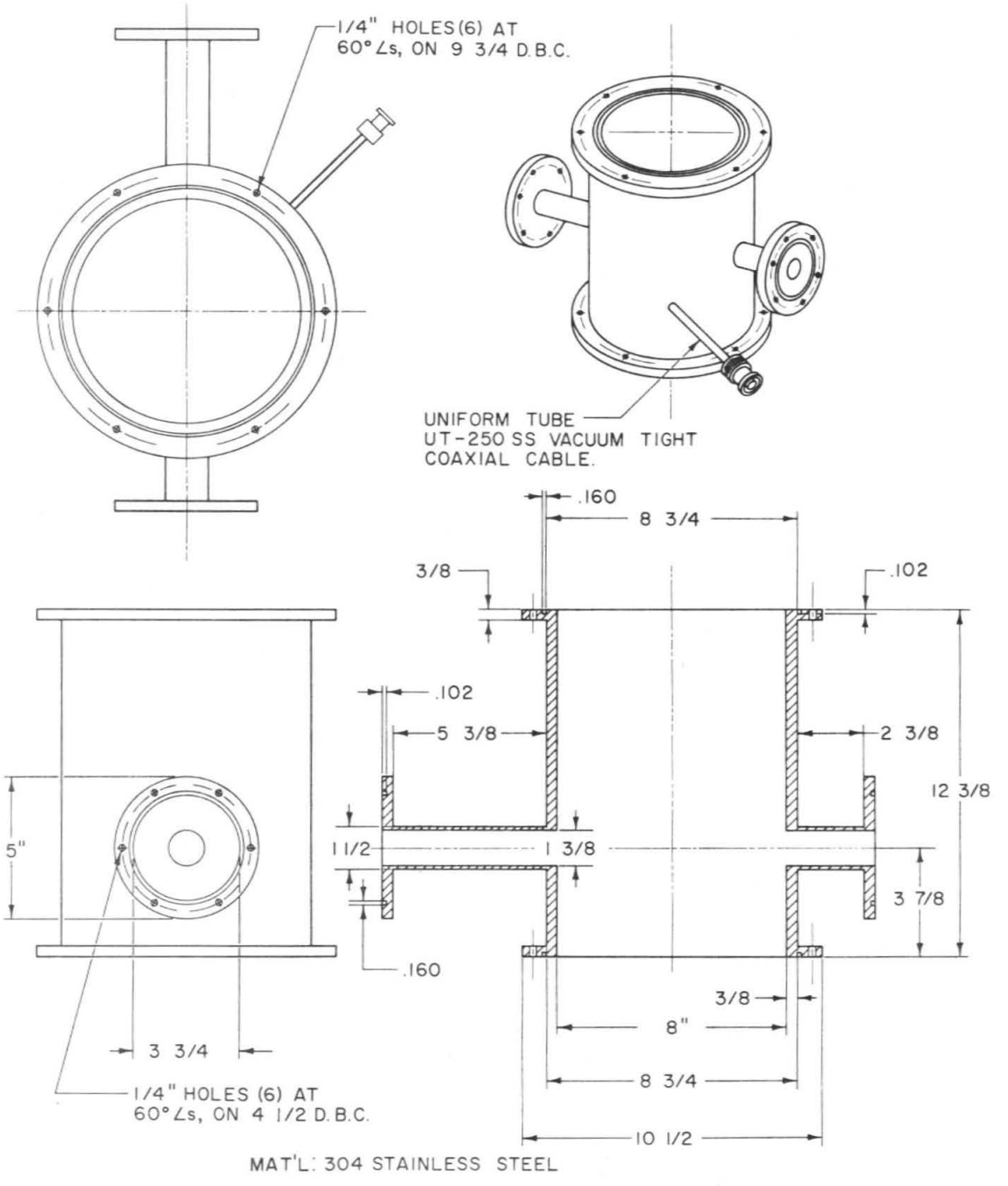

Figure I-3-11. Drawing showing main vacuum tank. Dimensions are in inches.

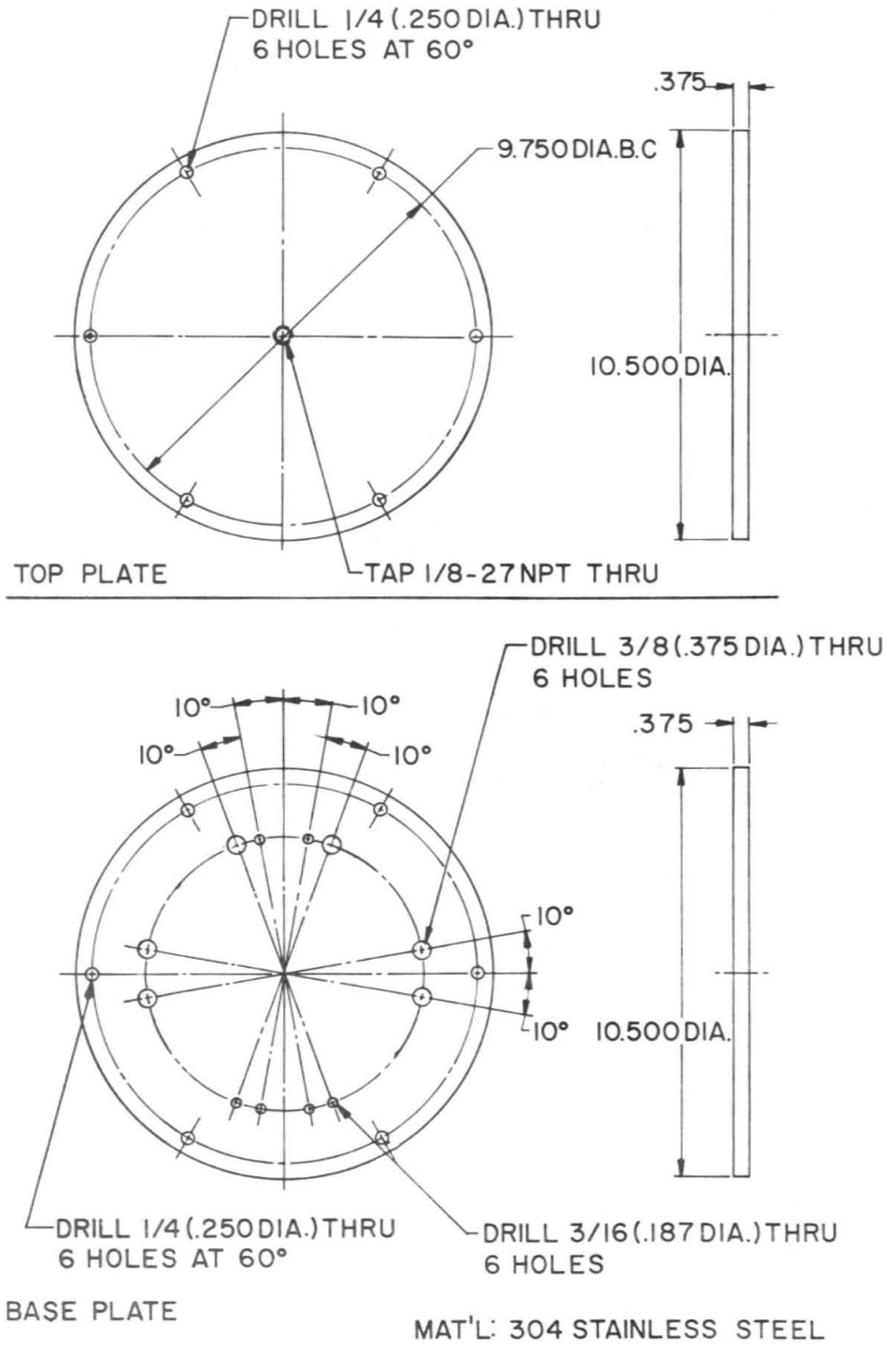

Figure I-3-12. Drawing showing vacuum tank top and base plates. Dimensions are in inches.

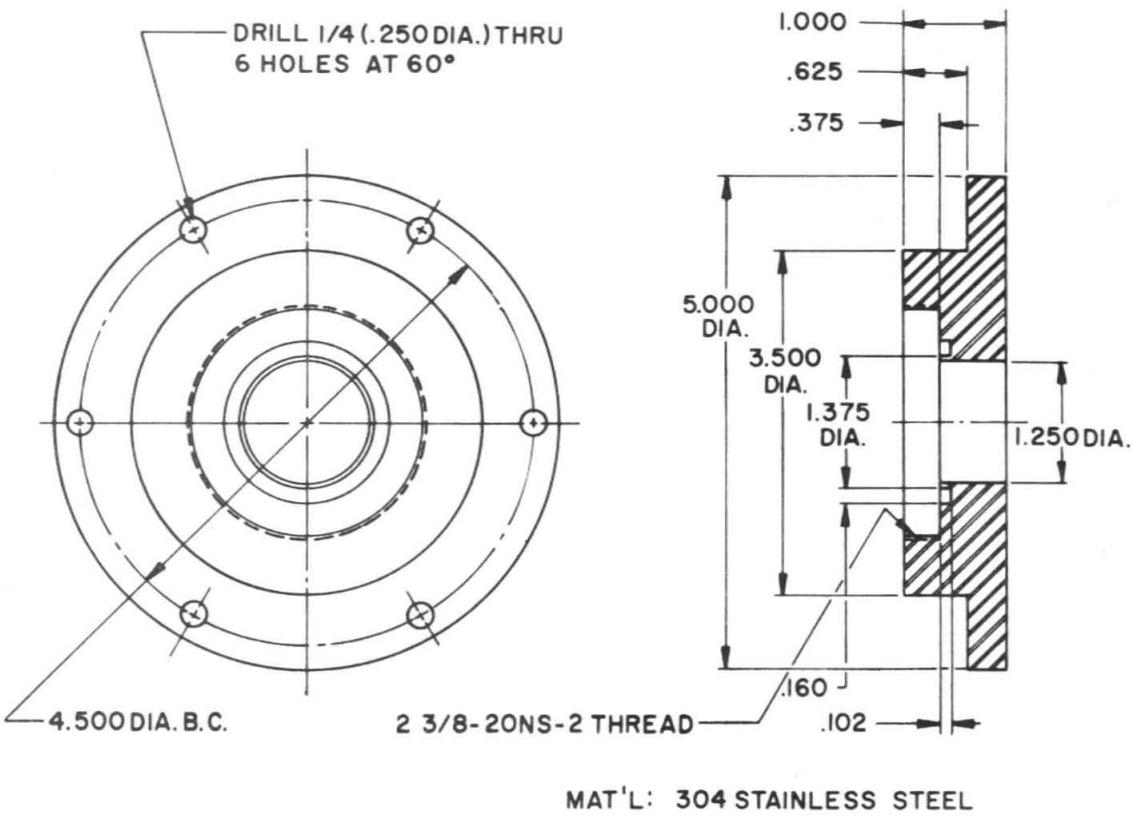

Figure I-3-13. Drawing showing vacuum tank optical window housing. Dimensions are in inches.

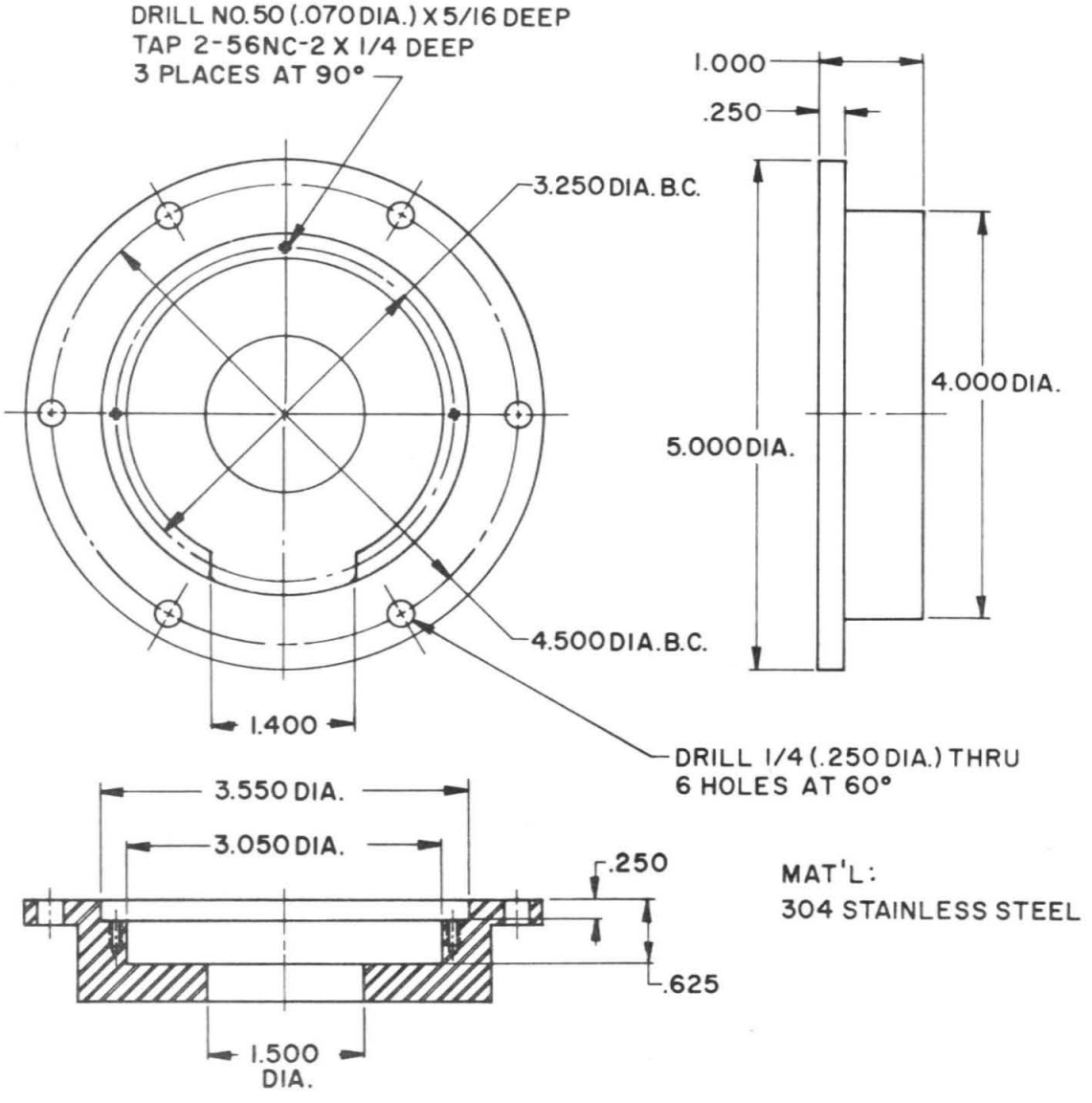

Figure I-3-14. Drawing showing shutter housing. Dimensions are in inches.

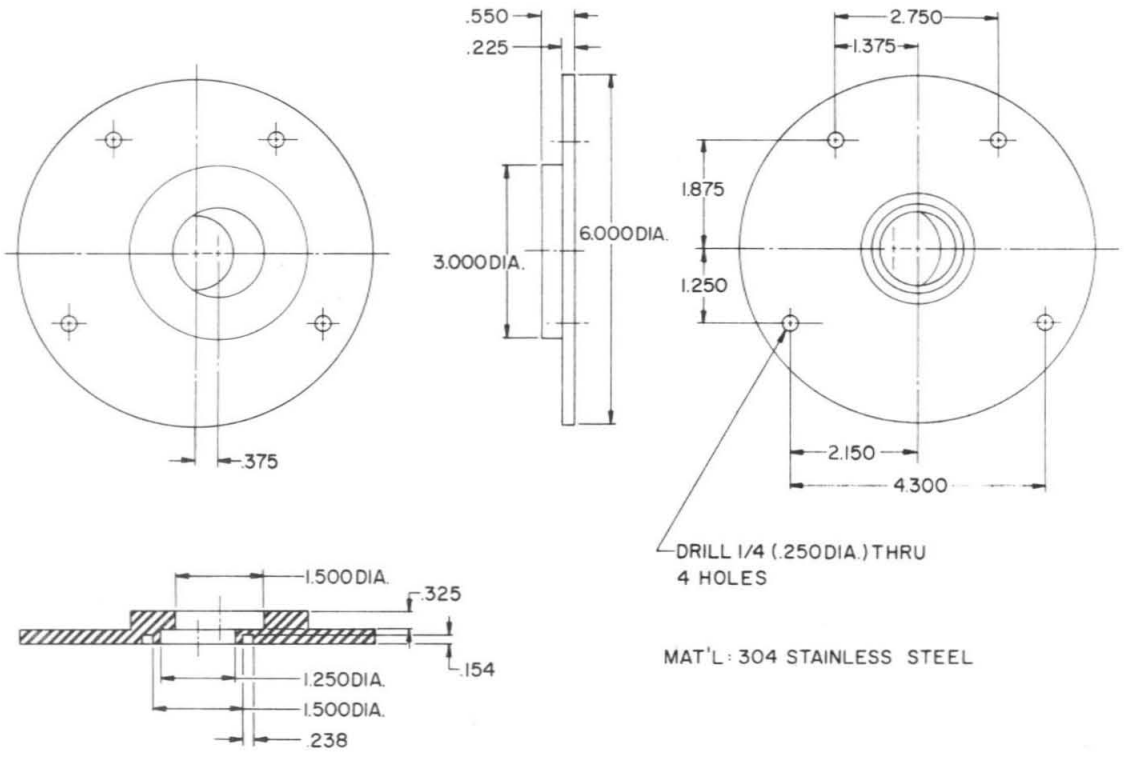

Figure I-3-15. Drawing showing photographic plate holder. Dimensions are in inches.

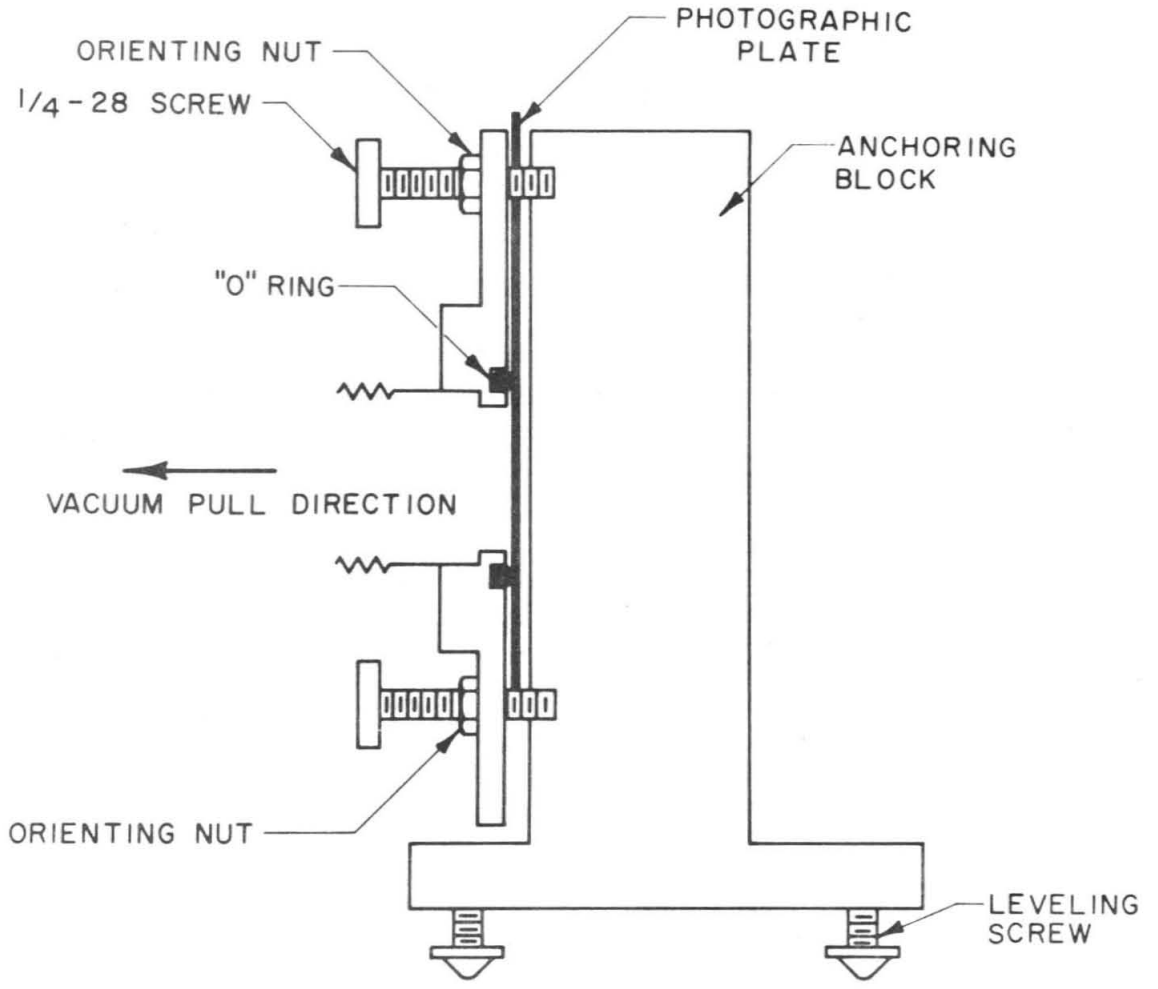

Figure I-3-16. Diagram showing relationship between photographic plate holder and its anchoring block.

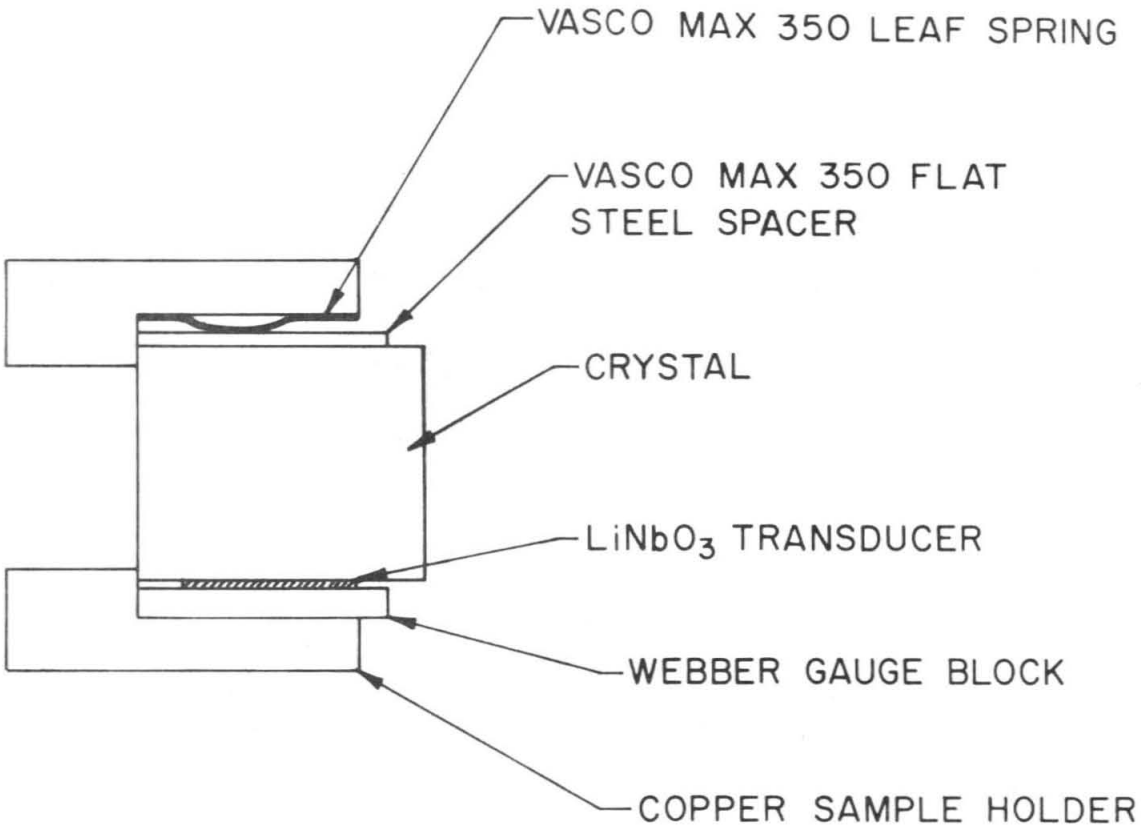

Figure I-3-17. Schematic drawing showing spring loading of $LiNbO_3$ transducer to spinel sample.

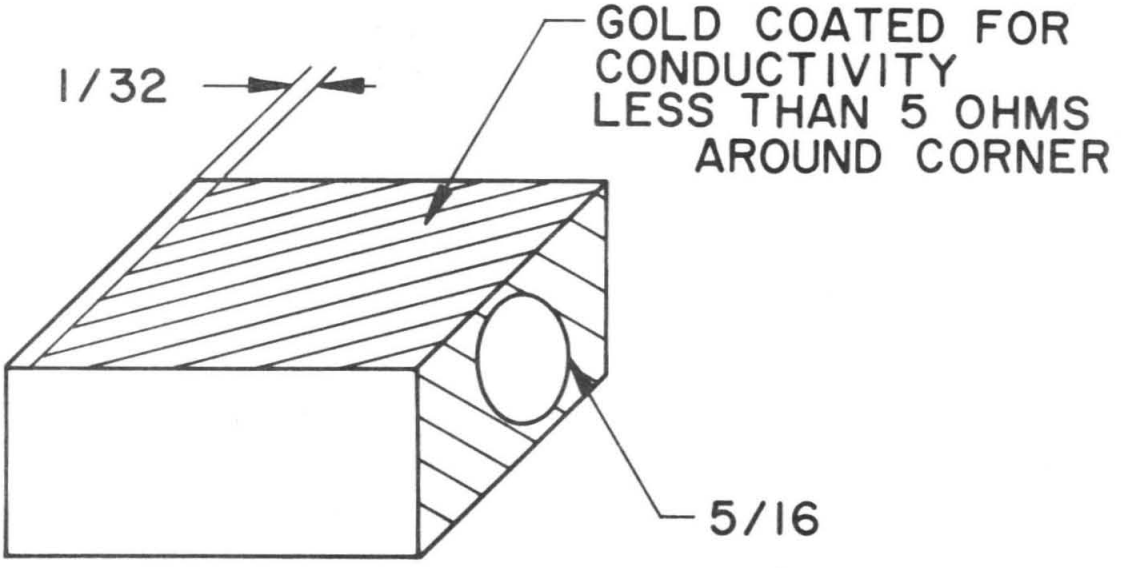

Figure I-3-18. Configuration of sample electrode coating. Dimensions are in inches.

4. Sample Description

The sample is a single crystal stoichiometric $MgAl_2O_4$ spinel grown by Czochralski method and furnished by Crystal Products Division of Union Carbide Corporation. After rough cut, the boule is lapped into a prism with two sets of faces parallel to (001) and (110) respectively. The crystal orientation is determined to be $5 \pm 5'$ parallel to (001) and $9 \pm 5'$ parallel to (110) by Laue back reflection method. (The X-ray work is done by Dr. E. K. Graham, now at Pennsylvania State University). The final polish of the two sets of faces to 1/10 wavelength (sodium light) flat and laser finish is done by Crystal Optics (Ann Arbor, Mich.). The parallelism between the polished faces is less than 10 seconds of arc. The dimension of the sample is 0.8923 ± 0.0002 cm (between (001) faces) x 1.1793 ± 0.0002 cm (between (110) faces) x 1.2578 ± 0.0002 cm (between the unpolished (110) faces). The density of the sample is measured by immersion method using distilled water as immersion liquid. At 18^oC the density is measured to be 3.5790 gm/cm^3. The density is computed to be 3.5784 gm/cm^3 at 25^oC using $\alpha = 6.93 \times 10^{-6}/K$ for linear thermal expansion coefficient (Rigby et al 1946). The sample is also placed between two crossed polarizers and illuminated by a diffused light source to examine for residual stress. No residual stress is found within the sample between the two sets of faces both before and after the experiment.

5. Data and Data Reduction

The data as recorded (raw data) are two dark spots exposed by the diffracted laser beam on a photographic plate. A contact print made from such a photographic plate is shown in Figure I.5-1. The distance between the two spots is measured on the optical density readout recorder chart from a Joyce-Loebl double beam microdensitometer (model MkIIICS, serial no. 497, Joyce, Loebl and Company, Burlington, Mass.). The details of the distance measurement are described below. The photographic plate is placed on the microdensitometer stage with its bottom edge pushed against the bottom edge of the recessed stage. The direction defined by the two spots on the photographic plate is aligned parallel to the scanning direction of the microdensitometer by rotating the stage and observing the images of the two spots with respect to a cross hair on the microdensitometer viewing screen. Alignment error is $\pm 0.1^{o}$. The angle between the direction defined by the spots and bottom edge of the photographic plate γ is read off the stage rotation table. A Starrett no. 360 precision protractor (L. S. Starrett Company, Athol, Mass.) is then placed on top of the photographic plate with its square frame set against the edge of the microdensitometer stage. The protractor angle is set at the angle γ but in an opposite sense. The vernier on the Starrett no. 362 protractor reads to 1/12 of a degree. An American Optical Corporation A01400 stage micrometer (Scientific Instrument Division, American Optical Corporation, Buffalo, N.Y.) is laid on top of the two spots and against the blade of the precision protractor.

The positioning of the protractor angle puts the scale divisions on stage micrometer perpendicular to the microdensitometer travel direction. The purpose of the stage micrometer is to put fiducial marks on the microdensitometer readout chart for distance measurement. The photographic plate, Starret protractor, and the stage micrometer are fixed in position on the microdensitometer stage by spring clips. An example of the microdensitometer readout with this arrangement is shown in Figure I.5-2a and Figure I.5-2b. Since it is the change of distance that is important in the temperature dependence measurement, the two spikes marked "4 mm" and "14 mm" are used as fixed fiducial marks in an entire suite of measurements. (For example, V_p[100] from 293 to 423K). The two density profiles are then matched on a light table and a pencil mark is put on both charts at the same (but arbitrary) location. The distance between the spots is therefore equal to a fixed distance (distance between the fiducial marks "4 mm" and "14 mm") plus the distance from the pencil mark on Figure I.5-2a to "4 mm" and the distance from the pencil mark on Figure I.5-2b to "14 mm". The scale on the charts is provided by the distance between the fiducial marks "3 mm" and "4 mm", and "14 mm" and "15 mm", respectively. These distances are calibrated by American Optical Corporation to be 0.1 ± 0.0005 cm. The use of fiducial marks is necessitated by the limited travel of the microdensitometer stage at such a large magnification (approximately 200 to 1). The distance between the two spots in Figures I.5-2a and I.5-2b is then read as

$$\ell = 10 \text{ mm} + \left(\frac{9.23 \pm 0.01}{19.75 \pm 0.01} + \frac{\binom{6.98}{6.71} \pm 0.01}{19.81 \pm 0.01}\right) \text{ mm}$$

where 10 mm is the distance between the fixed fiducial marks "4 mm" and "14 mm". 9.23 is the distance in centimeters on the chart from the pencil mark on Figure I.5-2b to the "14 mm" marker. 19.75 is the distance in centimeters on the chart between the fiducial marks "14 mm" and "15 mm" on the same figure. The corresponding readings on Figure I.5-2a are $\binom{6.98}{6.71}$, and 19.81. There are two readings, 6.98 and 6.71 because there are two pencil marks on Figure I.5-2a. There are two pencil marks on Figure I.5-2a because the two density profiles are not identical, and there is a latitude in which "matching" of the two density profiles can be considered as equally good. In the present case 6.98 is the distance in centimeters on the chart from the pencil mark to the "4 mm" marker when matching is by the top part of the density profiles. 6.71 is the corresponding distance when matching is by the bottom part of the density profiles. These are illustrated in Figures I.5-3 and I.5-4. This latitude in matching is indeed the major source of experimental uncertainty, and will be discussed in detail later. A measure of the reproducibility of the microdensitometer readout is provided by the repeated optical density readouts of divisions on the stage micrometer used as fiducial markers. Histograms of the distribution of repeated readout of distance between pairs of markers are shown in Figure I.5-5. It is estimated from these histograms that the repeatability of intensity profiles is within 0.05 cm on the microdensitometer recorder chart.

Note that in Figure I.5-5 the distance between the two markers "5 mm" and "6 mm" in the data readout for $V_s[001]$ differs from that in the data readout for $V_p[110]$. This is because the ratio arm connecting the microdensitometer specimen table and recorder chart table is removed between the two readouts, and slight variation in the setting of the ratio arm in its socket causes the difference in the two readouts. Since the error in aligning the two spots with the microdensitometer stage travel direction is $\pm 0.1^{o}$, and the error in aligning the stage micrometer with the two spots is also $\pm 0.1^{o}$, the error in distance measurement between the two spots due to angular misalignment is $\ell(1 - \cos 0.14^{o}) \cong 5 \times 10^{-6}\ell \cong 0.05$ μm , equivalent to 0.001 cm on the readout chart, and is negligible compared to the latitude in density profile matching as discussed above.

Consider now the problem of the difference in the two density profiles on the same photographic plate. Note first that the degree of disparity varies from one photographic plate to another. Indeed, the two density profiles in Figures I.5-2a and I.5-2b are one of the worst cases. An example of two density profiles which match better is illustrated by Figures I.5-6a, I.5-6b, and I.5-7. Note secondly, that whenever "bad" matching exists, the matching of one profile with the mirror image of the other profile is generally better. This is illustrated in Figure I.5-8 with the profile in Figure I.5-2a matching the mirror image of the profile in Figure I.5-2b. There are density profile distortions introduced during photographic processing, such as unevenness in plate emulsion and water stain marks during drying, and electronic noises introduced during the microdensitometer readout.

These distortions and noises are, however, insufficient to account for the disparity, when it exists, between the two density profiles. The reason for this disparity is that the stress-induced birefringence inside the crystal does not assume a plane wave front parallel to the sample faces. Temperature gradient inside the sample, edge and corner effects, lack of perfect parallelism between sample faces, positioning of the transducer (not exactly at the center of sample face) and transducer radiation pattern all cause the steady state birefringence pattern to deviate from a plane standing wave. However, the steady state birefringence pattern induced by forced vibration of the crystal can be decomposed into plane waves in different directions. These plane waves will be divided into those whose wave vectors are perpendicular to the light wave vector and those which do not belong to the class just described for separate discussions. For plane waves whose wave vector are perpendicular to the light wave vector, the diffracted light intensity is given by equation (I.2-22) with $\alpha = 0$, i.e., $I_1 = J_1^2(v)$. By adjusting the transducer driving frequency, however, only plane waves whose wave vector lies nearly perpendicular to the polished faces (on one of which the transducer is mounted) can enjoy the condition of constructive interference. The result is demonstrated in Fig. I.5-1. Since all photographic plates are pushed with bottom edge against the film holder bottom orienting screws during exposure, the direction defined by the two spots relative to the photographic bottom edge serves to check the maximum deviation in direction from pure mode of the sound wave velocity

which each photographic plate measures. The microdensitometer table angle readings in Tables I.5-1 to I.5-4 are exactly these data.

Since to compute, from pure mode velocity, sound velocities of modes whose directions deviate slightly from a pure mode involves correction factors proportional to the square of the cosine of the deviation angle (for example, Neighbours and Schacher 1967) and $1 - \cos^2 0.6^\circ = 1.08 \times 10^{-4}$, where 0.6° is the maximum deviation angle in Tables 1 through 4, the error involved in this respect is at most one-fifth of that arising from disparity of density profiles. In the more typical case, the deviation angle is 0.2° and $1 - \cos^2 0.2^\circ = 1.2 \times 10^{-5}$. Now consider those waves in whose wave front the light wave vector does not lie. The diffracted light intensity from these waves is given by equation (I.2-22) with $\alpha \neq 0$, $I_1 = J_1^2[v \frac{\sin(Q\alpha/2)}{(Q\alpha/2)}]$. The intensity distribution $J_1^2[v \frac{\sin(Q\alpha/2)}{(Q\alpha/2)}]$ as a function of α is plotted in Klein and Cook (1967) and has zeros at $Q\alpha = 2m\pi$ where m is any non-zero integer. The intensity is significant only for values of α less than the first zero. The first zero occurs at $\alpha = 2\pi/Q$. Recall $Q = \frac{2\pi}{\Lambda^2} \frac{\lambda_o}{n_o} t$, $\alpha = n_o \frac{\Lambda}{\lambda_o} \sin\theta$, where θ is the angle between sound wave front and light wave vector. $Q\alpha = 2\pi$ implies $|\sin\theta| = \Lambda/t$. Take t to be width of the sample $\theta \cong 1^\circ 30'$ for $V_p[100]$ measurements, 1° for $V_s[100]$ measurements, 2° for $V_p[110]$ measurements, and $0^\circ 50'$ for $V_s[110]$ measurements. Since the characteristic curve (Hurter-Driffield curve) of the Agfa-Gavaert 8E75 and 10E75 plates shown in Figure I.5-9 is such that exposure for energy density below the "toe" is greatly depressed, the effective angular range in which

light diffracted from these waves is recorded on the photographic plate is even less than the angles listed above. Nevertheless, this does have the effect of causing disparity between the two density profiles and explains also why in case of disparity, the match between one density profile with mirror image of the other profile is better than the match between the two profiles themselves.

The data interpreted as described above are listed in Tables I.5-1 through I.5-4. Each table provides data for velocity measurement as a function of temperature of a pure mode. There are two spot separation readings for each photographic plate. The first reading is the separation when matching the top part of the two profiles and the second reading is the separation when matching bottom part of the two profiles. The first reading is not consistently greater than the second, nor is it true vice versa. It depends rather on the detailed excitation of off-pure mode plane waves which in turn depends on exact sample geometry, positioning of transducer, transducer driving frequency, and temperature gradient inside the sample. In computing these distances, the distance between the fixed markers is taken as the calibrated distance shown on the stage micrometer. Any error in this distance affects only the absolute velocity but not the temperature dependence of velocity measurements. In summary, the errors discussed in the measurement of the distance between the two spots on the photographic plates by the microdensitometer readout are:

(1) Error due to microdensitometer and stage micrometer misalignment. This is about $\sim$0.1 μm;

(2) Pencil marker and recorder pen trace thickness on the

microdensitometer readout chart. This error is less than 1 μm;

(3) Reproducibility of microdensitometer readout, which is within 2.5 μm.

(4) The error involved when the direction defined by the two spots, relative to the photographic plate bottom edge, fluctuates from plate to plate. This error is typically one order of magnitude smaller than and at most one-fifth of the uncertainty in profile matching.

(5) Error involved in profile matching, on the average $\sim$ 5 μm.

Item (1) is negligible compared to item (5). Items (2) and (3) have a Gaussian probability distribution and their contribution to the standard deviation of temperature dependence of velocity is negligible compared to item (5). Item (4) is one order of magnitude smaller than item (5), which leaves item (5) as the major contributing factor in experimental error.

Note also in Table I.5-1, D-2, D-4, D-5, D-6, and D-7 all measure the same velocity at room temperature, only that the D-5, D-6, D-7 measurements have one more half-wavelength inside the sample than the D-2, D-4 measurements. Also in Table I.5-2, E-14, E-16, E-17 all measure the velocity at nearly the same temperature, but E-14 has a slightly different frequency than E-16 and E-17. This is also the case in Table I.5-3 between F-1, F-2, and F-6. These variations are used to check if this method would depend on the number of half wavelengths inside the sample, or the selection of transducer driving frequency. From the readings of the ratio of transducer driving frequency and spot

separation as listed in Tables I.5-1 to I.5-4, these factors do not show any effect within the experimental error. It should also be noted that the effect of random index of refraction fluctuation along the partially evacuated light path has not been taken into account in the data analysis. Figures I.5-10 to I.5-13 are plots of the ratio of transducer driving frequency and spot separation vs. temperature constructed from Tables I.5-1 to I.5-4, respectively. In these figures the short end of each error bar indicates density profile matching by top, while the long end indicates density profile matching by bottom.

A linear temperature dependence is fit to the quantity f/ℓ in Figures I.5-10 through I.5-13 by a least square method. The method is to minimize the sum of the distance from center of each error bar to the straight line squared. The intercept at $0^{o}C$ and slope of each least square fit straight line are labeled in each figure.

The standard deviation of the parameters of any least square fit scheme depends on the meaning of error bar at each individual data point. For example, if the error bar represents one standard deviation of a Gaussian distribution from repeated measurements at the same given value of the independent variable, the standard deviation of the parameters in the least square fit can be calculated, for example, according to Mathews and Walker (1965a). The error bars in the present case, as explained earlier, however, represent the latitude in the matching of the two density profiles, and the probability distribution inside the error bars is not necessarily Gaussian. The assignment of standard deviation to the parameters is therefore difficult. Instead,

a measure of uncertainty in these parameters is assigned by a consistency check which will be discussed later.

Before computing the velocity and its temperature dependence from these results, two more possible sources of error must be considered. The first is error in temperature measurement. As stated in the Experimental Techniques section, the temperatures are measured at two sites located at diagonally opposite corners of the sample. Each temperature reading listed in Tables I.5-1 through I.5-4 is an average of the temperatures at the two thermocouple sites. At room temperature the two thermocouples give identical readings. At higher temperatures the two readings differ. This difference is $\sim 5^{o}C$ at $150^{o}C$. The cause for this difference is that the center of the sample holder assembly deviates slightly from the furnace center. This means that the temperature reading is uncertain to $\pm 2.5^{o}C$ at $150^{o}C$. Since room temperature is $\sim 20^{o}C$ for all measurements, this would introduce an error of $\pm 2.5^{o}/130^{o} = \pm 2\%$ to the slopes in Figures I.5-10 through I.5-13. Another possible source of error comes from the lensing effect at the exit sample face if a radial temperature gradient exists in the furnace. A separate test is conducted to determine the upper limit of this radial thermal gradient. A fused silica 1 cm x 1 cm x 1 cm is placed inside the furnace in place of the spinel sample. A third thermocouple is pasted at the center of the exit face (face toward the shutter) by Sauereisen cement. At $\sim 100^{o}C$, the three thermocouple readings are 1.466 mV (thermocouple at one corner of the exit face), 1.660 mV (thermocouple at the diagonally opposite corner) and 1.256 mV

(thermocouple at center of the exit face). Since 0.1 mV corresponds to $2.22^{o}C$ and since the third thermocouple, placed inside the tubular furnace, provides a conduction path between high temperature region of the furnace and low temperature region outside the furnace (which is absent during the optical measurement), the maximum radial temperature difference existing in the optical measurement is estimated to be $4.44^{o}C \times \frac{3.25}{22.65} = 0.63^{o}C$ at $\sim 100^{o}C$. 3.25/22.65 is the ratio of thermal conductivity of fused silica and spinel (Horai 1971). The lensing effect of the exit face can be estimated as the following. Refer to Figure I.5-14, $x = 6.93 \times 10^{-6} \Delta T$, where $6.93 \times 10^{-6}/K$ is the linear thermal expansion coefficient of spinel (Rigby et al 1946), $b = 0.8$ cm is the distance between corner thermocouple and center thermocouple. The curvature a is given by $a = b^2/2x = 0.64/(2 \times 6.93 \times 10^{-6} \Delta T)$. The change in diffraction angle due to lensing effect is then (for example, Yariv 1971a) $\Delta\theta = (n_{spinel} - 1) \frac{r}{a} = 0.719 \frac{r}{a} = 15.6 \times 10^{-6} r\Delta T$. The corresponding change in spot separation on the photographic plate is $\Delta\ell = L\Delta\theta = 15.6 \times 10^{-6} r\Delta TL$, where L is the distance between sample and photographic plate. Take $V_s[001]$ measurement, for example, $r = \frac{\lambda_o}{\Lambda} \times 1.179 \text{ cm} = \frac{0.6328 \times 10^{-4} \times 30.85 \times 10^{6}}{6.57 \times 10^{5}} \times 1.179 \text{ cm} = 3.50 \times 10^{-3}$cm, $L = 257.7$ cm, $\Delta\ell = 1.41 \times 10^{-5} \Delta T$ cm/^{o}C, $\ell = 1.54$ cm, $\Delta\ell/\ell = 0.91 \times 10^{-5} \Delta T$. With $\frac{d(f/\ell)/dT}{(f/\ell)} = 0.22 \times 10^{-4}$ ^{o}C, the lensing effect introduces an error of $\frac{0.91 \times 10^{-5}}{0.22 \times 10^{-4}} \times \frac{0.63}{80} = 0.3\%$ between room temperature and $100^{o}C$. This is neglected in comparison with other sources of error.

The velocity and its temperature dependence are computed from the values f/ℓ by the equations

$$v = f\Lambda = (L + \frac{t}{2n_{spinel}})\ 2\lambda_o(\frac{f}{\ell}) \qquad (I.5\text{-}1)$$

where t is the sample thickness;

λ_o is the laser wavelength in vacuum, $\lambda_o = 0.6328\ \mu m$, the stability of He-Ne wavelength is within $\Delta\lambda_o/\lambda_o = \Delta f/f = \frac{1.5 \times 10^9}{4.74 \times 10^{14}} = 3.16 \times 10^{-6}$, Δf being He-Ne laser Doppler width,

and

$$\frac{\partial v}{\partial T})_p = (L + \frac{t}{2n_{spinel}})\ 2\lambda_o\ \frac{\partial(f/\ell)}{\partial T})_p \qquad (I.5\text{-}2)$$

The values of velocity of the four pure modes at 25^oC and their temperature derivatives, together with values of L and t are listed in Table I.5-5.

The four pure mode velocities are given by

$$v_1 \equiv v_p[001] = \sqrt{C_{11}^s/\rho} \quad , \quad v_2 \equiv v_s[001] = \sqrt{C_{44}^s/\rho} \qquad (I.5\text{-}3)$$

$$v_3 \equiv v_p[110] = \sqrt{(C_{11}^s + C_{12}^s + 2C_{44}^s)/2\rho}\ ,$$

$$v_4 \equiv v_s[110](P // [1\bar{1}0]) = \sqrt{\frac{C_{11}^s - C_{12}^s}{2\rho}}$$

where C_{11}^s, C_{12}^s and C_{44}^s are the three adiabatic elastic constants of spinel and ρ its density.

It follows from equation (I.5-3) that

$$v_1^2 + v_2^2 = v_3^2 + v_4^2 \qquad \text{(I.5-4)}$$

and

$$v_1 \frac{\partial v_1}{\partial T})_p + v_2 \frac{\partial v_2}{\partial T})_p = v_3 \frac{\partial v_3}{\partial T})_p + v_4 \frac{\partial v_4}{\partial T})_p \qquad \text{(I.5-5)}$$

These two equations serve for consistency check of the experimental results. From Table 5, $v_1^2 + v_2^2 = (78.65 + 43.12)\text{km}^2/\text{sec}^2 = 121.77\ \text{km}^2/\text{sec}^2$, and $v_3^2 + v_4^2 = (104.01 + 17.73)\text{km}^2/\text{sec}^2 = 121.74\ \text{km}^2/\text{sec}^2$, the agreement is within 0.03%. The reason that the consistency check shows a closer agreement than the individual errors in velocity (as listed in Table 5) would indicate that the major contribution to the individual errors in Table 5 comes from the systematic calibration error of A01400 stage micrometer which contributes only to the second order in error in a consistency check. For the consistency check on temperature derivatives of velocity, Table I.5-5 gives $v_1(\frac{\partial v_1}{\partial T})_p + v_2(\frac{\partial v_2}{\partial T})_p = -(27.85 + 9.65) \times 10^{-4}\text{km}^2/\text{sec}^2\text{K} = -37.50 \times 10^{-4}\text{km}^2/\text{sec}^2\text{K}$, and $v_3(\frac{\partial v_3}{\partial T})_p + v_4(\frac{\partial v_4}{\partial T})_p = -(32.64 \pm 8.72) \times 10^{-4}\text{km}^2/\text{sec}^2\text{K} = -41.36 \times 10^{-4}\text{km}^2/\text{sec}^2\text{K}$. The disagreement is 9.6%. It has been remarked previously that it is difficult in the present experiment to ascertain the standard deviation of the temperature derivatives from individual error bars. The consistency check provides an alternative way to assign a measure of experimental uncertainty to these temperature derivatives. The disagreement between $v_1(\frac{\partial v_1}{\partial T})_p + v_2(\frac{\partial v_2}{\partial T})_p$ and $v_3(\frac{\partial v_3}{\partial T})_p + v_4(\frac{\partial v_4}{\partial T})_p$ is 9.6%. Since the absolute value of velocities v_1, v_2, v_3 and v_4 are accurate to better than 0.1%, the disagreement can be considered to arise from the velocity derivatives alone. Note

also that in Figures I.5-10 through I.5-13 the four temperature derivatives have different errors. A strategy to assign weighing factors to these temperature derivatives is as follows: Assume that the error involved in profile matching is the same for all four velocity measurements. A check on the spot separation column in Tables I.5-1 through I.5-4 indicates this to be a good approximation. Denote this matching error by ε. The percentage error in slope of the quantity f/ℓ vs. T in Figures I.5-10 through I.5-13 (which is also the percentage error of $(\frac{\partial v}{\partial T})_p$) is then $|(f/\ell)\,\frac{\varepsilon}{\ell}\Big/[(\frac{f}{\ell})_{150^oC} - (\frac{f}{\ell})_{20^oC}]|$. From this expression, the percentage error for $(\partial v_1/\partial T)_p$ is calculated to be 217ε; that for $(\partial v_2/\partial T)_p$ 342ε; for $(\partial v_3/\partial T)_p$ 245ε; and for $(\partial v_4/\partial T)_p$ 156ε. Let $[(217)^2 + (342)^2 + (245)^2 + (156)^2]^{1/2}\varepsilon = \pm 9.6\%$. Solving for ε, the resulting percentage errors for the four velocity temperature derivatives are $\pm 4.2\%$ for v_1, $\pm 6.6\%$ for v_2, $\pm 4.7\%$ for v_3, and $\pm 3.0\%$ for v_4. These values are certainly allowed within the error bars as indicated in Figures I.5-10 through I.5-13. The adiabatic elastic constants C_{11}^S, C_{12}^S, C_{44}^S and the adiabatic bulk modulus $K^S = \frac{1}{3}(C_{11}^S + 2C_{12}^S)$ of spinel can be calculated from equation (I.5-3) with $\rho = 3.5784$ gm/cm^3 at 25°C. The temperature derivative of the elastic constants are calculated from

$$\frac{\partial C_i^S}{\partial T})_p = \rho v_i[2(\frac{\partial v_i}{\partial T})_p - 3\alpha v_i] \qquad i=1,2,3,4 \qquad \text{(I.5-6)}$$

where α is linear thermal expansion coefficient.

$$C_1^S \equiv C_{11}^S \ , \ C_2^S \equiv C_{44}^S \ , \ C_3^S \equiv \frac{1}{2}(C_{11}^S + C_{12}^S + 2C_{44}^S), \text{ and } C_4^S \equiv \frac{1}{2}(C_{11}^S - C_{12}^S)$$

The temperature derivative of the adiabatic bulk modulus is calculated from

$$\frac{\partial k^S}{\partial T})_p = \frac{1}{3}\left[\left(\frac{\partial C_{11}^S}{\partial T}\right)_p + 2\left(\frac{\partial C_{12}^S}{\partial T}\right)_p\right] \qquad \text{(I.5-7)}$$

These values are listed in Table I.5-6.

TABLE I-5-1

Experimental Data for Determination of $V_p(001)$ and Its Temperature Dependence

Photographic Plate Designation	Vacuum Gauge Reading (μm)	Temperature (°C)	Transducer Driving Frequency (MHz)	Microdensitometer Table Angle Reading (Degree)	Spot Separation (cm)	Ratio of Transducer Driving Frequency and Spot Separation (MHz/cm)
D-2	130	20.29	28.87804	21.75	1.0628	27.171
					1.0623	27.183
D-3	120	20.34	28.87804	21.75	1.0624	27.182
					1.0619	27.195
D-5	130	20.49	29.37592	21.75	1.0803	27.193
					1.0797	27.208
D-6	150	21.67	29.37592	21.75	1.0796	27.210
					1.0802	27.196
D-7	100	20.07	29.37592	21.75	1.0805	27.188
					1.0809	27.177
D-8	150	57.08	29.34020	21.75	1.0805	27.155
					1.0812	27.136
D-9	150	59.83	29.34020	21.75	1.0806	27.152
					1.0820	27.117
D-10	150	80.64	29.31250	21.75	1.0807	27.125
					1.0801	27.139
D-11	150	80.09	29.31250	21.75	1.0822	27.087
					1.0813	27.110
D-12	175	119.33	29.26488	21.70	1.0806	27.083
					1.0796	27.108
D-13	175	120.50	29.26488	21.70	1.0805	27.084
					1.0799	27.099
D-14	175	145.83	29.23100	21.60	1.0792	27.087
					1.0803	27.059
D-15	180	146.80	29.23100	21.60	1.0801	27.063
					1.0796	27.075
D-17	90	80.93	28.81502	21.75	1.0625	27.120
					1.0622	27.128

TABLE I-5-2

Experimental Data for Determination of $V_s\langle 001\rangle$ and Its Temperature Dependence

Photographic Plate Designation	Vacuum Gauge Reading (μm)	Temperature (°C)	Transducer Driving Frequency (MHz)	Microdensitometer Table Angle Reading (Degree)	Spot Separation (cm)	Ratio of Transducer Driving Frequency and Spot Separation (MHz/cm)
E-2	130	21.81	30.95130	22.60	1.5398	20.101
					1.5391	20.109
E-4	140	21.92	30.95130	22.60	1.5391	20.111
					1.5388	20.115
E-5	115	21.95	30.95130	22.60	1.5400	20.099
					1.5395	20.105
E-6	105	21.59	30.95130	22.60	1.5386	20.116
					1.5390	20.111
E-8	110	49.22	30.92020	22.40	1.5381	20.102
					1.5378	20.107
E-9	120	49.37	30.92020	22.60	1.5384	20.099
					1.5377	20.108
E-11	125	80.44	30.89004	22.60	1.5377	20.089
					1.5374	20.092
E-12	100	80.96	30.89004	22.60	1.5374	20.093
					1.5369	20.099
E-13	100	80.81	30.89004	22.40	1.5380	20.084
					1.5376	20.089
E-14	130	120.90	30.83805	22.40	1.5375	20.057
					1.5380	20.051
E-16	130	118.91	30.84604	22.50	1.5366	20.075
					1.5372	20.066
E-17	100	118.89	30.84604	22.40	1.5392	20.041
					1.5377	20.060
E-19	150	145.08	30.81604	22.60	1.5353	20.071
					1.5369	20.051
E-20	130	146.17	30.81604	22.50	1.5359	20.064
					1.5364	20.057

TABLE I-5-3

Experimental Data for Determination of $V_p(110)$ and Its Temperature Dependence

Photographic Plate Designation	Vacuum Gauge Reading (μm)	Temperature (°C)	Trancducer Driving Frequency (MHz)	Microdensitometer Table Angle Reading (Degree)	Spot Separation (cm)	Ratio of Transducer Driving Frequency and Spot Separation (MHz/cm)
F-1	120	18.50	30.96020	18.60	0.9918	31.216
					0.9927	31.188
F-2	100	18.57	30.96020	18.60	0.9921	31.208
					0.9925	31.196
F-3	110	49.95	30.94500	19.20	0.9930	31.162
					0.9927	31.173
F-4	95	49.31	30.94500	19.20	0.9927	31.171
					0.9938	31.140
F-5	100	49.04	30.94500	19.20	0.9932	31.157
					0.9926	31.177
F-6	95	17.87	30.97000	18.60	0.9927	31.199
					0.9932	31.183
F-7	120	78.46	30.91620	19.20	0.9939	31.105
					0.9930	31.135
F-8	130	79.13	30.91620	19.20	0.9922	31.160
					0.9927	31.144
F-10	130	113.53	30.88058	19.20	0.9925	31.114
					0.9929	31.102
F-11	140	113.49	30.88058	19.20	0.9926	31.112
					0.9928	31.104
F-12	150	145.98	30.84830	18.60	0.9929	31.069
					0.9934	31.053
F-13	150	147.87	30.84830	18.60	0.9924	31.086
					0.9929	31.070

TABLE I-5-4

Experimental Data for Determination of $V_s\{110\}$ ($P//\{1\bar{1}0\}$) and Its Temperature Dependence

Photographic Plate Designation	Vacuum Gauge Reading (μm)	Temperature (°C)	Transducer Driving Frequency (MHz)	Microdensitometer Table Angle Reading (Degree)	Spot Separation	Ratio of Transducer Driving Frequency and Spot Separation (MHz/cm)
G-4	140	17.09	31.10572	20.40	2.4128	12.892
					2.4136	12.888
G-5	130	16.37	31.10572	20.40	2.4134	12.889
					2.4139	12.886
G-6	120	48.12	31.05112	20.40	2.4140	12.863
					2.4144	12.861
G-7	140	47.81	31.05112	20.40	2.4136	12.865
					2.4142	12.862
G-8	110	48.29	31.05112	20.40	2.4156	12.855
					2.4149	12.858
G-9	90	80.62	30.99005	20.40	2.4119	12.849
					2.4116	12.851
G-10	100	80.40	30.99005	20.40	2.4141	12.837
					2.4133	12.841
G-11	100	119.02	30.93251	20.40	2.4125	12.822
					2.4117	12.826
G-12	85	118.90	30.93251	20.60	2.4110	12.830
					2.4111	12.829
G-13	115	149.05	30.87503	20.60	2.4128	12.796
					2.4132	12.795
G-14	120	149.11	30.87503	20.60	2.4122	12.800
					2.4120	12.801
G-15	110	149.29	30.87503	20.60	2.4117	12.802
					2.4122	12.799

TABLE I-5-5
Ultrasonic Velocities and Their Isobaric Temperature Derivatives of Spinel at 25°C

Mode	Velocity at 25°C, v (km/sec)	Isobaric Temperature Derivative, $(\partial v/\partial T)_p$ (10^{-4}km/sec-K)	Distance between Sample & Plate, L (cm)	Sample Thickness at 25°C, t (cm)
L// [001]	8.869	-3.14	257.46	1.1793
	±0.013	±0.13 (±4.2%)	±0.03	±0.0003
T// [001]	6.5666	-1.47	257.67	1.1793
	±0.0055	±0.10 (±6.6%)	±0.03	±0.0003
L// [110]	10.199	-3.20	258.36	0.8923
	±0.011	±0.15 (±4.7%)	±0.03	±0.0003
T// [110]	4.2101	-2.07	258.02	0.8923
(P// [1$\bar{1}$0])	±0.0043	±0.06 (±3.0%)	±0.03	±0.0003

The error in the absolute velocity includes Americam Optical Corporation A01400 stage micrometer calibration error, photographic density profile matching error, sample thickness measurement error, and error in length measurement between sample and photographic plate.
The uncertainties in isobaric temperature derivatives of velocity are assigned from consistency check.

TABLE I-5-6

Adiabatic Elastic Constants, Bulk Modulus, and Their Isobaric Temperature Derivatives

C_{11}^s (kb)	C_{44}^s (kb)	C_{12}^s (kb)	$K_s = \left(\frac{C_{11}^s + 2C_{12}^s}{3}\right)$ (kb)	$\left(\frac{\partial C_{11}^s}{\partial T}\right)_p$ (kb/K)	$\left(\frac{\partial C_{44}^s}{\partial T}\right)_p$ (kb/K)	$\left(\frac{\partial C_{12}^s}{\partial T}\right)_p$ (kb/K)	$\left(\frac{\partial K_s}{\partial T}\right)_p$ (kb/K)	α (10^{-6}/K)
2814 ±8	1543 ±3	1546* ±9	1969* ±6	-0.258 ±0.018	-0.101 ±0.01	-0.107* ±0.019	-0.157* ±0.014	6.93††
		1544† ±19	1967† ±13			-0.161† ±0.052	-0.193† ±0.035	

*Values calculated from $V_p^s // [110]$ ($P // [1\bar{1}0]$) measurement.
†Values calculated from $V_p^s // [110]$ measurement.
†† Linear thermal expansion coefficient from Rigby et al. (1946)

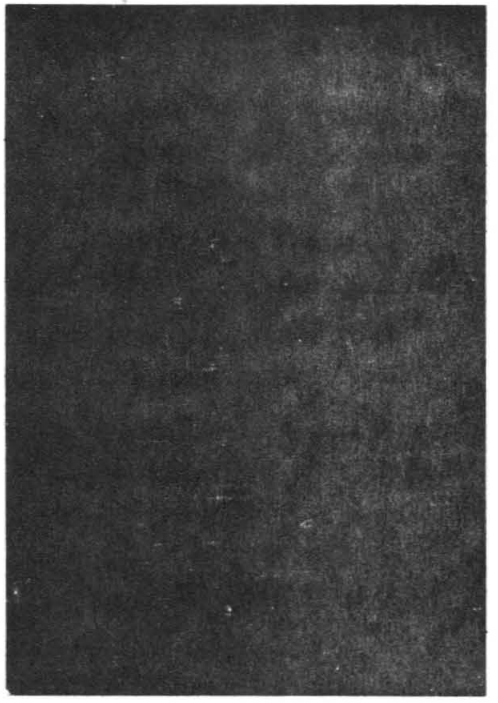

Figure I-5-1. Contact print made from a data photographic plate.

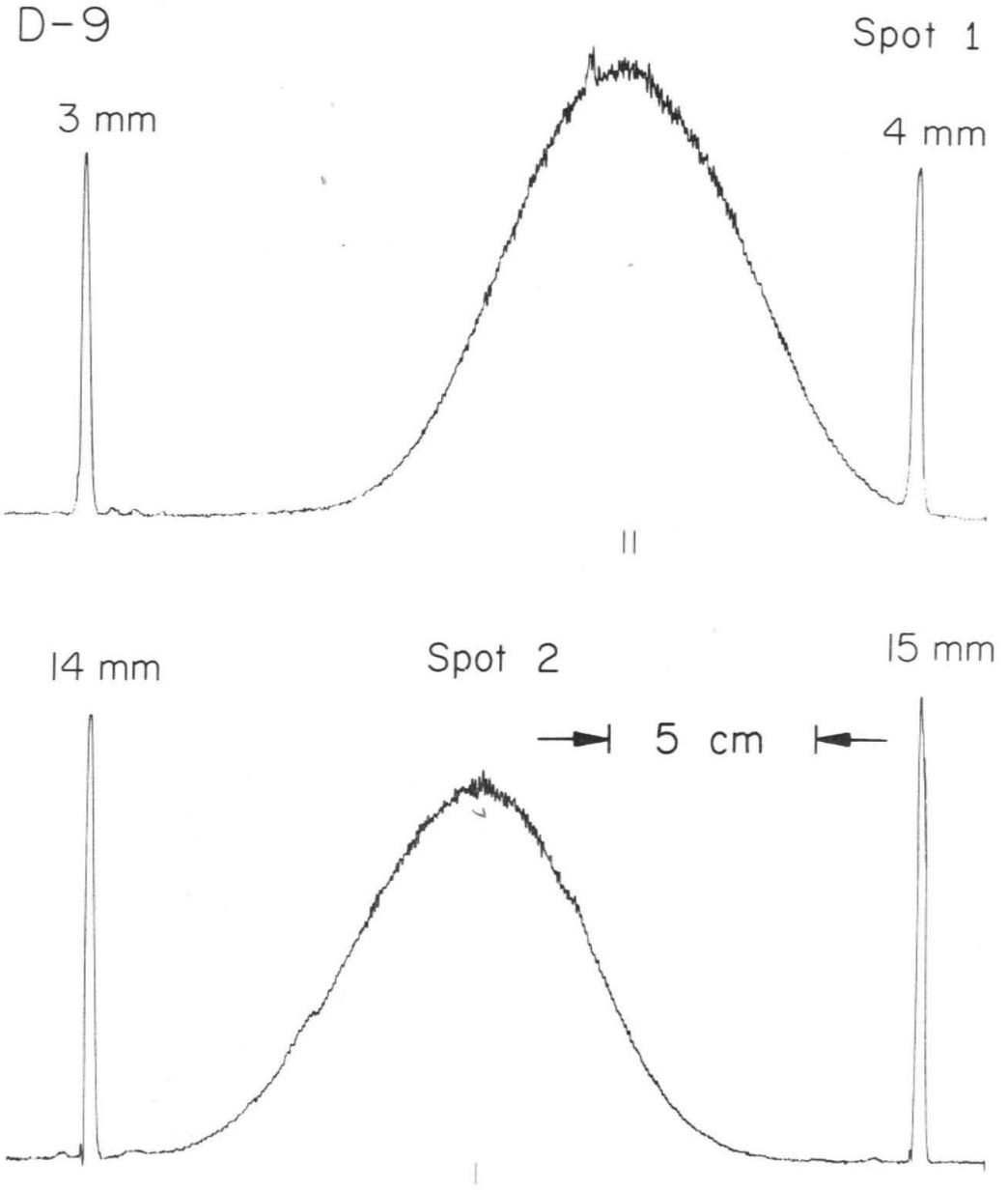

Figure I-5-2(a). Microdensitometer trace out of photographic plate D-9, spot 1.
(b). Microdensitometer trace out of photographic plate D-9, spot 2.

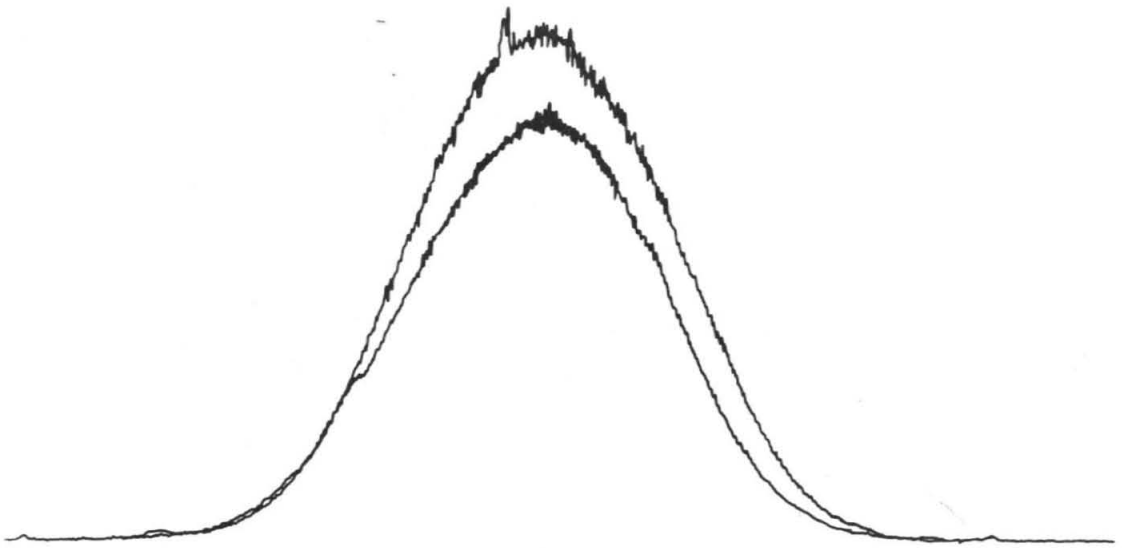

Figure I-5-3. Matching the two density profiles of photographic plate D-9 by top.

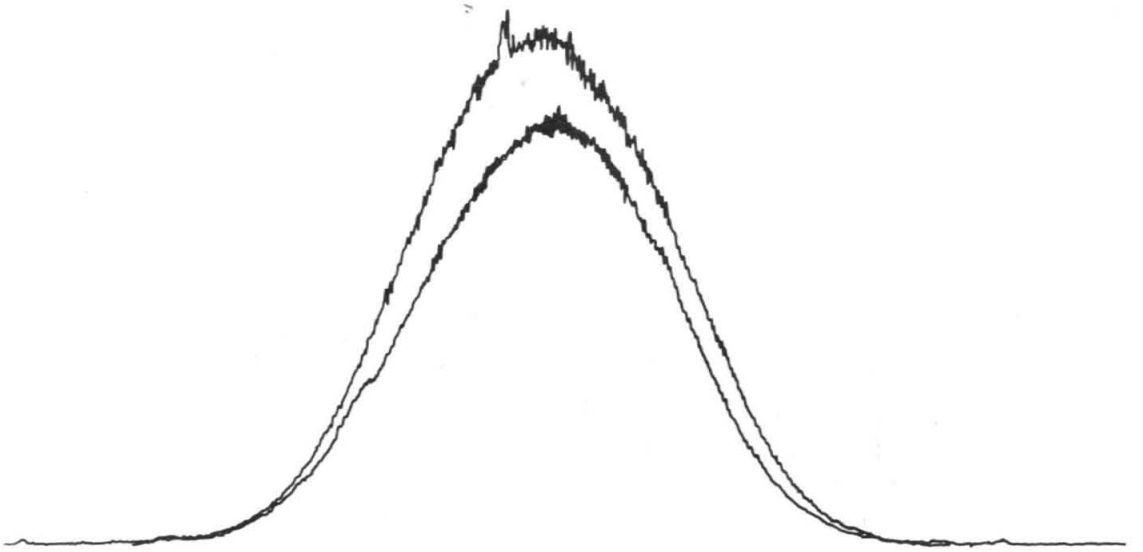

Figure I-5-4. Matching of the two density profiles of photographic plate D-9 by bottom.

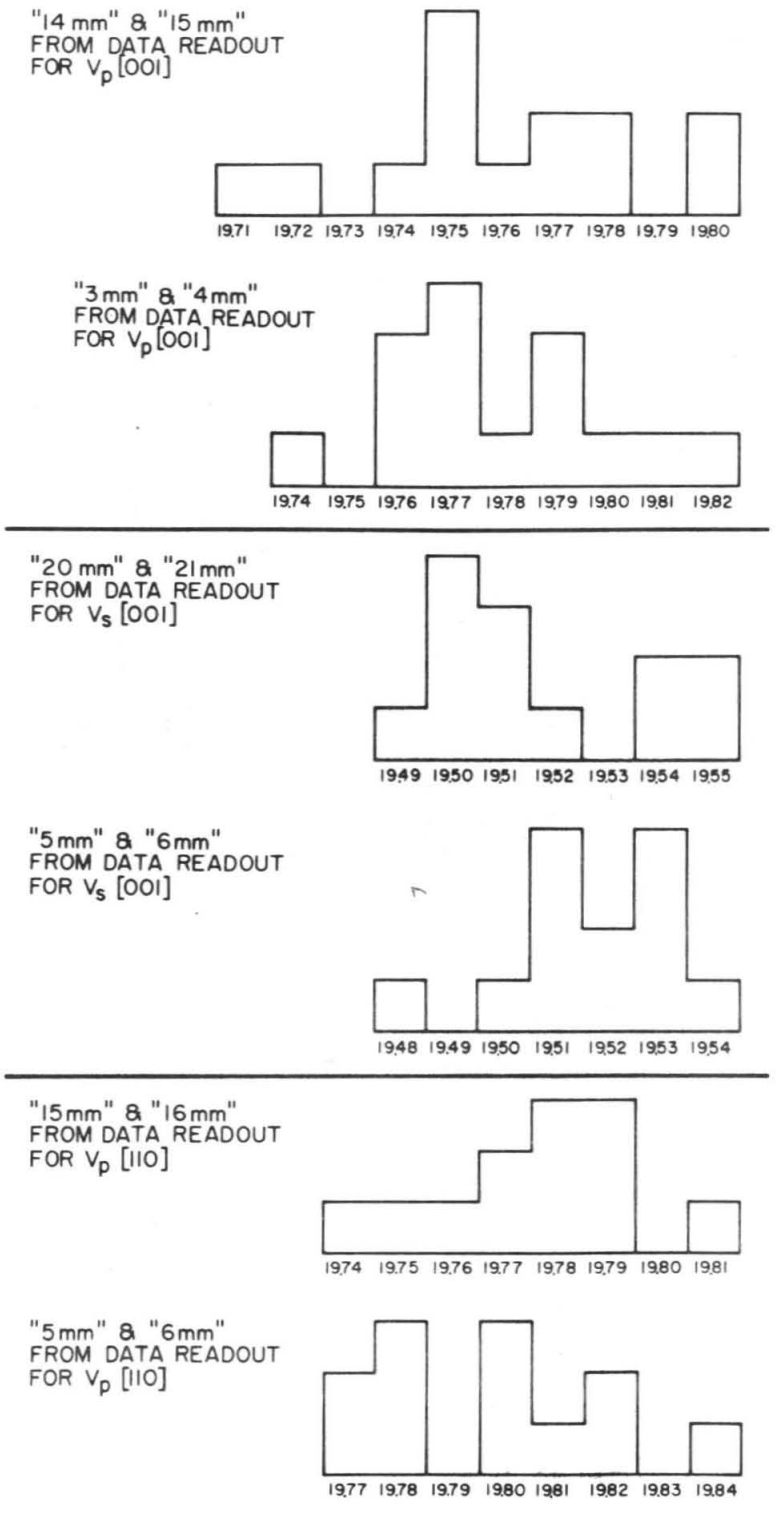

Figure I-5-5. Histogram giving a measure of reproducibity of density readout by a Joyce-Loebl MkIIICS microdensitometer.

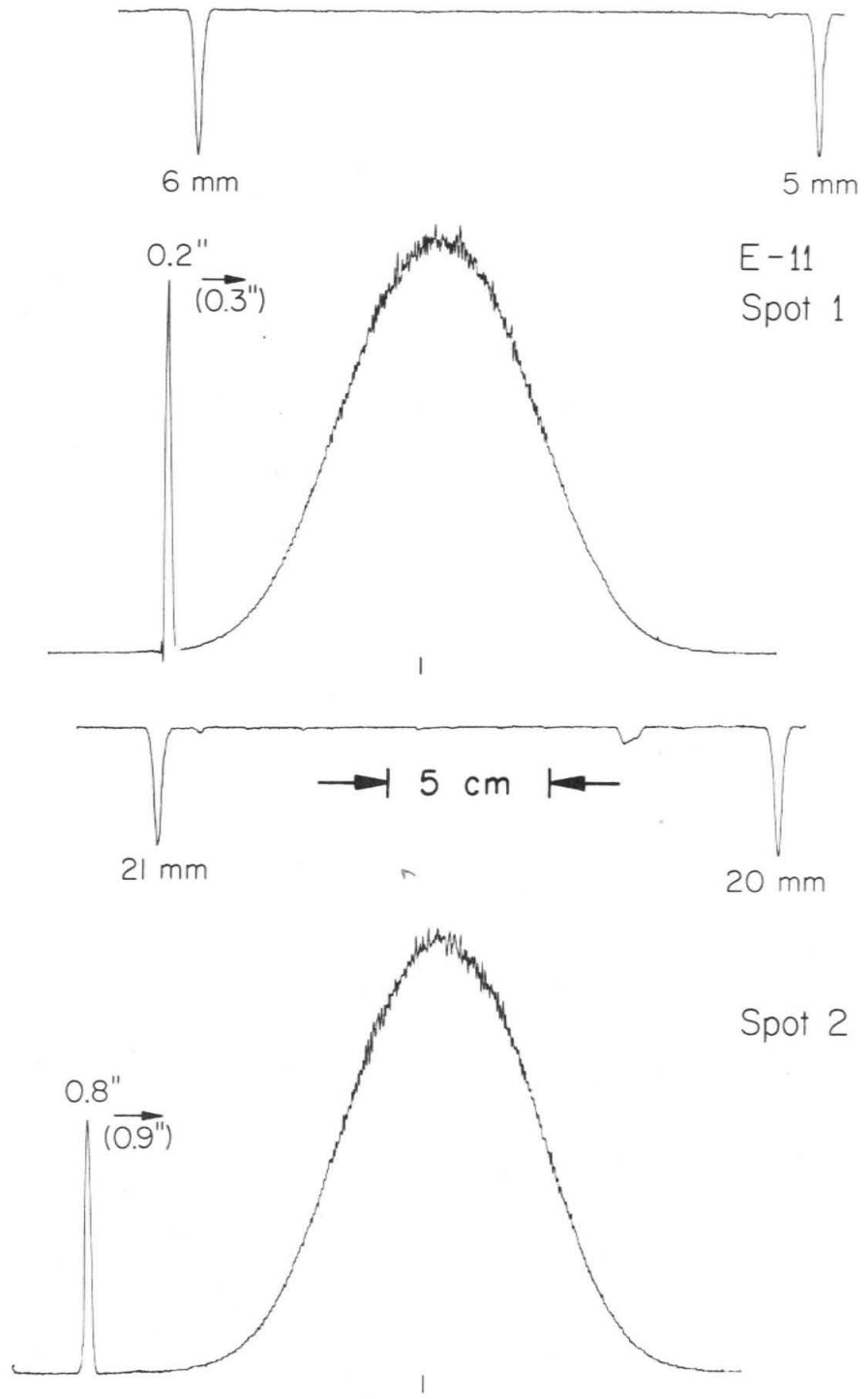

Figure I-5-6(a). Microdensitometer trace out of photographic plate E-11, spot 1.
(b). Microdensitometrr trace out of photographic plate E-11, spot 2.

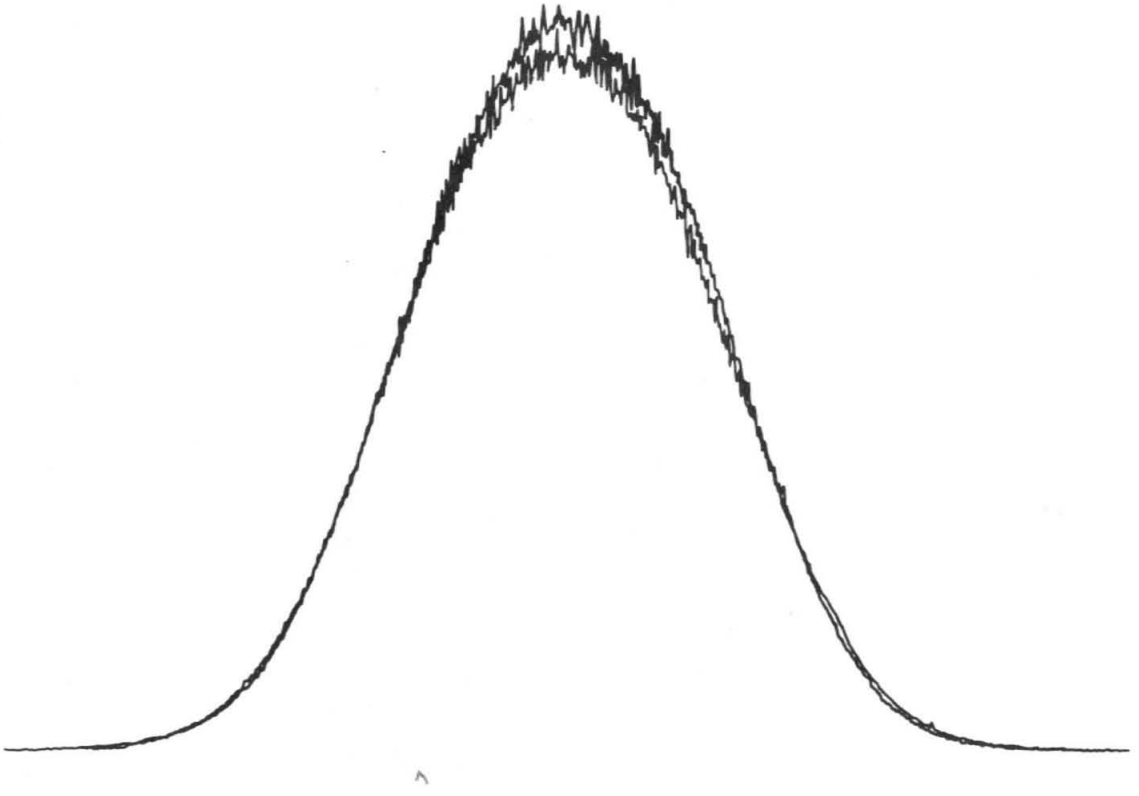

Figure I-5-7. Matching of the two density profiles of photographic plate E-11.

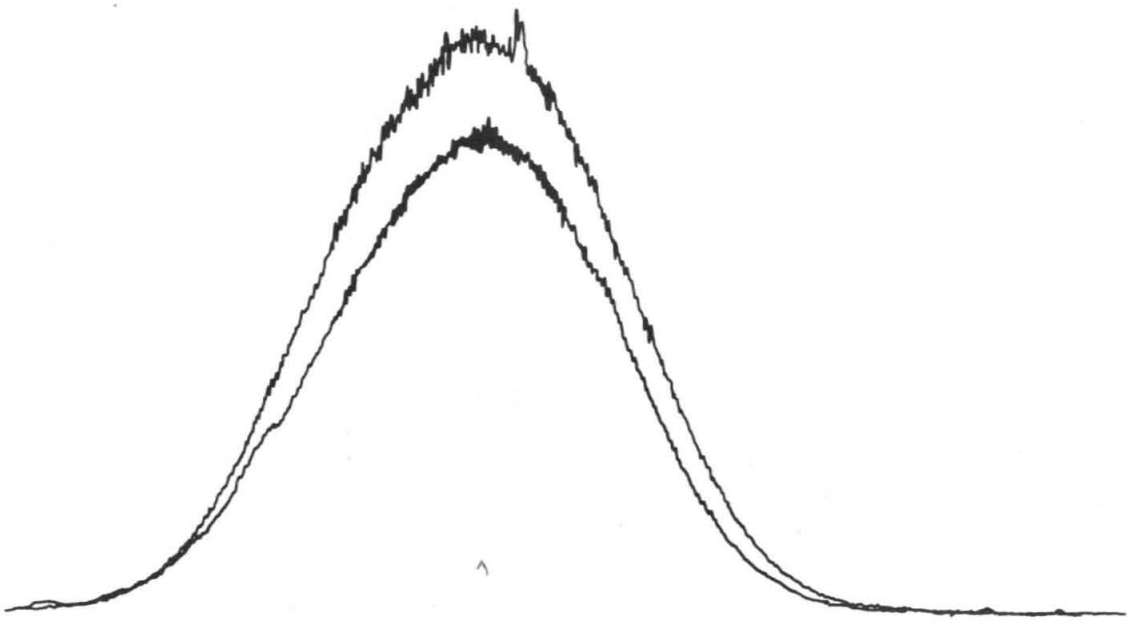

Figure I-5-8. Matching of one density profile of phtographic plate D-9 with the mirror image of the other density profile.

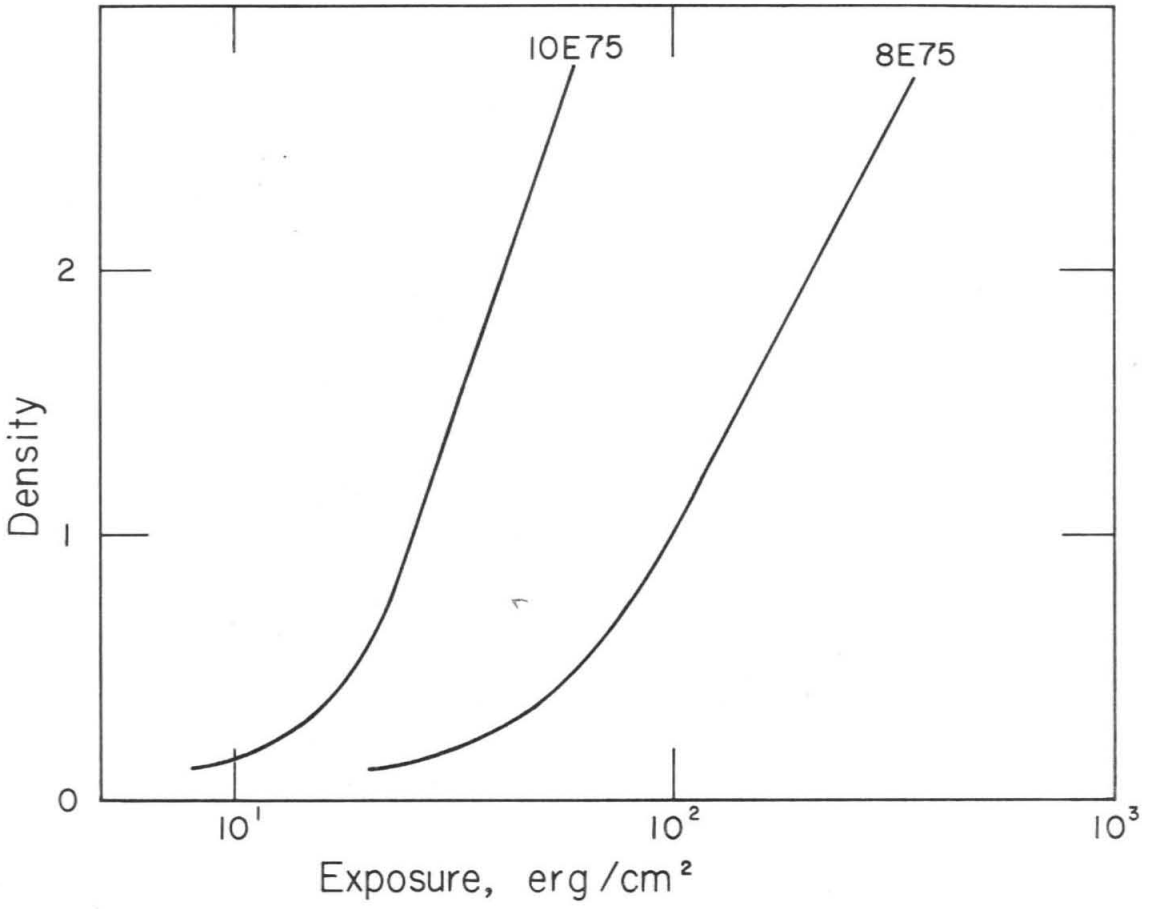

Figure I-5-9. Characteristic curve for Agfa-Gavaert film 8E75 and 10E75.

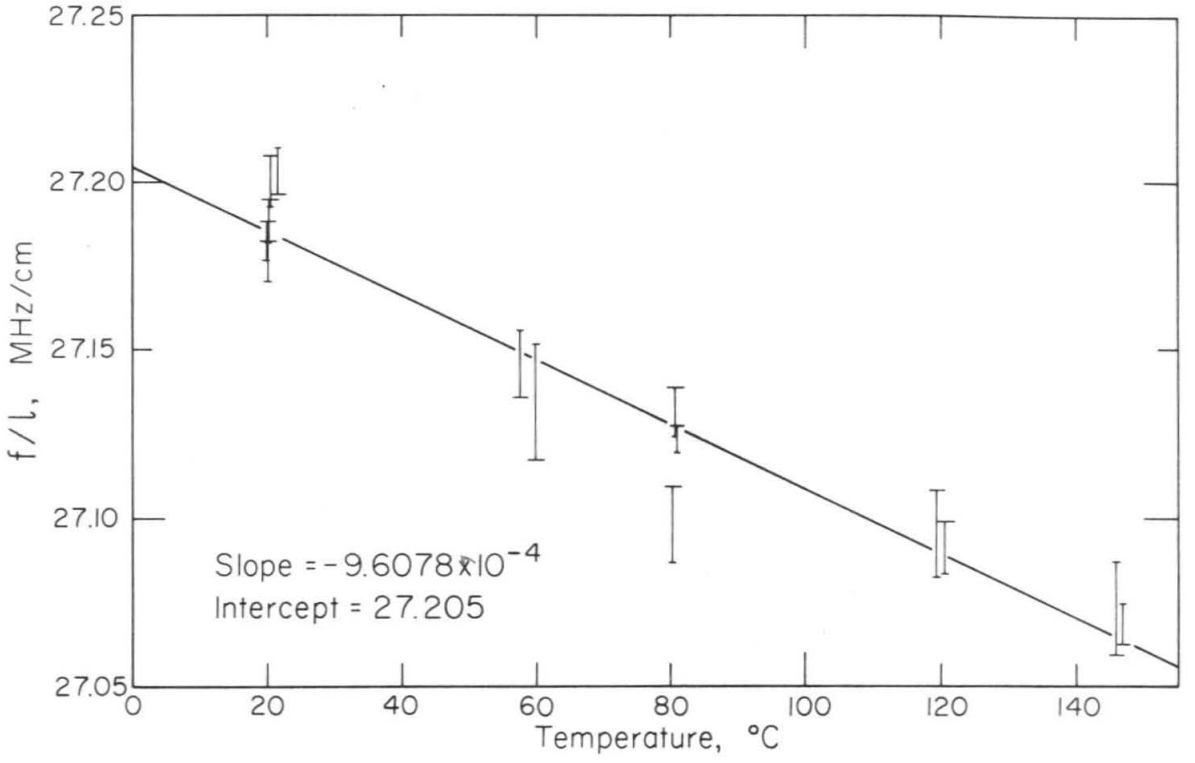

Figure I-5-10. Ratio of transducer driving frequency and spot separation vs. temperature for $V_p\langle 001\rangle$ measurements. The short end of each error bar indicates density profile matching by top. The long end indicates density profile matching by bottom.

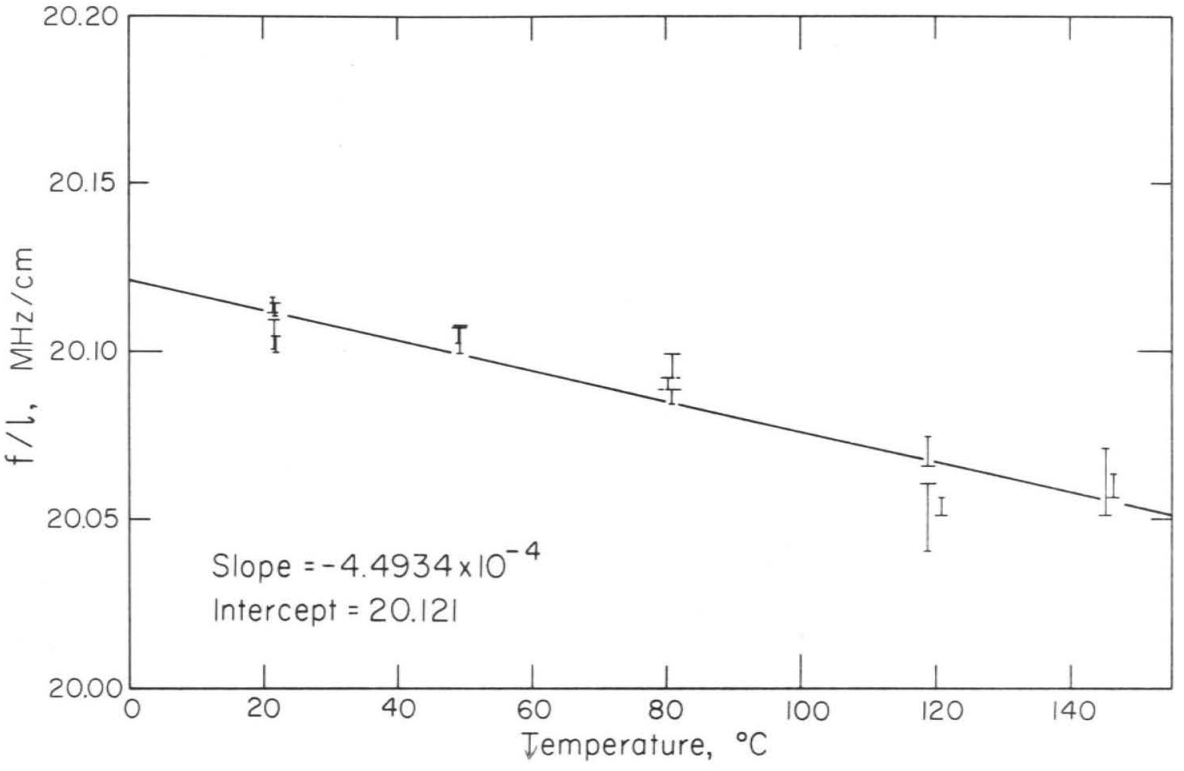

Figure I-5-11. Ratio of transducer driving frequency and spot separation vs. temperature for V_s [001] measurements. The short end of each error bar indicates density profile matching by top. The long end indicated density profile matching by bottom.

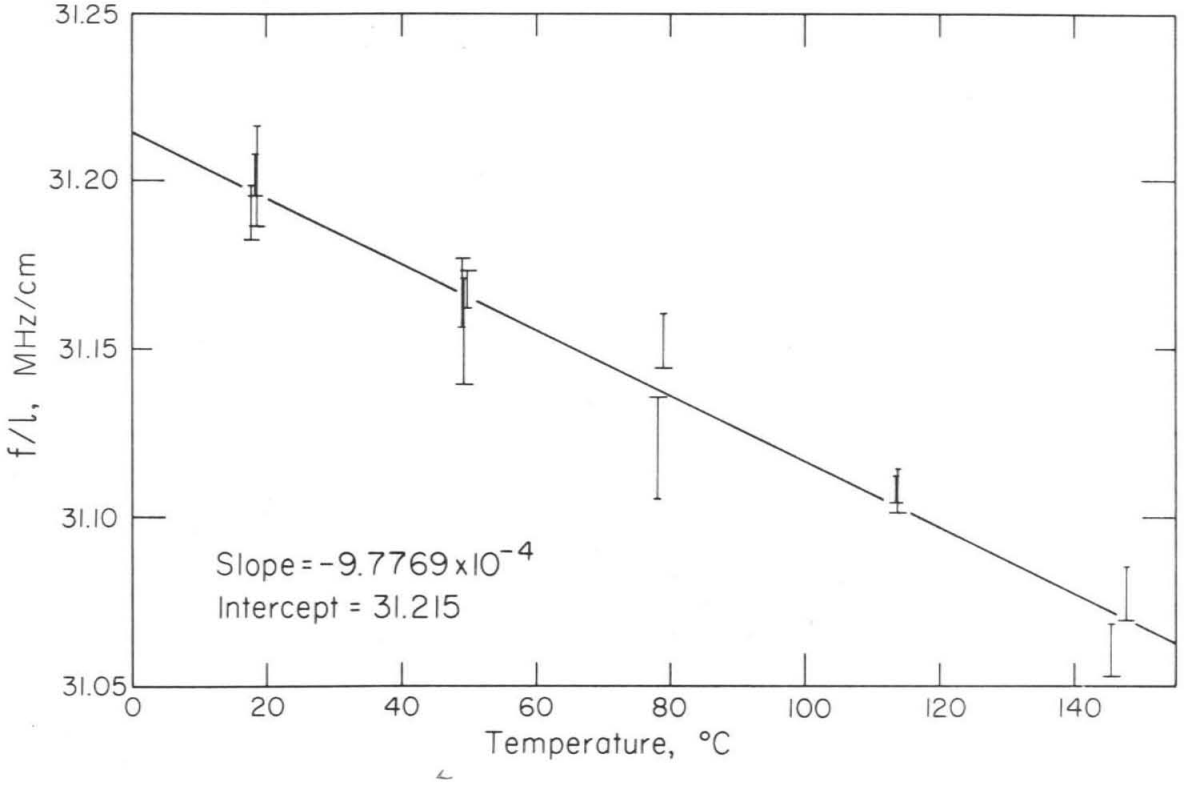

Figure I-5-12. Ratio of transducer driving frequency and spot separation vs. temperature for V_p (110) measurements. The short end of each error bar indicates density profile matching by top. The long end indicates density profile matching by bottom.

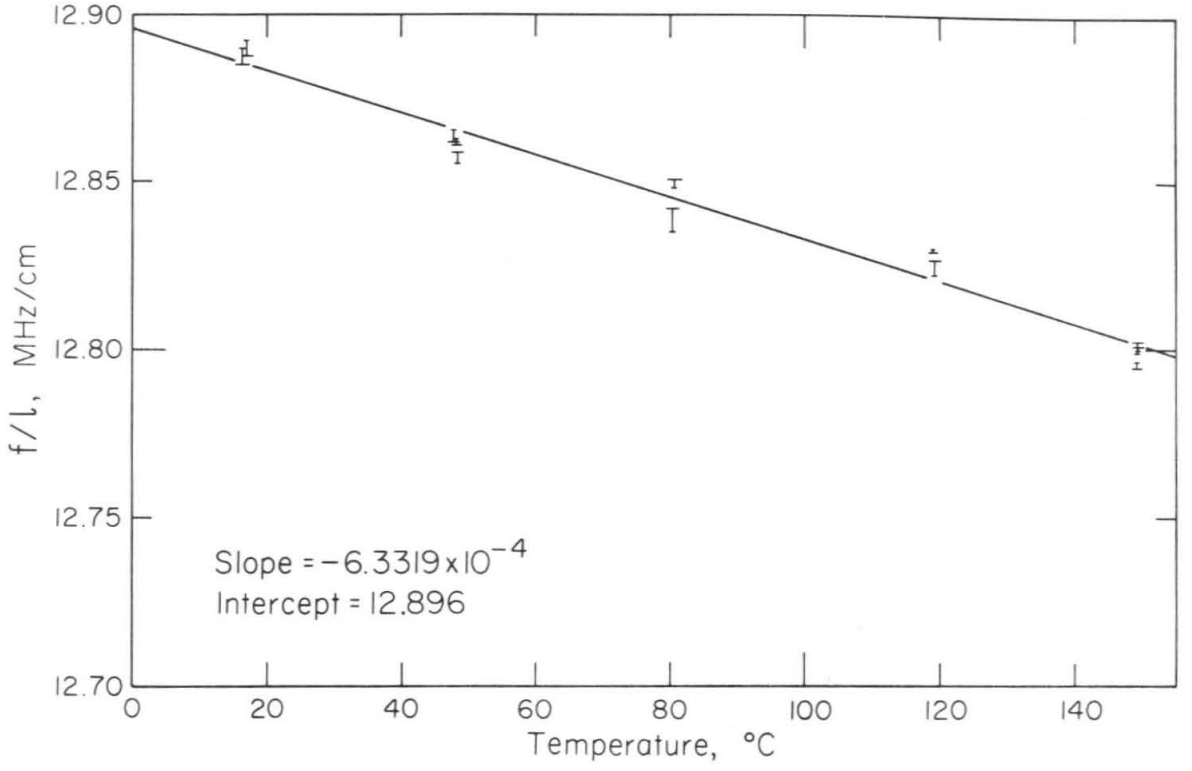

Figure I-5-13. Ratio of transducer driving frequency and spot separation vs. temperature for $V_S\{110\}(P//\{1\bar{1}0\})$ measurements. The short end of each error bar indicates density profile matching by top. The long end indicates density profile matching by bottom.

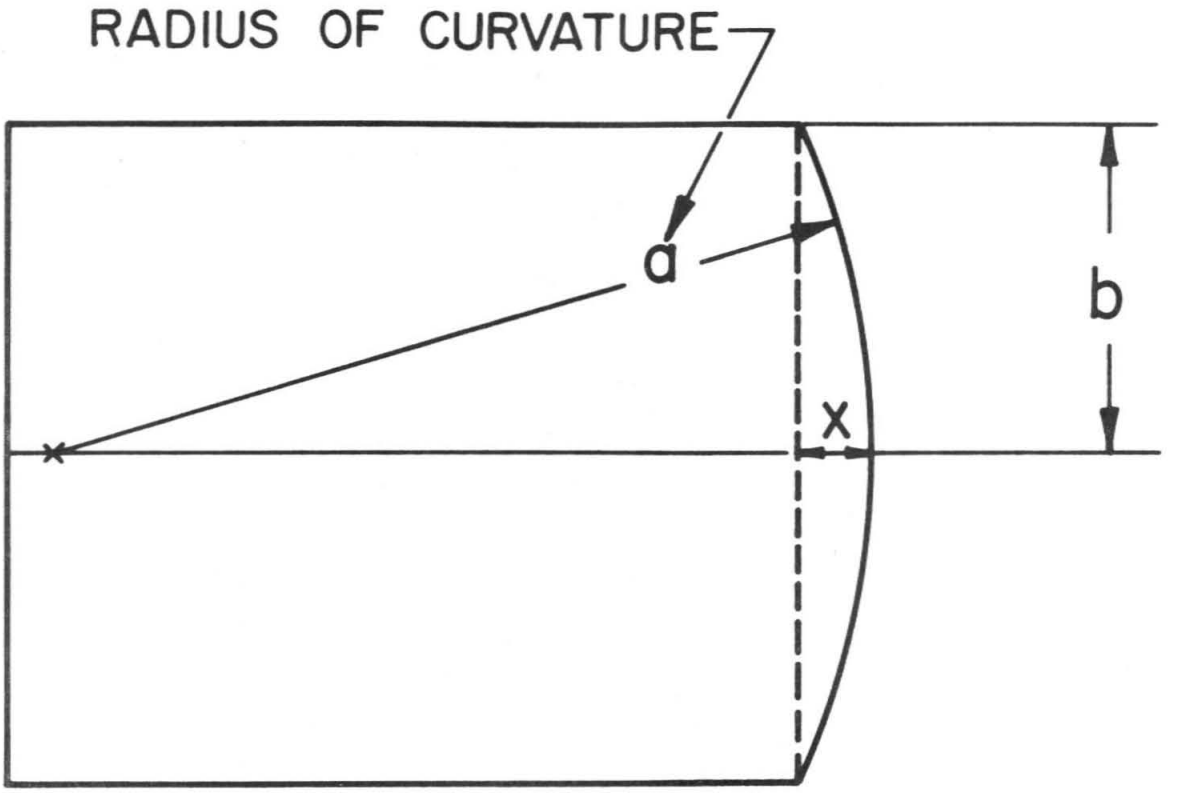

Figure I-5-14. Illustration of lensing effect of crystal face due to temperature gradient.

6. Data Interpretation and Comparison with Other Measurements on Single Crystal Spinel Elastic Constants and Their Temperature Dependence

In order to apply the temperature dependence data of single crystal elastic constants to the interpretation of Earth's mantle composition, the data must be put into several different forms and utilized in several calculations. The Debye temperature of single crystal spinel can be calculated from elastic constants according to methods summarized by Alers (1965). The calculated value is $\Theta_{spinel} = 883^{o}K$ using either de Launay's formula or Marcus' graph. The thermal Grüneisen's parameters are calculated to be:

$$\gamma_{th} = \frac{\beta K_s}{\rho C_p} = 6.93 \times 3 \times 10^{-6} \times 1969 \times 10^{9} \Big/ (3.5784 \times 0.815 \times 10^{7}) = 1.40 \quad \text{(I.6-1)}$$

for the first Grüneisen parameter, and

$$\delta_{th} = -\frac{1}{\beta K_s}\left(\frac{\partial K_s}{\partial T}\right)_p = 0.157/(6.93 \times 10^{-6} \times 1969 \times 3) = 3.84 \quad \text{(I.6-2)}$$

for the Anderson-Grüneisen parameter, where β is volume thermal expansion coefficient and $C_p = 0.815$ J/gm-K is the specific heat at constant pressure with the value given by Bonnickson (1955). The isothermal bulk modulus is given by

$$K_T = K_s(1 + T\beta\gamma_{th}) \quad \text{(I.6-3)}$$

and its temperature derivative is given by differentiating (I.6-3)

$$\left(\frac{\partial K_T}{\partial T}\right)_p = \left(\frac{\partial K_s}{\partial T}\right)_p (1 + T\beta\gamma_{th})^{-1} - k_s\gamma_{th}[1 + T\beta\gamma_{th}]^{-2} \left[\beta + T\left(\frac{\partial \beta}{\partial T}\right)_p\right] \qquad (I.6\text{-}4)$$

$\left(\frac{\partial \beta}{\partial T}\right)_p$ is measured to be $1.20 \times 10^{-8} K^{-1}$ by Rigby et al (1946). Anderson (1966) showed that for oxide compounds

$$\left(\frac{\partial K_s}{\partial T}\right)_p = - \frac{\gamma_{th}\delta_{th}}{V_o} C_v \qquad (I.6\text{-}5)$$

where V_o is the volume at absolute zero.

Anderson's derivation assumes that the thermal Grüneisen parameters are identical to the mode gammas in lattice dynamics and that the Grüneisen parameters are temperature independent. Chang and Barsch (1973) concluded that for single crystal spinel, the first assumption is bad. Based on Achar and Barsch (1971) and Barsch and Achar (1972), Chang and Barsch concluded that the second assumption in Anderson's derivation is valid for $T \simeq \frac{\Theta}{2}$. In short, equation (I.6-5) holds in the form

$$\left(\frac{\partial K_s}{\partial T}\right)_p \propto C_v \qquad \text{for } T \gtrsim \frac{\Theta}{2} \qquad (I.6\text{-}6)$$

independent of assumptions regarding Grüneisen parameters. Since

$$C_v = 3R[4D(x) - 3x(e^x - 1)^{-1}] \ , \ x = \Theta/T \qquad (I.6\text{-}7)$$

where $D(x)$ is the Debye function, and $C_v = 3R = 5.961$ cal/mol-K at high temperatures ($T >> \Theta$), equation (I.6-7) can be used to calculate the temperature dependence of bulk modulus at high temperatures. Take $\left(\frac{\partial K_s}{\partial T}\right)_p = -0.157 \pm 0.014$ kb-K^{-1}, at $T = \left(\frac{293 + 423}{2}\right) \pm 65K =$ $(358 \pm 65)K$, $\Theta/T = 2.47 \pm 0.45$, $C_v(\Theta/T) = 4.485 \pm 0.435$ cal/mol-K.

Substituting these values into equation (I.6-7),

$$\left(\frac{\partial K_S}{\partial T}\right)_p = -0.209 \pm 0.028 \text{ kb-K}^{-1} \quad \text{for} \quad T \gg \Theta \qquad \text{(I.6-8)}$$

The bulk modulus of spinel is identical for both single crystal and its polycrystalline aggregates. The shear modulus for a polycrystalline aggregates can be expressed in terms of Voigt, Reuss, and Hill averages. These and their temperature derivatives are calculated according to expressions given by Chung (1967):

$$\mu_V = \frac{1}{5}\left(C_{11}^S - C_{12}^S + 3C_{44}^S\right) = 1179 \text{ kb} \pm 3 \text{ kb}$$

$$\mu_R = 5(C_{11}^S - C_{12}^S)C_{44}^S/[3(C_{11}^S - C_{12}^S) + 4C_{44}^S] = 981 \text{ kb} \pm 10 \text{ kb}$$

$$\mu_{VRH} = \frac{1}{2}(\mu_V + \mu_R) = 1080 \text{ kb} \pm 5 \text{ kb}$$

$$\left(\frac{\partial \mu_V}{\partial T}\right)_p = \frac{1}{5}\left(\frac{\partial C_{11}^S}{\partial T} - \frac{\partial C_{12}^S}{\partial T} + 3\frac{\partial C_{44}^S}{\partial T}\right)_p = -0.091 \pm 0.008 \text{ kb-K}^{-1}$$

$$\left(\frac{\partial \mu_R}{\partial T}\right)_p = \frac{4}{5}\left(\frac{\mu_R}{C_{11} - C_{12}}\right)^2 \left(\frac{\partial C_{11}^S}{\partial T} - \frac{\partial C_{12}^S}{\partial T}\right)_p + \frac{3}{5}\left(\frac{\mu_R}{C_{44}}\right)_p^2 \left(\frac{\partial C_{44}^S}{\partial T}\right)_p$$

$$= -0.097 \pm 0.013 \text{ kb/K}$$

$$\left(\frac{\partial \mu_{VRH}}{\partial T}\right)_p = \frac{1}{2}\left(\frac{\partial \mu_V}{\partial T}\right)_p + \frac{1}{2}\left(\frac{\partial \mu_R}{\partial T}\right)_p = -0.094 \pm 0.008 \text{ kb/K} \qquad \text{(I.6-9)}$$

The shear modulus obeys an equation similar to equation (I.6-6) only if the Poisson's ratio is independent of temperature (Anderson 1966). These various temperature derivatives given above can then be applied to density and velocity calculations inside Earth's mantle using various averaging schemes and extrapolation based on temperature

dependent equations of state. The significance of various averaging schemes are discussed, for example, in Kumazawa (1969) and in Thomsen (1972a,b). One example of discussing the composition of Earth's upper mantle in terms of temperature and pressure dependence of elasticity is given by Graham (1970).

The elastic constants of stoichiometric single crystal spinel have been measured by Chang and Barsch (1973), O'Connel and Graham (1971) and Lewis (1966). The elastic constants of non-stoichiometric spinel have been measured by Schreiber ($MgO.2.61Al_2O_3$, Anderson et al 1968) and by Verma ($MgO.3.5Al_2O_3$, 1960). Chang and Barsch (1973), O'Connel and Graham (1971), and Schreiber (Anderson et al 1968) also measured their pressure and temperature dependence. These results, together with their methods of measurement, are listed in Table I.6-1. The three most recent measurements especially merit a comparison, since all of them are obtained from single crystal samples grown by Union Carbide, Crystal Products Division, and two of them (the present work and that of O'Connel and Graham 1971) are obtained from the same sample. It is seen from Table I.6-1 that the absolute velocity measurements agree within experimental error but the temperature dependence of velocities generally disagree among the three measurements. It should be pointed out, however, that the error bounds of the present work in Table I.6-1 are assigned from the consistency check as discussed in Section 5. The range of temperature derivatives of velocity allowed by the uncertainty of individual measurements as shown in Figures I.5-10 through I.5-13 are: $(\frac{\partial v_1}{\partial T})_p = (\frac{-2.18}{-3.82}) \times 10^{-4}$ km/sec-K , $(\frac{\partial v_2}{\partial T})_p =$

$\binom{-0.82}{-1.69} \times 10^{-4}$km/sec-K, $(\frac{\partial v_3}{\partial T})_p = \binom{-2.49}{-4.12} \times 10^{-4}$ km/sec-K, and $(\frac{\partial v_4}{\partial T})_p = \binom{-2.05}{-2.41} \times 10^{-4}$km/sec-K. Comparing the values of present work and Chang and Barsch (1973), $(\frac{\partial v_1}{\partial T})_p$ agree within experimental error as listed in Table I.6-1. $(\frac{\partial v_2}{\partial T})_p$, $(\frac{\partial v_3}{\partial T})_p$, and $(\frac{\partial v_4}{\partial T})_p$ disagree in Table I.6-1, but the values given by Chang and Barsch lie within the range allowed by individual uncertainties as listed above. Therefore, the results of the present work are consistent with the measurements obtained by Chang and Barsch (1973). Comparing the values of the present work and those obtained by O'Connel and Graham (1971), $(\frac{\partial v_3}{\partial T})_p$ agree within experimental error as listed in Table I.6-1. Values of $(\frac{\partial v_1}{\partial T})_p$, $(\frac{\partial v_2}{\partial T})_p$, and $(\frac{\partial v_4}{\partial T})_p$ calculated from O'Connel and Graham's data lie even outside the range of values allowed by uncertainty in individual measurements. The conclusion is that the experimental values as obtained from the present method disagree with those obtained from ultrasonic interferometry by O'Connel and Graham. Discussions of possible systematic error in the ultrasonic methods are presented in Section 8.

TABLE I-6-1

Ultrasonic Sound Velocities (in km/sec) at 25°C and Their First Temperature Derivatives (in 10^{-4} km/sec-K) of Single Crystal Spinel

	$v_1 = \sqrt{\frac{C_{11}^s}{\rho}}$	$v_2 = \sqrt{\frac{C_{11}^s}{\rho}}$	$v_3 = \sqrt{\frac{C_{11}^s+C_{12}^s+2C_{44}^s}{2\rho}}$	$v_4 = \sqrt{\frac{C_{11}^s-C_{12}^s}{2\rho}}$	$\sqrt{\frac{K^s+\frac{4}{3}\mu_{VRH}}{\rho}}$	$\sqrt{\frac{\mu_{VRH}}{\rho}}$	Specimen, Author & Technique	Temperature Range
M	8.869 ±0.013	6.5666 ±0.0055	10.199 ±0.011	4.2101 ±0.0043	9.760 ±0.013	5.494 ±0.013	$MgO.Al_2O_3$ Present	293K-423K
$\left(\frac{\partial M}{\partial T}\right)_p$	-3.14 ±0.13	-1.47 ±0.10	-3.20 ±0.15	-2.07 ±0.06	-3.77 ±0.43	-1.82 ±0.20		
M	8.8850 ±0.0088	6.5747 ±0.004	10.2149 ±0.0057	4.2220 ±0.012	-------	------	$MgO.Al_2O_3$ Chang and Barsch(1973) Pulse Superposition	308K-328K
$\left(\frac{\partial M}{\partial T}\right)_p$	-3.20 ±0.03	-1.18 ±0.04	-2.62 ±0.03	-2.25 ±0.08	-------	------		
M	8.8790 ±0.0016	6.5645 ±0.0021	10.2070 ±0.0017	4.2126 ±0.0024	-------	------	$MgO.Al_2O_3$ O'Connel and Graham(1971) Ultrasonic Interferometry	300K-400K Two end points only
$\left(\frac{\partial M}{\partial T}\right)_p$	-3.956 ±0.032	-2.213 ±0.021	-3.62 ±0.41	-0.743 ±0.010	-------	------		
M	------	------	-------	------	9.914	5.645	$MgO.2.61Al_2O_3$ Schreiber (Anderson et al. 1968) Pulse Superposition	-----
$\left(\frac{\partial M}{\partial T}\right)_p$	------	------	-------	------	-3.1	-2.2		
M	8.83 ±0.09	6.54 ±0.07	10.15 ±0.07	4.19 ±0.14	-------	------	$MgO.Al_2O_3$ Lewis(1966) Pulse Echo	-----
M	9.10	6.61	10.30	------	-------	------	$MgO.3.5Al_2O_3$ Verma(1960) Phase Comparison	-----

TABLE I-6-1 (continued)

The values of O'Connel and Graham are calculated from C_{11}^S =2821±1 kb, C_{12}^S=1551±1 kb, C_{44}^S=1542±1 kb; $(\partial C_{11}^S/\partial T)_p$=-0.31±0.002 kb/K, $(\partial C_{44}^S/\partial T)_p$ =-0.136±0.001 kb/K, $[\partial(C_{11}^S+C_{12}^S+2C_{44}^S)/2\partial T]_p$=-0.342±0.03 kb/K ,and $[\partial(C_{11}^S-C_{12}^S)/2\partial T]_p$=-0.0544±0.0003 kb/K, ρ=3.5783 gm/cm^3, and linear thermal expansion coefficient α=6.93x10^{-6}/K (Rigby et al. 1946)

7. Attempt of Using the Same Technique for Pressure Dependence Measurement of Single Crystal Spinel Elastic Constants

Before the temperature dependence measurement of spinel elastic constants, an attempt was made to measure their pressure dependence.

The pressure is generated by a revised version of a 10 kb hand-pump designed by Daniels (1966). The high pressure optical cell employed in the experiment is designed by Stromberg and Schock (1970). The pressure medium is an optical grade vacuum pump fluid, Octoil-S, (Bendix Corporation, Rochester, New York) and the pressure is measured by a Heise gauge (model C, 0-7.5 kb pressure range, Heise-Bourdon Tube Co., Newtown, Conn.). The pressure circuit is shown schematically in Figure I.7-1.

The optical cell is a thick-walled cylinder with two plugs sealing the ends. One sapphire window, in the shape of a truncated cone, is seated against a matching cone in each plug with a pyrophyllite layer in between to seal the pressure fluid and to evenly distribute the stress. The spinel crystal is spring loaded, but separated by a Webber gauge block spacer, onto the end face of one sapphire cone. Details of the plug and sapphire cone are illustrated in Figures I.7-2 and I.7-3 respectively. Figure I.7-4 illustrates the high pressure cell and the relationship between the sample and the two windows. A $LiNbO_3$ 36^{o}rotated Y-cut transducer (1.1 cm x 1.1 cm, 28.5 MHz center frequency) is bonded to the sample using Araldite epoxy (Ciba-Geigy Ltd., Plastic Division, Duxford, Cambridge, England). Leads

are bonded to the transducer electrodes (in Tab configuration) with Tra-duct 2924 conductive epoxy (Tra-Con Inc., Medford, Mass.) and are soldered to the electrical feedthroughs of the high pressure cell plug. The electronics are identical to those used in the temperature dependence measurement.

After being diffracted by the ultrasonic beam inside the crystal, the laser beams travel through the pressure medium and sapphire window before reaching the recording photographic plate. Since the diffraction angle of laser beam carries the information of sound wavelength inside the crystal, any effect changing the diffraction angle of laser beam in the pressure medium and the sapphire window must be corrected.

The window axis is aligned to coincide with the crystal C-axis within half a degree. Under pressure loading, the window deforms in the following manner: the two faces become curved. When the pressure is small compared to the elastic moduli, the curved surface can be approximated by spherical surfaces. Since the maximum pressure in the present experiment is 5 kb , this condition is being satisfied. Also, the surfaces are symmetric about the window axis.

The effect of internal elastic strain on the optical indicatrix is to turn it from uniaxial to biaxial with its z axis generally different from the window axis. We use cylindrical polar coordinate system and take the z-axis along the window axis. For a ray entering the window at distance r_o from the window axis whose displacement vector makes an angle ρ_o with the z-axis and an angle ϕ_o with the

x-axis of the indicatrix at the point of entrance, the index of refraction seen by this ray throughout the window can be written as

$$n(\rho_o,\phi_o,r_o;r,z) = n_o(\rho_o') + n_1(\rho_o,\phi_o,r_o;z) + \frac{1}{2}\left.\frac{\partial^2 n}{\partial r^2}\right|_{r=0,z;\rho_o,\phi_o,r_o} r^2 \qquad \text{(I.7-1)}$$

where ρ_o' is the angle between the polarization vector and the optical axis of the uniaxial indicatrix before elastic deformation. Equation (I.7-1) is the first three terms of expansion in r in axially symmetric medium of the expression

$$n = \left(\frac{\sin^2\rho\,\cos^2\phi}{\alpha^2} + \frac{\sin^2\rho\,\sin^2\phi}{\beta^2} + \frac{\cos^2\rho}{\gamma^2}\right)^{-1/2} \qquad \text{(I.7-2)}$$

where α,β,γ are the three principal indices of refraction. From equation (I.2-2), $\Delta\left(\frac{1}{n^2}\right)_{ij} = \pi_{ijk\ell}\,\sigma_{k\ell}$. Also

$$\pi_{ijk\ell} = p_{ijrs}\,S_{rsk\ell} \qquad \text{(I.7-3)}$$

where $(S_{rsk\ell})$ is the stiffness tensor.

For α - Al_2O_3, Nye (1957), for example, gives

$$(p_{ijrs}) = \begin{pmatrix} p_{11} & p_{12} & p_{13} & p_{14} & & \\ p_{12} & p_{11} & p_{13} & -p_{14} & & \\ p_{31} & p_{31} & p_{33} & 0 & & \\ p_{41} & -p_{41} & 0 & p_{44} & & \\ & & & & p_{44} & 2p_{41} \\ & & & & p_{14} & (p_{11}-p_{12})/2 \end{pmatrix} \quad \text{(I.7-4)}$$

Dixon (1967b) measured the photoelastic tensor $(p_{ijk\ell})$ for α - Al_2O_3 with the results $p_{11} = 0.20$, $p_{12} = 0.08$, $p_{44} = 0.085$, $p_{31} \cong p_{13} \cong 0$, $p_{33} = 0.252$, $p_{14} \cong 0$, $p_{41} \cong 0$. Take the stiffness of α - Al_2O_3 measured by Wachtman et al (1960) with components s_{11}=2.35, s_{33}=2.17 $s_{44} = 6.94$, $s_{12} = -0.72$, $s_{13} = -0.36$, $s_{14} = 0.49$ (unit $10^{-13}cm^2/dyne$), $\pi_{44} = p_{44}s_{44} = 0.59 \times 10^{-13}cm^2/dyne$, for example. Assume a maximum shear stress of 10 kb inside the window (when loaded by a hydrostatic pressure of 5 kb on the window inside face) $\Delta(\frac{1}{n^2})_{44} = \pi_{44}\sigma_4 = 0.59 \times 10^{-3}$. The smallness of this magnitude justifies the expansion (I.7-1).

Fixing attention on a ray with a particular polarization, therefore treating ρ_o, ϕ_o, r_o as parameters, equation (I.7-1) is now written as

$$n = n_o + n_1(z) + \frac{1}{2} n_2(z)\, r^2 \qquad \text{(I.7-5)}$$

The ray equation, given by Born and Wolf (1970a), for example, is

$$\frac{d}{ds}\left(n \frac{d\underset{\sim}{R}}{ds}\right) = \nabla n \qquad \text{(I.7-6)}$$

where $\underset{\sim}{R}$ is the position vector and s the ray parameter. The origin

of the cylindrical polar coordinate is taken at the intersection of the window axis with the window inside face. Use paraxial approximation

$$\frac{d}{ds}\left(n\frac{d\underset{\sim}{R}}{ds}\right) = \frac{d}{dz}\left(n\frac{dr}{dz}\right)\hat{\underset{\sim}{e}}_r + \frac{d}{dz}\left(n\frac{dz}{dz}\right)\hat{\underset{\sim}{e}}_z \qquad \text{(I.7-7)}$$

where $\hat{\underset{\sim}{e}}_r$ and $\hat{\underset{\sim}{e}}_z$ are unit vectors in the r and z directions, respectively. Take inner product with $\hat{\underset{\sim}{e}}_r$ on both sides of the ray equation, and the result is

$$\frac{dn}{dz}\frac{dr}{dz} + n\frac{d^2r}{dz^2} = \frac{\partial n}{\partial r}$$

or

$$\left[n_o + n_1(z) + \frac{1}{2}n_2(z)r^2\right]\frac{d^2r}{dz^2} + \left\{\frac{dn_1}{dz} + \frac{d}{dz}\left[\frac{1}{2}n_2(z)r^2\right]\right\}\frac{dr}{dz} = n_2(z)r \qquad \text{(I.1-8)}$$

However, $n_o >> n_1(z) + n_2(z)r^2/2$ by two orders of magnitude, as shown in the last paragraph. Also, compared with dn_1/dz, the rate of change of index of refraction in the z direction, the term $\frac{d}{dz}\left[\frac{1}{2}n_2(z)r^2\right] \equiv \frac{d}{dz}\left(\frac{1}{2}\frac{\partial^2 n}{\partial r^2}\Big|_{r=0,z} r^2\right)$, which is the change in the z direction of the rate of change of index of refraction in the r direction, is of second order. (A rigorous justification of this is difficult. A possible way to do this is to calculate the stress in the high pressure cell, window plug, and window by the finite element method and use the photoelastic tensor to calculate the indicatrix throughout the window.) The ray equation then becomes

$$\frac{d^2r}{dz^2} + \frac{d}{dz}\left(\frac{n_1}{n_o}\right)\frac{dr}{dz} - \left(\frac{n_2}{n_o}\right) r = 0 \qquad \text{(I.7-9)}$$

Let $r(z) = v(z)\, p(z)$ where

$$p(z) = e^{-n_1/2n_o}$$

$$p'(z) = -\left(\frac{n_1'}{2n_o}\right) e^{-n_1/2n_o}$$

$$p''(z) = \left[-\frac{n_1''}{2n_o} + \left(\frac{n_1'}{2n_o}\right)^2\right] e^{-n_1/2n_o}$$

where prime denotes differentiation with respect to z. Substituting $r(z) = v(z)\, p(z)$ into equation (I.7-9),

$$\frac{d^2v}{dz^2} + \left[\left(\frac{n_1'}{2n_o}\right)^2 - \frac{n_1''}{2n_o} + \left(-\frac{n_1'}{2n_o}\right)\frac{n_1'}{n_o} - \frac{n_2}{n_o}\right] v = 0$$

or

$$v'' - \left[\frac{1}{2}\left(\frac{n_1'}{n_o}\right)^2 + \frac{n_2}{n_o} + \frac{n_1''}{2n_o}\right] v = 0 \qquad \text{(I.7-10)}$$

Let

$$h(z) \equiv \frac{1}{2}\left(\frac{n_1'}{n_o}\right)^2 + \frac{n_2}{n_o} + \frac{n_1''}{2n_o} \qquad \text{(I.7-11)}$$

the WKBJ solution of the equation (Mathews and Walker (1965b)) is

$$v(z) = \frac{a}{|h(z)|^{1/4}} e^{\int_o^z \sqrt{h(z)}\, dz} + \frac{b}{|h(z)|^{1/4}} e^{-\int_o^z \sqrt{h(z)}\, dz}$$

where a, b are constants of integration.

Therefore,

$$r(z) = v(z)\, p(z) = \frac{a}{|h(z)|^{1/4}} e^{-\frac{n_1}{2n_o} + \int_o^z \sqrt{h(z)}\, dz} + \frac{b}{|h(z)|^{1/4}} e^{-\frac{n_1}{2n_o} - \int_o^z \sqrt{h(z)}\, dz} \qquad \text{(I.7-13)}$$

The condition of validity for WKBJ approximation is

$$\left| \frac{h'(z)}{\sqrt{h(z)}} \right| << |h(z)| \qquad \text{(I.7-14)}$$

as given by Mathews and Walker (1965b). The verification of the condition of validity also awaits a numerical calculation of the indicatrices inside the window. Assuming equation (I.7-14)

$$r' = \frac{a}{|h(z)|^{1/4}} \left(-\frac{n_1'}{2n_o} + \sqrt{h(z)}\right) e^{-\frac{n_1}{2n_o} + \int_o^z \sqrt{h(z)}\, dz} + \frac{b}{|h(z)|^{1/4}} \left(-\frac{n_1'}{2n_o} - \sqrt{h(z)}\right) e^{-\frac{n_1}{2n_o} - \int_o^z \sqrt{h(z)}\, dz} \qquad \text{(I.7-15)}$$

At $z = 0$

$$r = r_o = \frac{a}{|h(o)|^{1/4}} e^{-\frac{n_1(0)}{2n_o}} + \frac{b}{|h(0)|^{1/4}} e^{-\frac{n_1(0)}{2n_o}}$$

$$r' = r_o' = \frac{a}{|h(0)|^{1/4}} \left(-\frac{n_1'(0)}{2n_o} + \sqrt{h(0)}\right) e^{-\frac{n_1(0)}{2n_o}}$$

$$+ \frac{b}{|h(0)|^{1/4}} \left(- \frac{n_1'(0)}{2n_o} - \sqrt{h(0)}\right) e^{-n_1(0)/2n_o} \qquad \text{(I.7-16)}$$

Let

$$\alpha \equiv \frac{a}{|h(0)|^{1/4}} e^{-n_1(0)/2n_o} \quad , \quad \beta \equiv \frac{b}{|h(0)|^{1/4}} e^{-n_o(0)/2n_o}$$

$$\gamma_1 \equiv \frac{n_1'(0)}{2n_o} - \sqrt{h(0)} \quad , \quad \gamma_2 \equiv - \frac{n_1'(0)}{2n_o} - \sqrt{h(0)} \qquad \text{(I.7-17)}$$

Equation (I.7-16) becomes

$$\gamma_o = \alpha + \beta$$

$$\gamma_o' = -\alpha\gamma_1 + \beta\gamma_2 \qquad \text{(I.7-18)}$$

Solving for α and β

$$\alpha = (\gamma_2 r_o - r_o')/(\gamma_1 + \gamma_2)$$

$$\beta = (r_o' + r_o\gamma_1)/(\gamma_1 + \gamma_2) \qquad \text{(I.7-19)}$$

Finally, the solution to the ray equation (I.7-9) is given by

$$r = \left|\frac{h(0)}{h(z)}\right|^{1/4} \frac{e^{n_1(0)/2n_o}}{\gamma_1 + \gamma_2} \left\{ r_o \left[\gamma_2 e^{\left(- \frac{n_1(z)}{2n_o} + \int_o^z \sqrt{h(z)}\, dz\right)} + \gamma_1 e^{\left(- \frac{n_1(z)}{2n_o} - \int_o^z \sqrt{h(z)}\, dz\right)} \right] \right.$$

$$+ r_o' \left[e^{-\frac{n_1(z)}{2n_o} - \int_o^z \sqrt{h(z)}\, dz} - e^{-\frac{n_1(z)}{2n_o} + \int_o^z \sqrt{h(z)}\, dz} \right] \Bigg\} \quad \text{(I.7-20)}$$

Its derivative is given, from equation (I.7-16), by

$$\gamma' = \left|\frac{h(0)}{h(z)}\right|^{1/4} \frac{e^{n_1(0)/2n_o}}{\gamma_1 + \gamma_2} \Bigg\{ \gamma_1\gamma_2 r_o \left[e^{-\frac{n_1(z)}{2n_o} - \int_o^z \sqrt{h(z)}\, dz} - e^{-\frac{n_1(z)}{2n_o} + \int_o^z \sqrt{h(z)}\, dz} \right]$$

$$+ r_o' \left[\gamma_1 e^{-\frac{n_1(z)}{2n_o} + \int_o^z \sqrt{h(z)}\, dz} + \gamma_2 e^{-\frac{n_1(z)}{2n_o} - \int_o^z \sqrt{h(z)}\, dz} \right] \Bigg\} \quad \text{(I.7-21)}$$

$$|h(z)|^{-1/4} = |h(0)|^{-1/4} - \frac{1}{4}\frac{d}{dz}|h(z)|_{z=0}\, |h(0)|^{-5/4}$$

$$\cong |h(0)|^{-1/4}$$

$$n_1(z) = n(0) + n_1'(0)z \cong n_1(0)$$

and

$$e^{-\frac{n_1(z)}{2n_o} + \frac{n_1(0)}{2n_o}} \left|\frac{h(0)}{h(z)}\right|^{1/4} \cong 1$$

The expressions for r and r' are therefore

$$r = \frac{1}{\gamma_1 + \gamma_2}\left\{ r_o\left[\gamma_2\, e^{\int_o^z \sqrt{h(z)}\,dz} + \gamma_1\, e^{-\int_o^z \sqrt{h(z)}\,dz}\right] + r_o'\left[e^{-\int_o^z \sqrt{h(z)}\,dz} - e^{\int_o^z \sqrt{h(z)}\,dz}\right]\right\}$$

$$r' = \frac{1}{\gamma_1 + \gamma_2}\left\{ r_o\gamma_1\gamma_2\left(e^{-\int_o^z \sqrt{h(z)}\,dz} - e^{\int_o^z \sqrt{h(z)}\,dz}\right) + r_o'\left[\gamma_1 e^{\int_o^z \sqrt{h(z)}\,dz} + \gamma_2\, e^{-\int_o^z \sqrt{h(z)}\,dz}\right]\right\} \qquad \text{(I.7-22)}$$

For this particular ray, the window can be characterized by the matrix equation

$$\begin{pmatrix} r_{out} \\ r'_{out} \end{pmatrix} = \begin{pmatrix} A & B \\ C & D \end{pmatrix} \begin{pmatrix} r_{in} \\ r'_{in} \end{pmatrix} \qquad \text{(I.7-23)}$$

where

$$A \cong \frac{1}{\gamma_1 + \gamma_2}\left(\gamma_1 + \gamma_2 + \gamma_2 \int_0^L \sqrt{h(z)}\,dz - \gamma_1 \int_0^L \sqrt{h(z)}\,dz\right) \cong 1$$

$$B \cong \frac{-2}{\gamma_1 + \gamma_2} \int_0^L \sqrt{h(z)}\,dz$$

$$C \cong -\frac{2\gamma_1\gamma_2}{\gamma_1 + \gamma_2} \int_0^L \sqrt{h(z)}\,dz\,, \quad D \cong 1 + \frac{\gamma_1 - \gamma_2}{\gamma_1 + \gamma_2} \int_0^L h(z)\,dz \qquad \text{(I.7-24)}$$

where L is the distance between the two window faces.

Sidetracking for the moment we consider solution of the ray equation in the medium with index of refraction variation in only one dimension

$$N(z) = N_o + N_1(z) \tag{I.7-25}$$

The ray equation in this case is

$$\frac{d^2r}{dz^2} + \frac{d}{dz}\left(\frac{N_1}{N_o}\right)\frac{dr}{dz} = 0 \tag{I.7-26}$$

The integration factor for this differential equation is $e^{N_1(z)/N_o}$. Multiplying by this factor, the equation can be written as

$$\frac{d}{dz}\left(e^{N_1(z)/N_o}\frac{dr}{dz}\right) = 0 \quad \text{or} \quad \frac{dr}{dz} = C\, e^{-N_1(z)/N_o} \tag{I.7-27}$$

where C is the constant of integration. Integrate once more,

$$r = C\int_0^z e^{-N_1(z)/N_o}\, dz + D \tag{I.7-28}$$

At $z = 0$, $r = r_o$, $r' = r'_o$. These two conditions imply

$$C = r'_o\, e^{N_1(0)/N_o}, \qquad D = r_o$$

Equation (I.7-28) can be written as

$$r = r'_o\, e^{N_1(0)/N_o}\int_0^z e^{-N_1(z)/N_o}\, dz + r_o \tag{I.7-29}$$

The matrix characterization of the medium is by the following equation:

$$\begin{pmatrix} r_{out} \\ r'_{out} \end{pmatrix} = \begin{pmatrix} 1 & e^{N_1(0)/N_o} \int_0^Z e^{-N_1(z)/N_o}\, dz \\ 0 & e^{[N_1(0) - N_1(Z)]/N_o} \end{pmatrix} \begin{pmatrix} r_{in} \\ r'_{in} \end{pmatrix} \qquad \text{(I.7-30)}$$

where Z is total length of the medium. Expand in Taylor's series about $z = 0$

$$e^{N_1(0)/N_o} \int_0^Z e^{-N_1(z)/N_o}\, dz = Z - \frac{N'_1(0)}{2N_o} Z^2$$

$$e^{[N_1(0) - N_1(Z)]/N_o} = 1 - \frac{N'_1(0)}{N_o} Z$$

Equation (I.7-30) becomes

$$\begin{pmatrix} r_{out} \\ r'_{out} \end{pmatrix} = \begin{pmatrix} 1 & Z - \frac{N'_1(0)}{2N_o} Z^2 \\ 0 & 1 - \frac{N'_1(0)}{N_o} Z \end{pmatrix} \begin{pmatrix} r_{in} \\ r'_{in} \end{pmatrix} \qquad \text{(I.7-31)}$$

Recall that the matrix characterizing a thin lens of focal length f is (for example, Yariv 1971a):

$$\begin{pmatrix} 1 & 0 \\ -\frac{1}{f} & 1 \end{pmatrix}$$

Equating

$$\begin{pmatrix} 1 & 0 \\ -\frac{1}{f} & 1 \end{pmatrix} \begin{pmatrix} 1 & Z - \frac{N_1'(0)}{2N_o} Z^2 \\ 0 & 1 - \frac{N_1'(0)}{N_o} Z \end{pmatrix} = \begin{pmatrix} A & B \\ C & D \end{pmatrix} \qquad \text{(I.7-32)}$$

gives

$$Z - \frac{N_1'(0)}{2N_o} Z^2 = - \frac{2}{\gamma_1 + \gamma_2} \int_0^L \sqrt{h(z)}\, dz$$

$$1 - \frac{N_1'(0)}{N_o} Z = 1 + \frac{\gamma_1 - \gamma_2}{\gamma_1 + \gamma_2} \int_0^L \sqrt{h(z)}\, dz \qquad \text{(I.7-33)}$$

$$f = \left(\frac{2\gamma_1\gamma_2}{\gamma_1 + \gamma_2} \int_0^L \sqrt{h(z)}\, dz\right)^{-1}$$

From these equations Z, $\frac{N_1'(0)}{N_o}$, and f can be solved in terms of γ_1, γ_2, and $h(z)$. Equations (I.7-32) and (I.7-33) state that the effect of window internal strain on a linearly polarized ray, subject to the conditions

$$n_o >> n_1(z) + n_2(z)r^2/2$$

$$\frac{dn_1}{dz} >> \frac{d}{dz}\left[\frac{1}{2} n_2(z) r^2\right]$$

$$|h'(z) / \sqrt{h(z)}| << |h(z)| \ , \ \left[h(z) \equiv \frac{1}{2}\left(\frac{n_1'}{n_o}\right)^2 + \frac{n_2}{n_o} + \frac{n_1''}{2n_o}\right]$$

is equivalent to a medium under one-dimensional strain followed by a thin lens, whose focal length depends on the parameters ρ_o, ϕ_o, r_o characterizing the ray at its point of entrance. This is illustrated

schematically in Figure I.7-5a. As given by Yariv (1971a), a dielectric interface with radius of curvature R, separating dielectric with index of refraction n_1 on the left and dielectric with index of refraction n_2 on the right, is characterized by the matrix

$$\begin{pmatrix} 1 & 0 \\ \frac{n_2 - n_1}{n_2 R} & \frac{n_1}{n_2} \end{pmatrix} \tag{I.7-34}$$

for rays impinging on the interface from the left. When R becomes very large and approaches infinity, i.e., a plane dielectric interface, the matrix becomes

$$\begin{pmatrix} 1 & 0 \\ 0 & n_1/n_2 \end{pmatrix}$$

Since

$$\begin{pmatrix} 1 & 0 \\ 0 & \frac{n_1}{n_2} \end{pmatrix} \begin{pmatrix} 1 & 0 \\ \frac{n_2 - n_1}{n_1 R} & 1 \end{pmatrix} = \begin{pmatrix} 1 & 0 \\ \frac{n_2 - n_1}{n_2 R} & \frac{n_1}{n_2} \end{pmatrix}$$

$$= \begin{pmatrix} 1 & 0 \\ \frac{n_2 - n_1}{n_2 R} & 1 \end{pmatrix} \begin{pmatrix} 1 & 0 \\ 0 & \frac{n_1}{n_2} \end{pmatrix} \tag{I.7-35}$$

a dielectric interface with radius of curvature R is equivalent to a thin lens juxtapositioned with a straight dielectric interface. The equivalent focal length of the thin lens depends on the two indices of

refraction, radius of curvature of the interface, and in which dielectric the thin lens is located. Equation (I.7-35) is illustrated schematically in Figure I.7-5b.

In summary, the sapphire window under pressure loading by the pressure fluid from inside is optically equivalent to one thin lens in the pressure fluid followed by a medium with plane parallel boundaries under one-dimensional strain, and this followed by two thin lenses in the air, the first due to the internal strain in the window and the second representing the effect of window outside curvature. Schematically, this is shown in Figure I.7-5c. Since the change of index of refraction inside the window under strain is small by two orders of magnitude compared to the index of refraction, the indicatrix used to calculate the equivalent focal length of the window curvature can be approximated by the uniaxial indicatrix in the absence of stress. For the uniaxial indicatrix

$$\frac{1}{n^2} = \frac{\sin^2\theta}{\omega^2} + \frac{\cos^2\theta}{\varepsilon^2} \qquad \text{(I.7-36)}$$

where θ is the angle between optic axis and displacement vector, or

$$n = \omega\left[1 + \left(\frac{\omega^2 - \varepsilon^2}{\varepsilon^2}\right)\cos^2\theta\right]^{-1/2} \qquad \text{(I.7-37)}$$

Write $\theta = \frac{\pi}{2} + \Delta\theta$, and $\Delta\theta \sim 10^{-2}$ in the experiment

$$n = \omega\left[1 + \frac{\varepsilon^2 - \omega^2}{2\varepsilon^2}(\Delta\theta)^2\right] \qquad \text{(I.7-38)}$$

Sapphire is optically negative with birefringence of 0.008 in the

visible region. At 6328Å, $\omega = 1.766$ (Malitson 1962), therefore,

$$\frac{\varepsilon^2 - \omega^2}{2\varepsilon^2} \cong \frac{\varepsilon - \omega}{\varepsilon} = \frac{-0.008}{1.758} \cong 4.5 \times 10^{-3}$$

Equation (I.7-38) shows that $n = \omega(1 - 4.5 \times 10^{-7})$ and $n = \omega$ is a very good approximation in calculating the equivalent focal length of the window curvature.

The optical path of diffracted laser beams between crystal and photographic plate is shown in Figure I.7-6. The representation of the sapphire window is identical to Figure I.7-5c. In the figure,

$$(\Delta r)_{out} = \ell - D(\tan \theta_1 + \tan|\theta_{-1}|)$$

$$= \ell - D\,\Delta\theta$$

since $\theta_1, \theta_{-1} \sim 2 \times 10^{-3}$ and $\Delta\theta = \theta_1 + |\theta_{-1}|$, or

$$\Delta\theta = \frac{\ell - (\Delta r)_{out}}{D} \qquad \text{(I.7-39)}$$

Also,

$$\Delta\theta_\alpha = \Delta\theta + (\Delta r)_{out} \left(\frac{1}{f_2} + \frac{1}{f_3}\right) \qquad \text{(I.7-40)}$$

Tracing rays through the one-dimensional strain medium using Snell's law

$$n_\ell \Delta\theta_\beta = n_a \Delta\,\theta_\alpha \qquad \text{(I.7-41)}$$

where n_ℓ is index of refraction of pressure liquid,

and n_a is index of refraction of air.

Also,

$$n_\ell \Delta\theta_\gamma = n_\ell \Delta\theta_\beta + n_\ell \frac{(\Delta r)_{in}}{f_1} \tag{I.7-42}$$

and

$$n_\ell \Delta\theta_\gamma = n_{spinel}\, \Delta\theta_{spinel} = n_{spinel} \frac{2\lambda_o}{\Lambda n_{spinel}} = \frac{2\lambda_o}{\Lambda} \tag{I.7-43}$$

where n_{spinel} is index of refraction of spinel

λ_o is light wavelength in vacuum

Λ is the sound wavelength inside crystal

Combining equations (I.7-39), (I.7-40), (I.7-41), (I.7-42), and (I.7-43)

$$2\frac{\lambda_o}{\Lambda} = n_a \Delta\theta + n_a (\Delta r)_{out} \left(\frac{1}{f_2} + \frac{1}{f_3}\right) + n_\ell \frac{(\Delta r)_{in}}{f_1}$$

$$= n_a \frac{\ell}{D} + n_a (\Delta r)_{out} \left(\frac{1}{f_2} + \frac{1}{f_3} - \frac{1}{D}\right) + n_\ell \frac{(\Delta r)_{in}}{f_1} \tag{I.7-44}$$

When quantities on the right hand side of equation (I.7-44) are known, the sound wavelength Λ inside the crystal can be computed. The measurements of these quantities are discussed in the following:

n_a: index of refraction of air, can be found in handbook

D: distance between photographic plate and optical window outside surface, can be measured with an inside micrometer

ℓ: distance between laser beams as recorded on the photographic plate, can be measured by microdensitometer, as in the case of temperature dependence measurement

n_ℓ: index of refraction of the pressure liquid, can be measured with Abbe refractometer. Knowing compressibility of the

liquid, the pressure dependence of n_ℓ can be taken into account by Lorenz-Lorentz relation.

$$(\Delta r)_{in} = \Delta\theta_\gamma T + \Delta\theta_{spinel} t/2 = 2\lambda_o T/\Lambda n_\ell + \lambda_o t/\Lambda n_{spinel}$$

$$= \frac{2\lambda_o}{v} F\left(\frac{T}{n_\ell} + \frac{t}{2n_{spinel}}\right)$$

where t is the thickness of the crystal, T is the thickness of the spacer block between crystal and window, and v is the velocity of sound in crystal excited by transducer driven at frequency F. Since $\frac{1}{v}\frac{dv}{dp} \cong 5 \times 10^{-4}/\text{kb}$ (Chang and Barsch 1973) and $dn_{spinel}/dp \cong -10^{-4}/\text{kb}$ (K. Vedam, personal communication), room temperature, atmospheric pressure values of v, D, t, and n_{spinel} will yield accurate determination of $(\Delta r)_{in}$.

$(\Delta r)_{out}$: can be determined by an auxiliary experiment as illustrated in Figure I.7-7. The two mirrors are aligned parallel to the optical window and the photographic plate. (This can be accomplished, for example, by a comparison autocollimator). The laser beam is first focused such that the spots have minimum size when separated by ℓ' on the photographic plate. Secondly, the laser beam is focused such that the spots have minimum size when separated by ℓ'' on the photographic plate. From Figure I.7-7 and equation (I.7-39)

$$\Delta\theta = \frac{\ell'' - \ell'}{d} = \frac{\ell - (\Delta r)_{out}}{D} \qquad \text{(I.7-45)}$$

where d is the separation between the two mirrors. $(\Delta r)_{out}$ can be solved from equation (I.7-45). The 50% beam splitter can be mounted on a translation stage and moved in and out of the laser beams during different parts of the experiment.

This leaves us with the task of determining the focal lengths f_1, f_2, and f_3.

f_1, f_2, and f_3: The focal length f_1 can be characterized adequately by the curvature of window inside face, the index of refraction of the pressure fluid, and the index of refraction ω of sapphire when free of external stress, as discussed previously. Similarly, the focal length f_3 can be characterized by the window outside curvature, index of refraction of air, and ω. The focal length f_2, however, depends on the internal elastic strain of the window and on the particular ray which travels through the window. The dependence on the particular ray which travels through the window, however, is very weak (equation (I.7-38)), and can be neglected in the following auxiliary experiment. The experimental setup is essentially a Twyman-Green interferometer with chopped laser beam (laser chopped by a Bulova tuning fork chopper at 800 Hz) for lock-in detection. The details of the setup are shown in Figure I.7-8. For

determination of window outside face curvature, hence f_3, the window outside surface is coated by evaporation with aluminum. A Webber gauge block flat to $1/10\lambda$ is used as the reference mirror. The laser beam, after being chopped, is expanded and collimated by a microscope objective (Wild 20 magnification, N.A. 0.45), a 25 μm pinhole, and a long focal length lens (Wollensak f/4.5, 209 mm focal length). Intensity profiles are measured by a photomultiplier (EMI type no. 9558B) masked by a 25 μm pinhole and scanned by a synchronous motor driven translation stage at 0.025" per second. Three profiles are taken, one when the reference beam is blocked, another when the beam from beam splitter to window is blocked, and a third when the reference beam and the beam reflected from the window are allowed to interfere with each other. Examples of the three profiles are illustrated in Figure I.7-9. The high frequency noise in the reference beam profile comes from fine polishing streaks in the gauge block. While not presenting any intrinsic problem in data interpretation, this can be avoided in future experiments by using glass mirror instead. The intensity profile of the interference pattern is given in terms of the reference and window beam intensity profiles, complex degree of temporal coherence $\mu_T(\tau)$ of the laser, and phase difference between window and reference beams

by, e.g., Collier, Buckhardt and Lin (1971)

$$I = I_r + I_w + 2\sqrt{I_r I_w}\,|\mu_T(\tau)|\cos\beta \qquad \text{(I.7-46)}$$

where $\tau = \Delta\ell/c$, $\Delta\ell$: difference in path lengths of the two interfering beams, c is speed of light, $\beta = \delta + \zeta(\tau)$, δ = phase difference between interfering beams, and $\zeta(\tau)$: phase of the complex quantity $\mu_T'(\tau) = \mu_T(\tau)\exp(-2\pi i\, f_o\tau)$. The quantity f_o will be defined below. The complex degree of temporal coherence is defined by

$$\mu_T(\tau) = \frac{\langle v(t+\tau)\, v^*(t)\rangle}{\langle v(t)\, v^*(t)\rangle} \qquad \text{(I.7-47)}$$

where $v(t)$ is the complex electric field and $\langle v(t+\tau)v^*(t)\rangle \equiv \lim_{T\to\infty} \frac{1}{2T}\int_{-T}^{T} v(t+\tau)v^*(t)dt$

Born and Wolf (1970b) showed that equation (I.7-47) can be transformed into

$$\mu_T(\tau) = \int_{-\infty}^{+\infty} \Phi(f)\exp(2\pi i\, f\tau)df \Big/ \int_{-\infty}^{+\infty} \Phi(f)\, df \qquad \text{(I.7-48)}$$

where $\Phi(f)$ is the power spectrum of the electric field.

For Spectra Physics 135 laser which has only three longitudinal modes at f_o, f_1, and f_2, with $f_2 - f_1 = f_1 - f_o = \frac{c}{2\ell}$ where ℓ is the laser cavity length,

$$\Phi(f) = I_0\delta(f-f_0) + I_1\delta(f-f_1) + I_2\delta(f-f_2) \qquad \text{(I.7-49)}$$

Substituting $\Phi(f)$ into equation (I.7-48)

$$\mu_T(\tau) = \exp(2\pi i\, f_0\tau)[a_0 + a_1\exp(i\pi \frac{\Delta\ell}{\ell}) + a_2\exp(i\pi \frac{2\Delta\ell}{\ell}) \qquad \text{(I.7-50)}$$

a_0, a_1, and a_2, which give the relative excitation of the three longitudinal modes, are at most slowly varying functions of time. The last equation shows that both $|\mu_T(\Delta\ell)|$ and the phase of $\mu_T'(\Delta\ell) = a_0 + a_1\exp(\pi i \frac{\Delta\ell}{\ell}) + a_2\exp(2\pi i \frac{\Delta\ell}{\ell})$ are also at most slowly varying functions of time. Therefore, $\mu_T(\Delta\ell)$ and $\zeta_T(\Delta\ell)$ can be considered as constant during a single pressure measurement. For spherical curvature on the window outside surface

$$\delta = \delta_0 + \delta_1 r + \frac{kr^2}{R}$$

where k is light wave vector in air, R is the radius of curvature of the window outside surface, and r is the distance from the window axis.

The linear term comes from the slight nonparallelism between the two beams. The square term comes from the window curvature (Yariv 1971b). From the three intensity profiles, equation (I.7-46) can be solved for δ as a quadratic function of the distance along

the photomultiplier scanning path. The coefficient of the square term in distance gives the value k/R. From the value R, the equivalent focal length f_3 can be computed according to equation (I.7-35). The determination of f_1 and f_2 are more involved. Interference profiles are taken between a reference beam and the reflected beam from (i) window with outside surface clear and inside surface coated with aluminum by evaporation, and (ii) window with both surfaces clear but with a Webber gauge block in place of the spinel crystal. The gauge block is subjected to hydrostatic pressure and maintains its surface flatness at high pressures. Since

$$\begin{pmatrix} 1 & 0 \\ -\frac{1}{f_2} & 1 \end{pmatrix} \begin{pmatrix} 1 & -Z - \frac{N_1'(0)}{2N_o} Z^2 \\ 0 & 1 - \frac{N_1'(0)}{N_o} Z \end{pmatrix} \begin{pmatrix} 1 & 0 \\ -\frac{1}{f_1} & 1 \end{pmatrix} \begin{pmatrix} r_{in} \\ r_{in}' \end{pmatrix}$$

$$= \begin{pmatrix} r_{in}\left(1 - \frac{Z}{f_1} - \frac{N_1'(0)Z}{2N_o}\frac{Z}{f_1}\right) + r_{in}'\left(Z - \frac{N_1'(0)}{2N_o} Z^2\right) \\ - r_{in}\left(\frac{1}{f_1} + \frac{1}{f_2}\right) + r_{in}' + r_{in}\left(\frac{N_1'(0)Z}{N_o f_1} + \frac{Z}{f_1 f_2} - \frac{N_1'(0)}{2N_o}\frac{Z^2}{f_1 f_2}\right) \\ - r_{in}'\left(\frac{N_1'(0)Z}{N_o} + \frac{Z}{f_2} - \frac{N_1'(0)Z^2}{2N_o f_2}\right) \end{pmatrix} \quad \text{(I.7-51)}$$

For normal incidence, $r_{in}' = 0$ and the right hand side of equation (I.7-51) becomes

$$\begin{pmatrix} r_{in}\left(1 - \frac{Z}{f_1} - \frac{N_1'(0)}{2N_o}\frac{Z^2}{f_1}\right) \\ - r_{in}\left(\frac{1}{f_1}+\frac{1}{f_2}\right) + r_{in}\left(\frac{N_1'(0)}{N_o}\frac{Z}{f_1}+\frac{Z}{f_1 f_2} - \frac{N_1'(0)}{2N_o}\frac{Z^2}{f_1 f_2}\right) \end{pmatrix} \tag{I.7-52}$$

Since $\frac{Z}{f_2}, \frac{Z}{f_1} \sim 10^{-2}$, $\frac{ZN_1'(0)}{N_o} \sim 10^{-3}$, at most, the expression (I.7-52) becomes

$$\begin{pmatrix} r_{in} \\ - r_{in}\left(\frac{1}{f_1} + \frac{1}{f_2}\right) \end{pmatrix} \tag{I.7-53}$$

i.e., the effect of the one-dimensional strain medium in Figure I.7b can be neglected in these two measurements. From the two interference profiles (i) and (ii), which give equations of linear combinations of $\frac{1}{f_1}$ and $\frac{1}{f_2}$, the two equivalent focal lengths f_1 and f_2 can be determined. This, however, is complicated by the reflections at the clear window faces and instead of equation (I.7-46), an equation describing interference of multiple beams must be used to interpret the results. This has not been worked out for the present experiment for the unfortunate fact that the laser beam separation ℓ as recorded on the photographic plates showed large scatter in data under identical pressure conditions.

The data of the laser beam separation ℓ as a function of pressure (read out on a microdensitometer at the University of California Lawrence Livermore Laboratory by Dr. R. N. Schock) are presented in Figure I.7-10 and Table I.7-1. The cause of the wide scatter in data is suspected to be the index of refraction fluctuation in the pressure medium. Indeed, it is observed that if a rf power of $\sim$5 watts is kept on the transducer, the diffraction pattern of laser beams begins to appear distorted to the eye in 10 seconds, and in one minute the pattern is lost to the eye because the laser beam has been diffused to a great extent by the index of refraction fluctuation associated with fluid convection inside the high pressure cell. During the experiment, although the cell is left to reach thermal equilibrium with room temperature for about half an hour after each pressure change and associated adiabatic heating, the conditions that the room temperature is regulated to $\pm 2^{o}$C and that the change of diffraction angle due to pressure dependence of elastic constants is small ($\theta = \frac{\lambda}{\Lambda} = \frac{\lambda f}{v}$, λ: light wavelength, Λ: sound wavelength in crystal, v: velocity of sound, f: sound frequency, $d\theta/dp = -\frac{\lambda}{f^2} f \frac{dv}{dp} \simeq -10^{-6}$ radians/kb, using data from Chang and Barsch (1973) for compressional velocity and its pressure derivative in [100] direction) imply thermal and density (due to impurity in the pressure fluid) fluctuation in the index of refraction of the pressure fluid could easily overwhelm the effect of pressure dependence of elastic constants on the laser diffraction angle.

In view of these difficulties, it seems that it probably would be futile to try the experiment further without significantly improving

the experimental setup. Following are the improvements which should be implemented before the experiment is tried again.

1. Instead of using synthetic single crystal sapphire as optical window, synthetic single crystal spinel, which is optically isotropic when free of external stress, should be used.

2. Instead of the cone configuration of the optical window as used by Stromberg and Schock (1970), which has the advantage of being easy to seal, the old Poulter seal design (for example, as described in Fishman and Drickamer (1956)), which is a direct lap seal of window onto the steel plug, should be used. The reason is that the pyrophyllite cone in the Stromberg-Schock seal might still flow even after several pressure cycles and this would make the effective window focal lengths change as a function of time.

3. The thickness of the spacer block between sample and window should be reduced as much as possible in order to reduce the effect of index of refraction fluctuation in the pressure fluid.

4. The whole pressure cell should be enclosed in a constant temperature bath and the light path between the pressure cell and the photographic plate should be evacuated.

TABLE I-7-1

Separation of First Order Diffracted Laser Beams as Recorded on the Photographic Plate in the Setup Shown in Figure I-7-6 at Different Pressures. Compressional Sound Wave Propagates in the (001) Direction of the Crystal

Photographic Plate Designation	Pressure (kb)	Transducer Driving Frequency (MHz)	Spot Separation (cm)
P-1	0.509	28.88994	1.106
P-2	1.555	28.91343	1.092
P-3	1.555	28.91343	1.065
P-4	2.502	28.93695	1.068
P-5	2.502	28.93695	1.078
P-6	3.502	28.96049	1.064
P-7	3.502	28.96049	1.064
P-8	4.505	28.98403	1.066
P-9	4.505	28.98403	1.096
P-10	5.004	28.99600	1.073
P-11	5.004	28.99600	1.068
P-12	5.003	28.99600	1.122
P-13	5.003	28.99600	1.134
P-14	3.991	28.97245	1.134
P-15	3.991	28.97245	1.134
P-16	3.991	28.97245	1.128
P-17	3.991	28.97245	1.131
P-18	3.010	28.94891	1.082
P-19	3.010	28.94891	1.105
P-20	3.010	28.94891	1.066
P-21	1.996	28.92538	1.066
P-22	1.990	28.92538	1.067
P-23	1.992	28.92538	1.066
P-24	0.998	28.90186	1.061

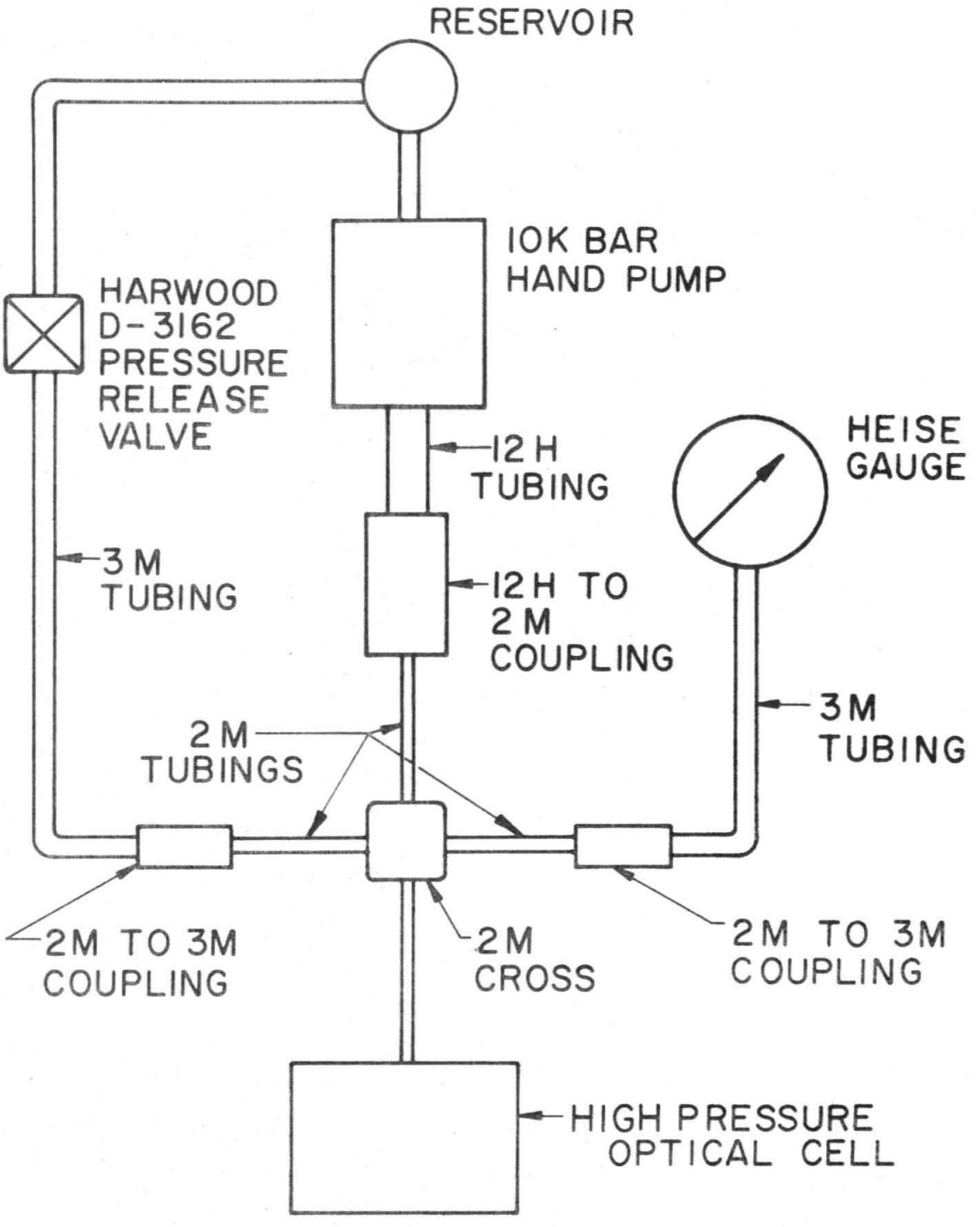

Figure I-7-1. Schematic diagram showing pressure circuit for the pressure dependence measurement of spinel elastic constants.

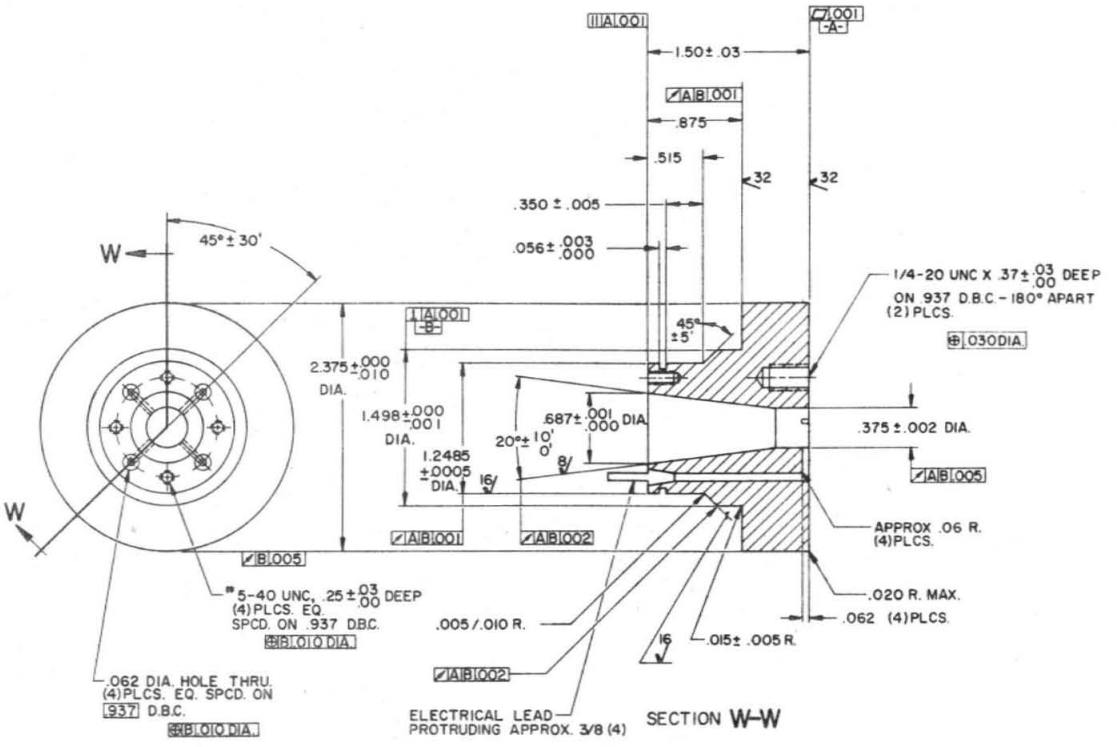

Figure I-7-2. Drawing of high pressure optical cell window plug. Dimensions are in inches.

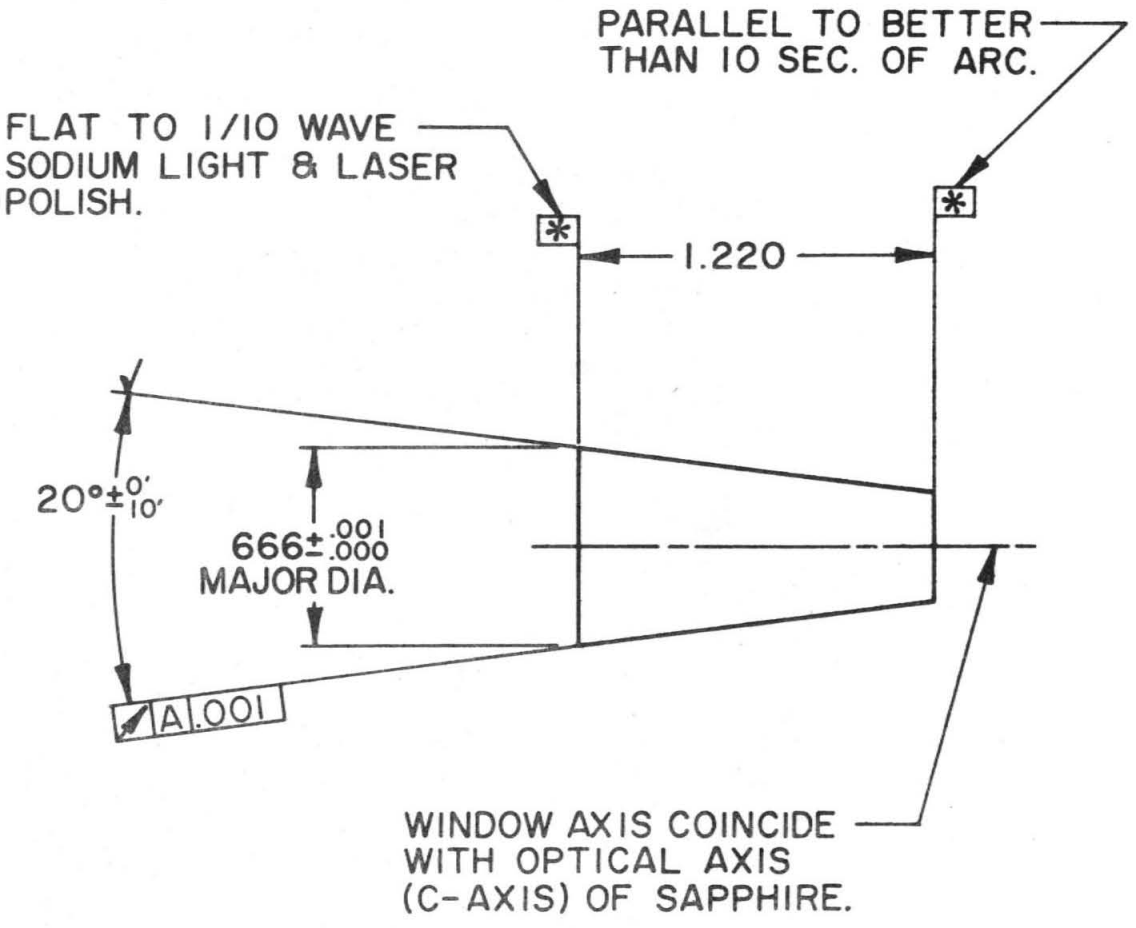

Figure I-7-3. Drawing of the high pressure optical cell sapphire window. Dimensions are in inches.

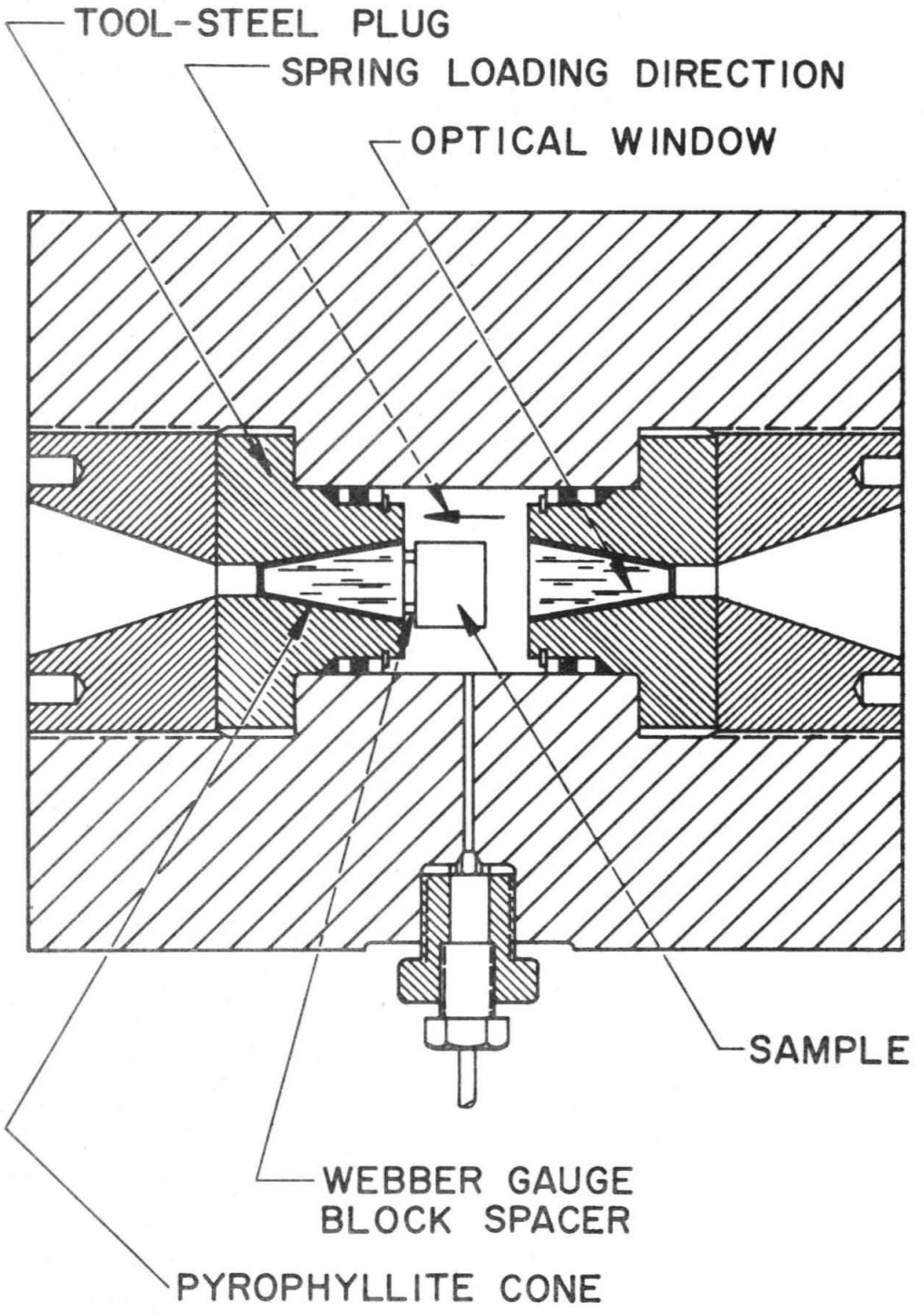

Figure I-7-4. The high pressure optical cell and positioning of sample inside the cell. Drawing of high pressure cell is after Stromberg and Schock (1970).

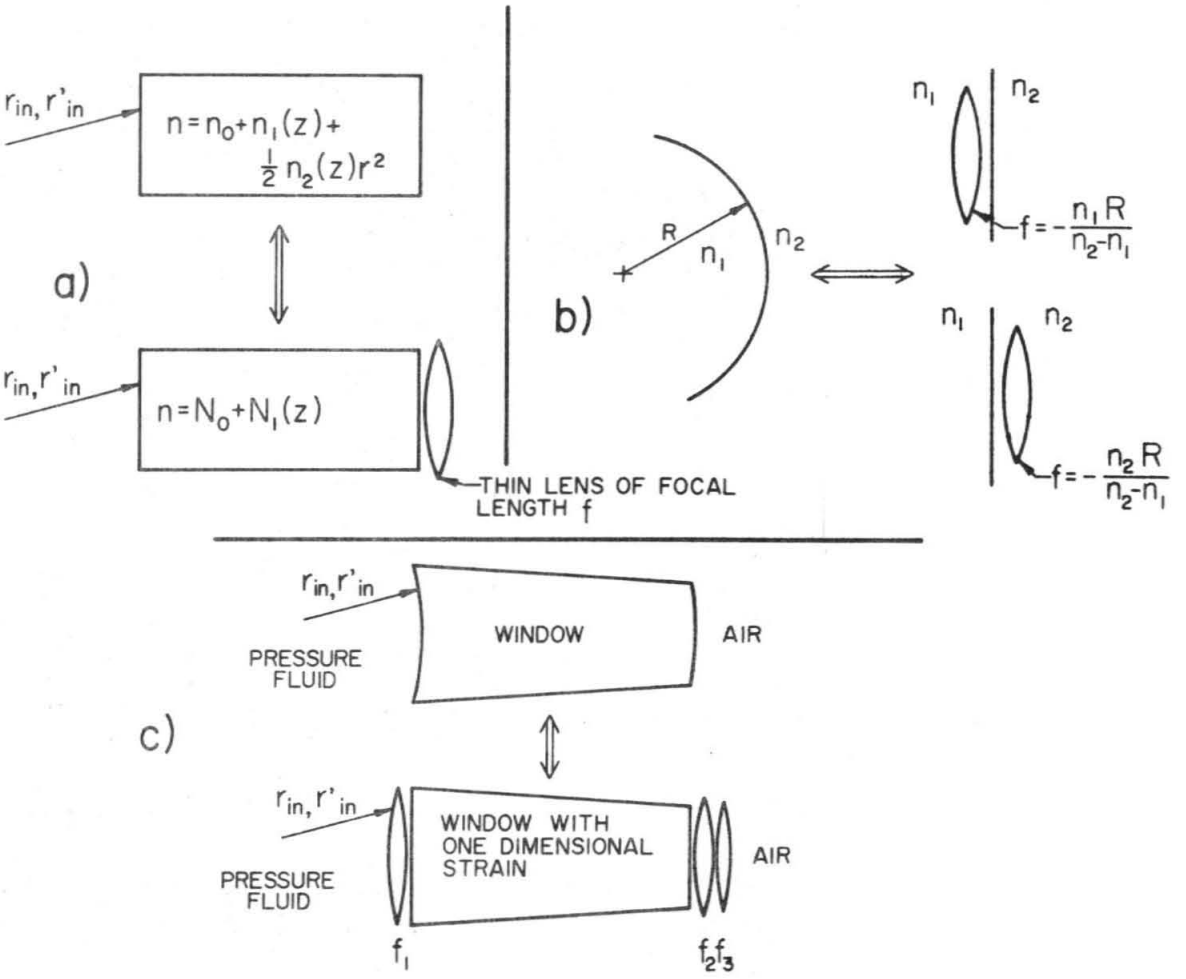

Figure I-7-5. Optical equivalents of (a) window with cylindrically symmetric internal strain, (b) spherical dielectric interface, and (c) window with cylindrical symmetric internal strain and curved endfaces.

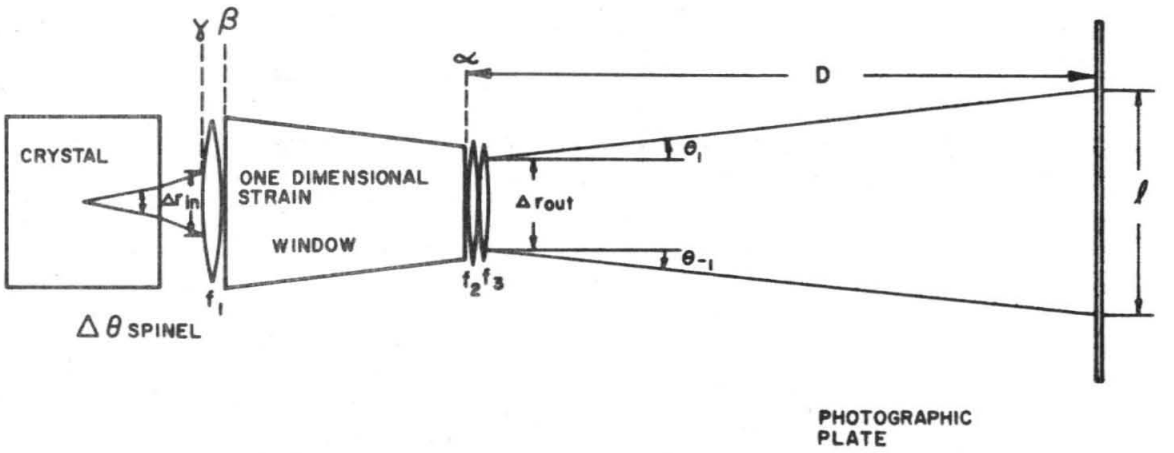

Figure I-7-6. Optical path between sample and photographic plate in the pressure dependence measurement of spinel elastic constants.

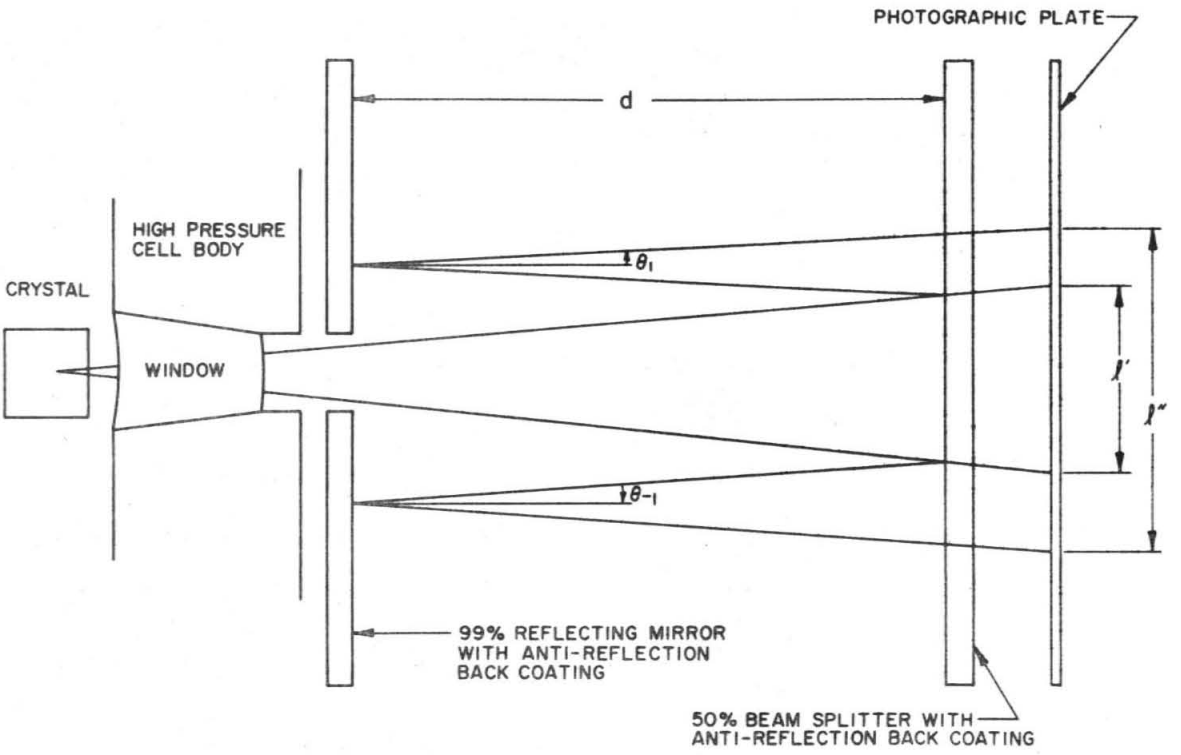

Figure I-7-7. Setup of auxiliary experiment for measuring $(\Delta r)_{out}$.

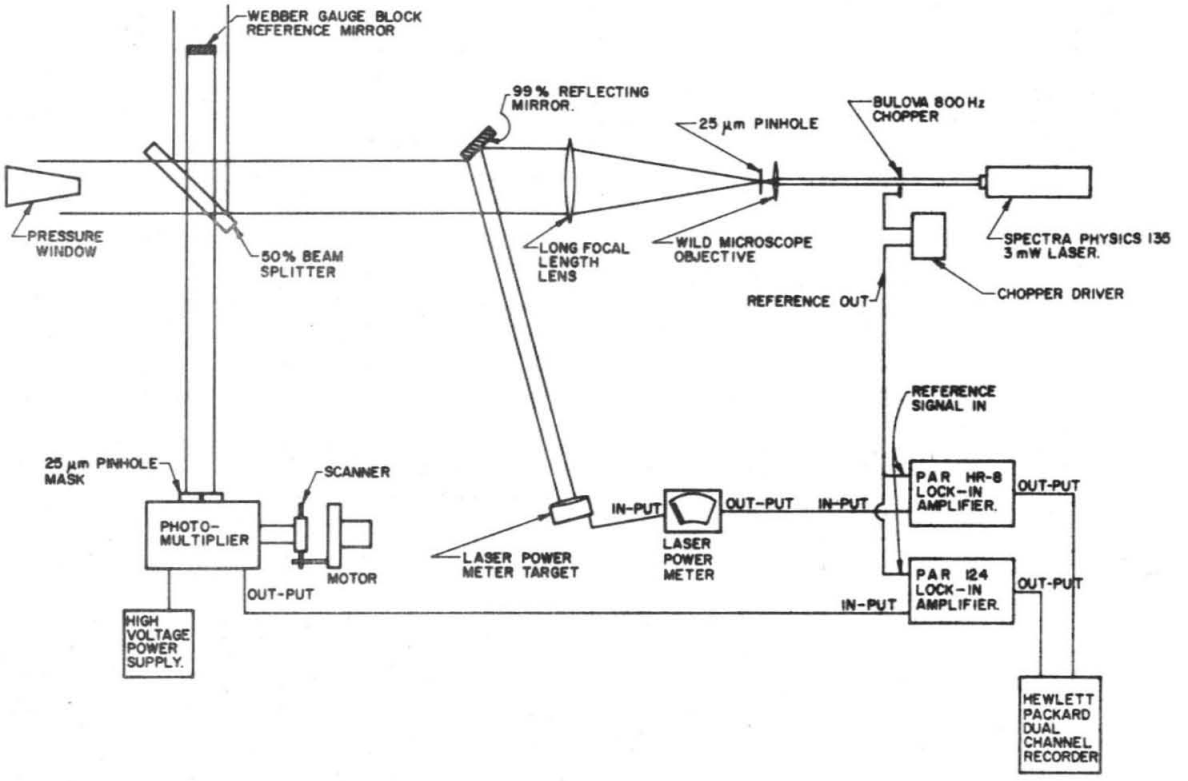

Figure I-7-8. Experiment setup of an optical interferometer for pressure window deformation measurement.

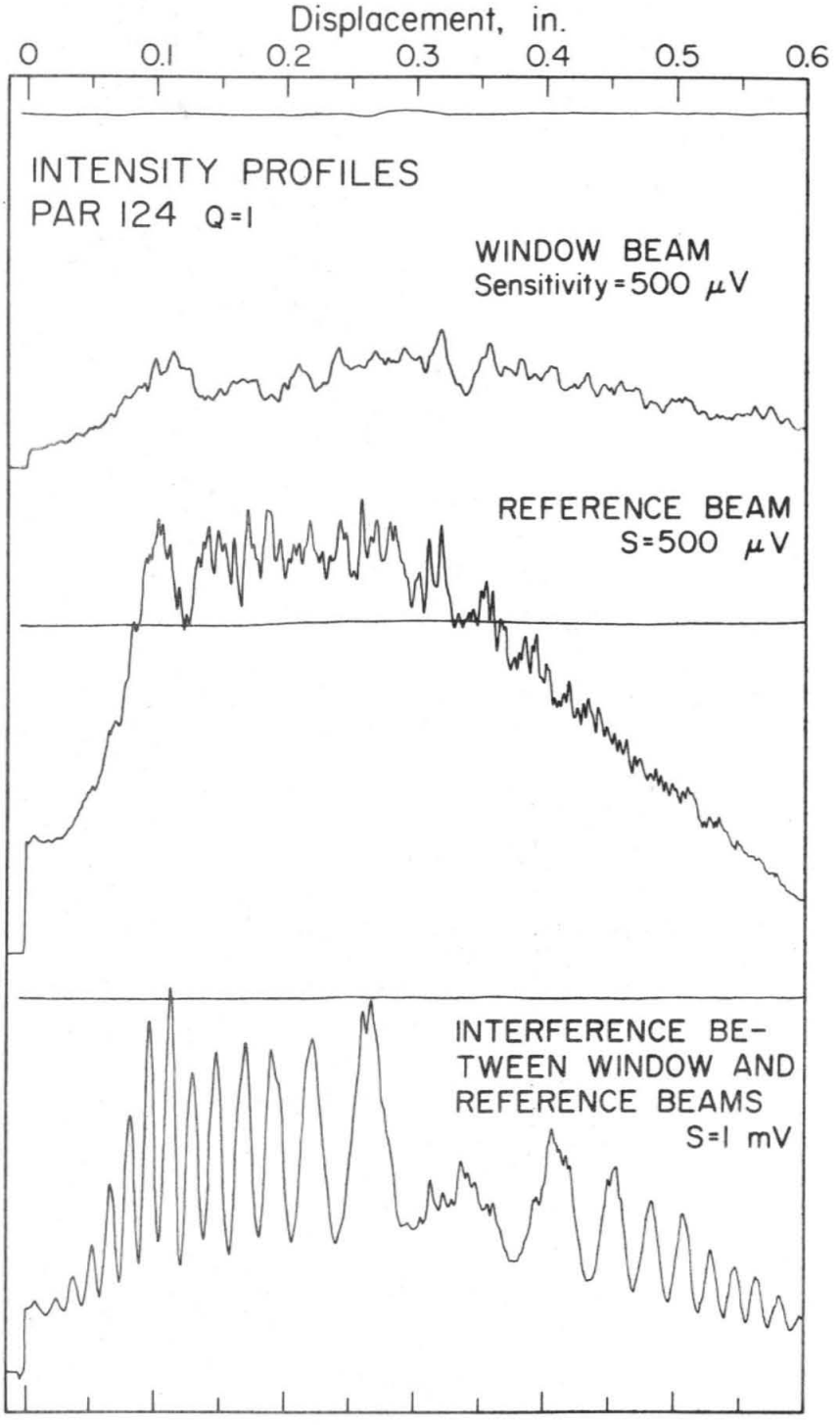

Figure I-7-9. Three intensity profiles for window deformation determination at 5.006kBar. (Window outside face coated with aluminum.)

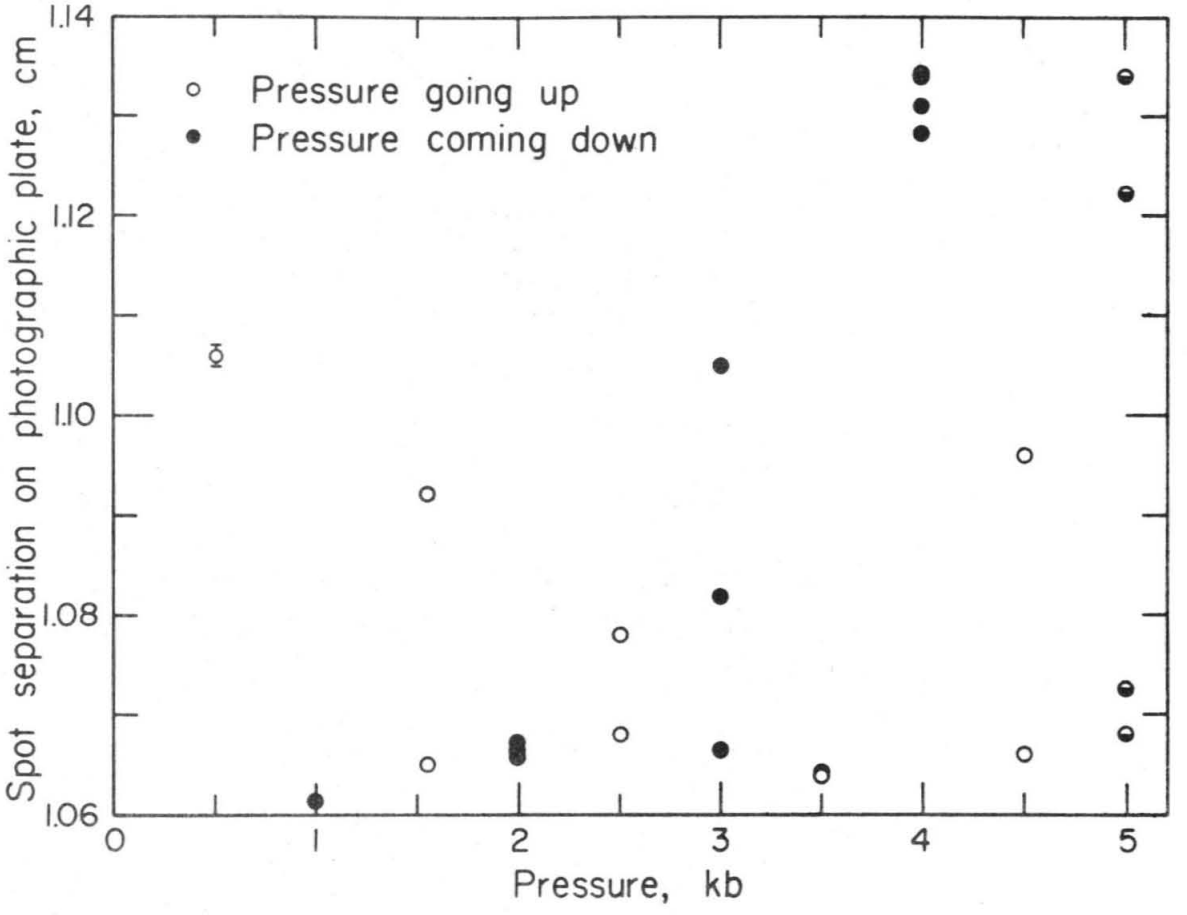

Figure I-7-10. Separation of first order sound-diffracted laser beams as recorded on the photographic plate vs. pressure. A representative error bar is indicated on the left-most data point. The sound wave propagates in the crystal $\langle 001 \rangle$ direction.

8. Evaluation of Light-Sound Scattering as a Method to Measure Elastic Constants

The present experiment is an attempt to use light-sound scattering in the Raman-Nath region to determine pressure and temperature dependence of sound velocities in solids. The temperature dependence of the sound velocities in single crystal spinel was successfully measured. Some of the results are different from those determined from ultrasonic measurements, as discussed in Section 6. The two high precision ultrasonic methods for measuring these quantities are (1) Pulse Superposition (McSkimin 1961, McSkimin and Andreatch 1962), and (2) Ultrasonic Interferometry through a buffer rod (Spetzler 1970). Measurements on the same samples with these two methods yield different results (Spetzler 1969).

In the pulse superposition method, the phase shifts at the sample-transducer interface must be corrected for. This correction involves (McSkimin and Andreatch 1962) the acoustical impedances of bond and transducer, their thicknesses and phase shift constants. Several difficulties, which limit the accuracy of the measurement, are (1) The resonance peak of transducer is not sharp and deteriorates with temperature and pressure, which makes transducer phase shift constant difficult to determine. (2) The bond (most commonly used is Nonag stopcock grease) impedance changes with pressure and temperature and this is usually not allowed for. Also, in the shear wave measurements, the acoustical impedance of the thin film grease bond depends on its viscosity (Thurston 1964) and is generally unaccounted for. (3) Effect

of transducer radiation pattern and side reflections. The buffer rod technique of Spetzler assumes zero phase shift at the lapped sample-buffer rod interface. Side reflections from the buffer rod and sample are not taken into consideration. Also, in picking the maxima and minima interference conditions, the frequency response of the transducer and the effect of electronic bandwidth, which envelope modulate the maxima and minima conditions, are neglected in the analysis. Both methods require exact sample length determination at all temperatures and pressures. The method of light-sound scattering in the Raman-Nath region, however, is free from these corrections. Since the interaction takes place inside the sample and the light samples only that portion of the sound wave which lies in its path, the exact manner in which sound is coupled into the crystal is immaterial. The only error introduced by the boundaries of the sample, as discussed in the Data and Data Reduction section, is the profile distortion of the diffracted light intensities. This distortion can be accounted in detail if instead of standing waves, travelling waves are used as the diffracting grating. In a setup as shown in Figure I.8-1, with the sample shaped at one end in a wedge and the wedge end bounded to an absorber (usually a soft metal, which attenuates effectively ultrasound with frequencies above 20 MHz). The sound wave launched at the transducer is absorbed at the farther end of the crystal. The acoustic wave will not feel the presence of the sides if the transducer is smaller than the sample face on which it is mounted and if the transducer frequency is high enough (Morse 1948). This will truly be a setup to

measure accurately sound propagation velocity in an infinite medium, which has not been done. With boundary effects removed, the accuracy of velocity measurement can be extended to 5×10^{-5}. The temperature dependence of sound velocities in solids can be measured to 670°C with $LiNbO_3$ transducer and a cold-weld gold-indium bond (Sittig and Cook 1968). The successful measurement of pressure dependence of sound wave velocities by Raman-Nath scattering awaits the solution of experimental difficulties as listed in the last section.

Although the present work is the first measurement of temperature dependence of ultrasonic velocities in a solid by light-sound scattering in the Raman-Nath region, the same phenomenon has been used to determine elastic constants of various materials with less experimental accuracy. The early work is reviewed in Bergmann (1954). More recently Barnes and Hiedemann (1956) measured elastic constants of various glasses and Mayer and Hiedemann (1958) determined elastic constants of single crystal sapphire with Raman-Nath diffraction of light by ultrasound.

The same scattering also takes place between light and surface waves, as first reported by Schaefer and Bergmann (1936). This technique can be used to measure elastic constants of opaque materials. Recently Auth and Mayer (1967) determined surface wave velocities for glass and aluminum and Krokstad and Svaasand (1967) measured surface velocity on crystalline quartz sample using laser light diffracted from acoustic surface waves. The former work quotes an experimental accuracy

of 5% and no experimental error is given in the latter. It should be possible to improve the experimental accuracy, therefore, to measure temperature dependence of surface wave sound velocities with the more efficient sound coupling method (White and Voltmer 1965) and a more accurate method of diffraction angle determination such as the one used in the present work.

Light-sound scattering in the Bragg region can also be used to measure sound velocities. Krischner (1968) measured sound velocities in LaF_3 with Bragg scattering to an accuracy of 0.2%. The Bragg scattering requires a different, perhaps more expensive technique from that of the Raman-Nath scattering method. The ultimate accuracy in both experiments are comparable since both involve an accurate angle measurement. However, the Bragg scattering technique may have the advantage of being able to measure temperature dependence of sound velocities in very small samples (2 mm x 2 mm x 2 mm). When applied to pressure dependence measurement, the Bragg scattering technique encounters the same problem of pressure window deformation and pressure fluid index of refraction fluctuation as does the Raman-Nath technique.

If one proceeds in sound frequency to hypersound, the Brillouin scattering of light by thermal phonons can be used to measure sound velocities. Brillouin scattering measurements of sound velocities in solids are summarized by Anderson, Phinney and Sammis (1969). The measurements summarized in this article are generally accurate at best to 0.5%. Pine (1972) improved the Brillouin scattering method to an accuracy of 0.1% by using a single mode laser and a

high resolution tandem spectrometer with two Fabry-Perot interferometers, and measured the temperature dependence of hypersound velocity along the C-axis of CdS from $100^{o}K$ to $400^{o}K$. Discrepancies exist between the temperature dependence of velocities of single crystal CdS as measured by Brillouin scattering and as measured by ultrasonic pulse superposition (Gerlich 1967) even after dispersion is accounted for (Pine 1972). Brillouin scattering offers a method to measure both pressure and temperature dependence of sound wave velocities since the experimentally determined quantities are Brillouin frequency shifts of the single mode laser and are independent of any pressure cell window deformation. The sample can be spring loaded directly to the pressure cell window to eliminate any effect arising from the fluctuation of pressure fluid index of refraction, which causes the fluctuation of collection angle in the Brillouin scattering experiment. A separate experiment to determine temperature and pressure dependence of index of refraction of the solid whose velocities are being measured is necessary to determine the elastic constants from Brillouin scattering results. This is straightforward, however. With pulsed laser, stimulated Brillouin scattering can be used to measured sound velocities in solids. The stimulated Brillouin scattered light being coherent, it should be possible to attain an experimental accuracy several orders of magnitude higher than thermal Brillouin scattering by using heterodyne technique to measure the Brillouin frequency shift. To the author's knowledge, this has not yet been done.

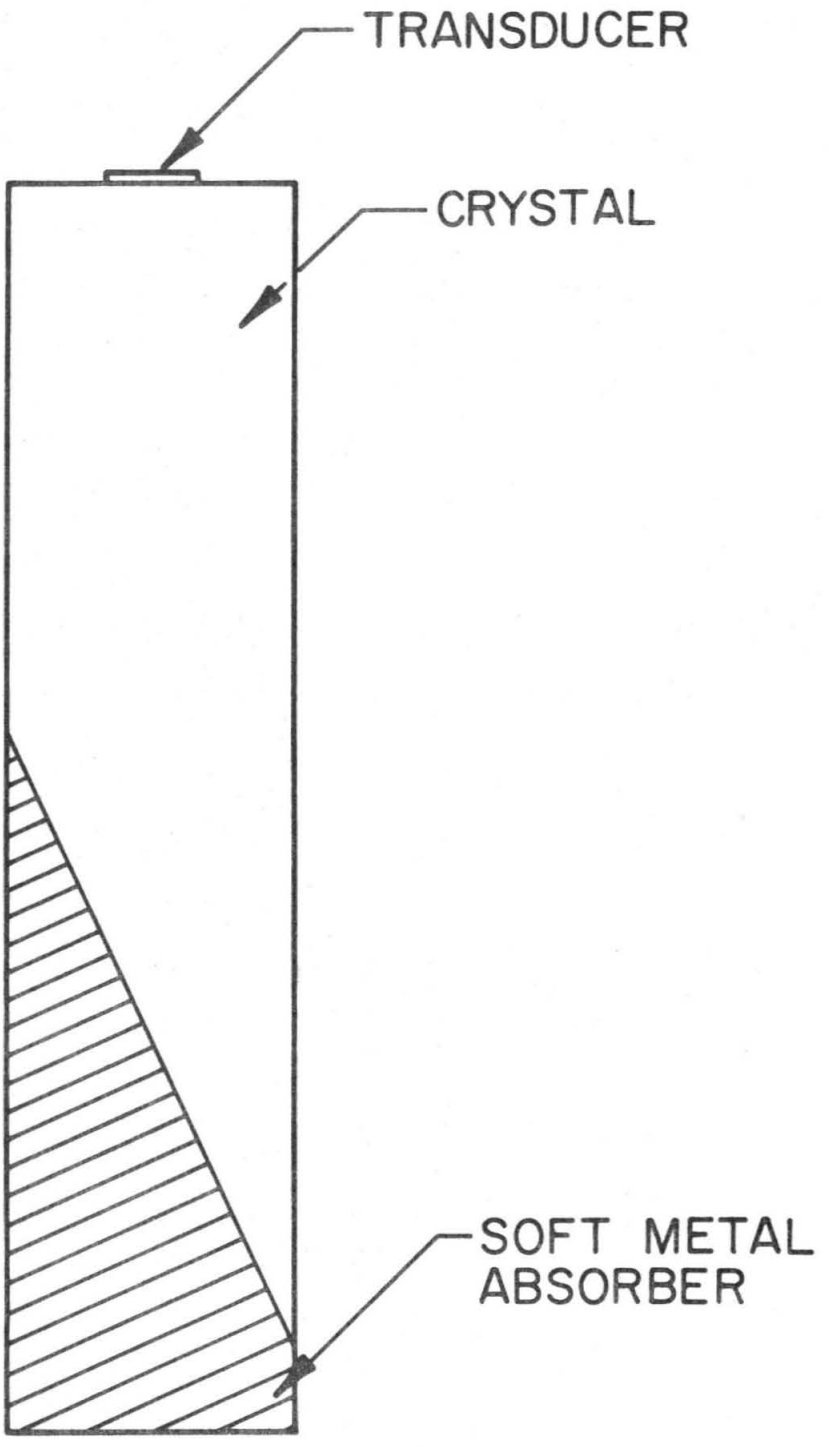

Figure I-8-1. Schematic drawing showing transducer and absorber arrangement for travelling sound wave scattering of laser beam.

9. Conclusion

The temperature dependence of single-crystal elastic constants of synthetic stoichiometric $MgAl_2O_4$, spinel, has been measured by the light-sound scattering in the Raman-Nath region. The crystal is set into forced vibration by a single crystal $LiNbO_3$ transducer coupled to one crystal face. A He-Ne laser beam is diffracted by the stress-induced birefringence inside the crystal. The diffraction angle is determined from the distance of two spots exposed on a photographic plate by the first order diffracted beams as measured by a microdensitometer. The sound wavelength inside the crystal is then inferred from the laser diffraction angle. Combining the sound wavelength with the measured transducer driving frequency, the velocity inside the crystal is determined typically to a precision of 0.05%. In this method, the measurement of velocity is not dependent on either the determination of sample length or on phase shifts at sample-transducer interface. Velocities of four pure modes, L// [001], T// [001], L// [110], and T// [110](P// [1$\bar{1}$0]) are measured in the temperature range between 293K and 423K. A linear temperature dependence is fit to the data by a least square method. Values obtained at 25°C from this linear fit are $V_p[001] = 8.869 \pm 0.013$ km/sec, $(\frac{\partial V}{\partial T})_p = -(3.14 \pm 0.13) \times 10^{-4}$km/sec-K; $V_s[001] = 6.5666 \pm 0.0055$ km/sec, $(\partial V/\partial T)_p = -(1.47 \pm 0.10) \times 10^{-4}$km/sec-K; $V_p[110] = 10.199 \pm 0.011$ km/sec, $(\partial V/\partial T)_p = -(3.20 \pm 0.15) \times 10^{-4}$km/sec-K; $V_s[110](P// [1\bar{1}0]) = 4.2101 \pm 0.0043$ km/sec, $(\partial V/\partial T)_p = -(2.07 \pm 0.06) \times 10^{-4}$km/sec-K. The uncertainties in the velocity derivatives are assigned from a

consistency check. The temperature dependence of the adiabatic elastic constants and bulk and shear (VRH average) moduli is computed using the density and literature value of thermal expansion coefficient. Values obtained are: $C_{11}^S = 2814 \pm 8$ kb, $(\partial C_{11}^S/\partial T)_p = -0.258 \pm 0.018$ kb/K; $C_{12}^S = 1546 \pm 9$ kb, $(\partial C_{12}^S/\partial T)_p = -0.107 \pm 0.019$ kb/K; $C_{44}^S = 1543 \pm 3$ kb, $(\partial C_{44}^S/\partial T)_p = -0.101 \pm 0.010$ kb/K; $K_S = 1969 \pm 6$ kb, $(\partial K_S/\partial T)_p = -0.157 \pm 0.014$ kb/K; $\mu_{VRH} = 1080 \pm 5$ kb, $(\partial \mu_{VRH}/\partial T)_p = -0.094 \pm 0.008$ kb/K. A comparison with previous measurements on stoichiometric single crystal spinel by pulse superposition and ultrasonic interferometry methods is made. The results of the present work are consistent with measurements obtained by Chang and Barsch (1973) by pulse superposition method while disagreeing with the results obtained by O'Connel and Graham (1971) by ultrasonic interferometry through a buffer rod.

An attempt has also been made to measure the pressure dependence of elastic constants of spinel with the same technique. It failed because of the large spurious diffraction introduced by the fluctuation in index of refraction of the pressure fluid. A method to eliminate this spurious effect is discussed. An optical interferometry method is devised to measure the pressure window distortion effect in the pressure dependence measurement. Finally, the present method with its possibility for further improvement is evaluated as a new method to measure temperature and pressure dependence of elastic constants. Other methods using light-sound scattering to measure sound velocities are also reviewed.

REFERENCES

Achar, B.N.N. and G. R. Barsch, Shell model calculation of thermal expansion of alkali halides and magnesium oxide, Phys. Status Solidi (a)6, 247-258 (1971).

Alers, G. A. Use of sound velocity measurements in determining the Debye temperature of solids, in Physical Acoustics, W. P. Mason, ed., IIIB, pp. 1-40, Academic Press, New York, 1965.

Anderson, D. L., R. A. Phinney and C. G. Sammis, Brillouin scattering--a new geophysical tool, in The Application of Modern Physics to the Earth and Planetary Interiors, S. K. Runcorn, ed., pp. 465-477, Wiley-Interscience, London, 1969.

Anderson, D. L., C. G. Sammis, and T. H. Jordan, Composition of the Mantle and Core, in The Nature of the Solid Earth, Eugene C. Robertson, ed., pp. 41-66, McGraw-Hill, Inc., New York, 1972.

Anderson, O. L., Derivation of Wachtman's equation for the temperature dependence of elastic moduli of oxide compounds, Phys. Rev. 144, 553-557 (1966).

Anderson, O. L., E. Schreiber, R.C. Liebermann, and N. Soga, Some elastic constant data on minerals relevant to geophysics, Rev. of Geophys. 6, 491-524 (1968).

Auth, D. C., and W. G. Mayer, Scattering of light reflected from acoustic surface waves in isotropic solids, J. Appl. Phys. 38, 5138-5140 (1967).

Barnes, J. M. and E. A. Hiedemann, Determination of the elastic constants of optical glasses by an ultrasonic method, J. Acoust.

Soc. Amer. 28, 1218-1221 (1956).

Barsch, G. R. and B.N.N. Achar, Shell model calculation of second Grüneisen parameters for alkali halides, Amer. Inst. Phys. Conf. Proc. 3, 211-230, New York, 1972.

Bergmann, L., Der Ultraschall, Hirzel, Zürich, 1954.

Bonnickson, K. R., High-temperature heat contents of aluminates of calcium and magnesium, J. Phys. Chem. 59, 220-221 (1955).

Born, M., and E. Wolf, Principles of Optics, fourth edition, p. 114, 1970a, pp. 503-504, 1970b, Pergamon Press, Oxford, England.

Chang, Z. P. and G. R. Barsch, Pressure dependence of single-crystal elastic constants and anharmonic properties of spinel, J. Geophys. Res. 78, 2418-2433 (1973).

Christensen, N. I., Compressional wave velocities in possible mantle rocks to pressure of 30 kbar, J. Geophys. Res. 79, 407-412 (1974).

Chung, D. H., First pressure derivative of polycrystalline elastic moduli; their relation to single-crystal acoustic data and thermodynamic relations, J. Appl. Phys. 38, 5104-5133 (1967).

Collier, R. J., C. B. Burckhardt, and L. H. Lin, Optical Holography, p. 156, Academic Press, New York, 1971.

Daniels, W. B., Two pumps for generating pressure above 10 kBar, Rev. Sci. Instr. 37, 1502-1504 (1966).

Debye, P. and F. W. Sears, On the scattering of light by supersonic waves, Proc. Nat'l. Acad. Sci. 18, 409-414 (1932).

Dixon, R. W., Acoustic diffraction of light in anisotropic media, J. Quantum Electronics QE-3, 85-93 (1967a).

Extermann, R. and G. Wannier, Theorie de la diffraction de la lumiére par les ultrasons, Helv. Phys. Acta (Switzerland) 9, 520-532 (1936).

Fishman, E. and H. G. Drickamer, Equipment for high pressure optical and spectroscopic studies, Analyt. Chem. 28, 804-805 (1956).

Frisillo, A. L. and G. R. Barsch, Measurement of single-crystal elastic constants of bronzite as a function of pressure and temperature, J. Geophys. Res. 77, 6360-6384 (1972).

Gerlich, D., The elastic constants of cadmium sulfide between 4.2-300°K, J. Phys. Chem. Solids 28, 2575-2579 (1967).

Graham, E. K., Elasticity and composition of the upper mantle, Geophys. J. R. Astr. Soc. 20, 285-302 (1970).

Graham, E. K., and G. R. Barsch, Elastic constants of single-crystal forsterite as a function of temperature and pressure, J. Geophys. Res. 74, 5949-5960 (1969).

Hope, L. L., Brillouin scattering in birefringent media, Phys. Rev. 166, 883-892 (1968).

Horai, K., Thermal conductivity of rock-forming minerals, J. Geophys. Res. 76, 1278-1308 (1971).

Jordan, T. H., and D. L. Anderson, Elastic structures from free oscillations and travel times, Geophys. J. R. Astr. Soc., (in press).

Klein, W. R., and B. D. Cook, Unified approach to ultrasonic light diffraction, IEEE Trans. Sonics and Ultrasonics SU-14, 123-134 (1967).

Krischner, C., Measurement of sound velocities in crystals using Bragg diffraction of light and application to lanthanum fluoride, Appl. Phys. Letters 13, 310-311 (1968).

Krokstad, J. and L. O. Svaasand, Scattering of light by ultrasonic surface waves in quartz, Appl. Phys. Letters 11, 155-157 (1967).

Kumazawa, M., The elastic constants of polycrystalline rock and non-elastic behaviour inherent to them, J. Geophys. Res. 74, 5311-5320 (1969).

Lewis, M. F., Elastic constants of magnesium aluminate spinel, J. Acoust. Soc. Amer. 40, 728-729 (1966).

Malitson, I. H., Refraction and dispersion of synthetic sapphire, J. Opt. Soc. Amer. 52, 1377-1379 (1962).

Mathews, J., and R. L. Walker, Mathematical Methods of Physics, W. A. Benjamin, Inc., New York, pp. 361-369, 1965a; pp. 26-30, 1965b.

Mayer, W. G., and E. A. Hiedemann, Optical methods for the ultrasonic determination of the elastic constants of sapphire, J. Acoust. Soc. Amer. 30, 756-760 (1958).

McSkimin, H. J., Pulse superposition method for measuring ultrasonic wave velocities in solids, J. Acoust. Soc. Amer. 33, 12-16 (1961).

McSkimin, H. J., and P. Andreatch, Analysis of the pulse superposition method for measuring ultrasonic wave velocities as a function of temperature and pressure, J. Acoust. Soc. Amer. 34, 609-615 (1962).

Morse, P. M., Vibration and Sound, p. 329, McGraw-Hill, New York, 1948.

Neighbours, J. R.,and G. E. Schacher, Determination of elastic constants from sound-velocity measurements in crystals of general symmetry, J. Appl. Phys. 38, 5366-5375 (1967).

Nye, J. F., Physical Properties of Crystals, Oxford University Press, London, p. 251, 1957.

O'Connel, R. J., and E. K. Graham, Equation of state of stoichiometric spinel to 10 kbar and 800°K, Trans. Amer. Geophys. Union 52, 359 (1971).

Pine, A. S., Thermal Brillouin scattering in cadmium sulfide: velocity and attenuation of sound: acoustoelectric effects, Phys. Rev. B5, 2997-3003 (1972).

Rigby, G. R., G. H. Lovell, and A. T. Green, Some properties of the spinels associated with chrome ores, Trans. Brit. Ceram. Soc. 45, 137-148 (1946).

Sammis, C. G., Lattice dynamics of MgO,Al_2MgO_4 and Mg_2SiO_4 spinel, Geophys. J. R. Astr. Soc. 29, 15-42 (1972)

Schaefer, C. L., and L. Bergmann, Über neue Beugungserscheinungen an schwingenden Kristallen, Naturwiss. 22, 685 (1934).

Schaefer, C. L., and L. Bergmann, Optische Beugungserscheinungen an schwingenden Kristallen im reflektierten Licht. Experimenteller Teil, Sitz. Ber. Berliner Akad. 245 (1936).

Sittig, E. K., and H. D. Cook, A method for preparing and bonding ultrasonic transducers used in high frequency digital delay lines, Proc. IEEE 56, 1375-1376 (1968).

Spetzler, H., Ph.D. Thesis, California Institute of Technology, Pasadena, 1969.

Spetzler, H., Equation of state of polycrystalline and single-crystal MgO to 8 kilobars and 800°K, J. Geophys. Res. 75, 2073-2087 (1970).

Stromberg, H. D., and R. N. Schock, A window configuration for high pressure optical cells, Rev. Sci. Instr. 41, 1880 (1970).

Thomsen, L., Elasticity of polycrystals and rocks, J. Geophys. Res. 77, 315-327 (1972a).

Thomsen, L., On the effects of pressure upon rock elasticity, Phys. Earth Planet. Interiors 5, 325-327 (1972b).

Thurston, R. N., Wave propagation in fluids and normal solids in Physical Acoustics, W. P. Mason, ed., IA, pp. 2-109, Academic Press, New York, 1964.

Verma, R. K., Elasticity of some high-density crystals, J. Geophys. Res. 65, 757-766 (1960).

Wachtman, J. B., Jr., W. E. Tefft, D. G. Lam, and R. P. Stinchfield, Elastic constants of synthetic single crystal corundum at room temperature, J. Res. Nat. Bur. Std. 64A, 213-228 (1960).

White, R. M., and F. W. Voltmer, Direct piezoelectric coupling to surface elastic waves, Appl. Phys. Letters 7, 314-316 (1965).

Willard, G. W.,Criteria for normal and abnormal ultrasonic light diffraction effects, J. Acoust. Soc. Amer. 21, 101-108 (1949).

Yariv, A., Quantum Electronics, John Wiley and Sons, Inc., New York, p. 301, 1968.

Yariv, A., Introduction to Optical Electronics, Holt, Rinehart and Winston, New York, p 20, 1971a; p. 25, 1971b.

PART II

EFFECT OF ANELASTICITY ON EARTH'S FREE OSCILLATION PERIODS (TOROIDAL MODES)

1. Introduction

The anelasticity of the Earth's interior gives rise to a variety of important phenomena in solid earth geophysics. Examples are: the short period effects such as seismic wave attenuation and tidal dissipation; the long term phenomena such as response of Earth's crust and mantle to loading and unloading on the surface ("isostasy") or the transverse movements of large segments of Earth's upper layer. ("plate tectonics"). The mechanisms responsible for the anelastic behavior of the Earth's interior are largely controlled by defect structure of the crystals making up the rock minerals. A host of such mechanisms, thought applicable to geophysics, are reviewed and listed in the literature (Gordon and Nelson 1966, Jackson and Anderson 1970). Further experimentation under high pressure and temperature pertinent to mantle conditions are necessary to decide their relative importance.

Recently, the attenuation of seismic body and surface waves at different frequencies have been measured. Jackson and Anderson (1970) summarize this information up to 1970. This information from seismology, when carefully interpreted, can serve to put a constraint on the physical mechanisms of anelasticity operating in the Earth's interior.

It will be shown in the present work that anelasticity, as inferred from the seismic wave attenuation data, also produces a non-negligible shift on the periods of Earth's toroidal oscillations. This result implies that in constructing velocity and density models of the Earth using free oscillation data, one has to invert them together with anelastic structure when the free oscillation period measurements have an accuracy limit less than the shift due to anelasticity. Computations

in this work show this limit to be $|\Delta T/T| \sim 2.3 \times 10^{-4}$ for the toroidal oscillations. Dziewonski and Gilbert (1972) recently determined the free oscillation periods excited by the 1964 Alaskan earthquake. The resolution of the fundamental toroidal modes ${}_oT_\ell$ reported by them varies between 0.031% and 0.262% and is generally about 0.1% for the higher frequency toroidal modes ${}_oT_\ell$ at which the anelastic shift becomes important. The magnitude of present observational error is about five times bigger than the shift of free oscillation period due to anelasticity.

2. Derivation of Equations for Shift in Earth's Toroidal Free Oscillations Due to Anelasticity

The equation of motion for the elastic-gravitational oscillation of a nonrotating earth with lateral heterogeneity is given by

$$\rho_o(\omega^m_{k\ell})^2 \underset{\sim}{S}^m_{k\ell} = H(\underset{\sim}{S}^m_{k\ell}, \phi) \tag{II.2-1}$$

and

$$\nabla^2\phi_1 = 4\pi G \nabla\cdot(\rho_o \underset{\sim}{S}^m_{k\ell}) \tag{II.2-2}$$

where ρ_o: equilibrium density distribution

$\underset{\sim}{S}^m_{k\ell}$: displacement field of free oscillation characterized by the mode numbers k, ℓ, and m

$\omega^m_{k\ell}$: angular oscillation frequency

$\rho_1 = -\nabla\cdot(\rho_o \underset{\sim}{S}^m_{k\ell})$, change in density due to displacement

$\phi = \phi_o + \phi_1$, total gravitational potential

ϕ_o: equilibrium gravitational potential

ϕ_1: change in gravitational potential due to free oscillation

G: gravitational constant.

The operator H is defined by its components in Cartesian coordinates (Dahlen 1968) by

$$[H(\underset{\sim}{S},\phi)]_i = -\partial_j(\Gamma_{ijk\ell}\,\sigma_{k\ell}) + \partial_i[\rho_o S_j \partial_j\phi_o] - \nabla\cdot(\rho_o \underset{\sim}{S})\,\partial_i\phi_o$$

$$+ \rho_o\partial_i\phi_1 - \partial_i[S_k\partial_j\tau^o_{kj}] + \partial_j(S_k\partial_k\tau^o_{ij}) + \partial_j[\tfrac{1}{2}\tau^o_{j\ell}(\partial_i S_\ell - \partial_\ell S_i)]$$

$$+ \partial_j[\tfrac{1}{2}\tau^o_{i\ell}(\partial_j S_\ell - \partial_\ell S_j)] \tag{II.2-3}$$

The mode numbers are suppressed in the above equation. In equation (II.2-3) where

$$\sigma_{k\ell} \equiv (\partial_k S_\ell + \partial_\ell S_k)/2$$

$\underset{\approx}{T}^o$: static stress field tensor

$\underset{\approx}{\tau}^o \equiv \underset{\approx o}{T} - \frac{1}{3}(\underset{\approx o}{T})_{ii}\ \underset{\approx}{I}$, is the static stress deviator tensor

$\underset{\approx}{E}$: elastic stress tensor

and the stress-strain relationship (in Cartesian coordinates)

$$E_{ij} = \Gamma_{ijk\ell}\,\sigma_{k\ell} - \frac{1}{2}\,\tau^o_{j\ell}(\partial_i S_\ell - \partial_\ell S_i) - \frac{1}{2}\,\tau^o_{i\ell}(\partial_j S_\ell - \partial_\ell S_j) \quad \text{(II.2-4)}$$

has been used in the equation of motion to obtain the expression for operator $H(\underset{\sim}{S},\phi)$ in equation (II.2-3). $\Gamma_{ijk\ell}$ in equation (II.2-4) are components of the elastic coefficient tensor. The boundary conditions are (Alterman, Jarosch and Pekeris 1959; Backus 1967)

$\underset{\sim}{S}$ continuous, except at mantle-core boundary where only $\hat{\underset{\sim}{n}} \cdot \underset{\sim}{S}$ needs to be continuous

ϕ_1 continuous

$\hat{\underset{\sim}{n}} \cdot \nabla\phi_1 + \underset{\sim}{S} \cdot \hat{\underset{\sim}{n}}\ 4\pi G\ \rho_o$ continuous (II.2-5)

$\hat{\underset{\sim}{n}} \cdot \underset{\approx}{E}$ continuous

where $\hat{\underset{\sim}{n}}$ is the outward normal to a undeformed surface of continuity. Since equation (II.2-2) can be integrated to express $\phi_1(\underset{\sim}{r})$ in terms of the displacement field $\underset{\sim}{S}$

$$\phi_1(\underset{\sim}{r}) = -G \int \nabla \cdot (\rho_o \underset{\sim}{S})\, g(\underset{\sim}{r},\underset{\sim}{r}')\, dV' + G \int \rho_o(\underset{\sim}{r}')\, g(\underset{\sim}{r},\underset{\sim}{r}')\, \underset{\sim}{S}(\underset{\sim}{r}') \cdot \hat{\underset{\sim}{n}}'\, dS' \qquad \text{(II.2-6)}$$

$$g(\underset{\sim}{r},\underset{\sim}{r}') = 1/|\underset{\sim}{r}-\underset{\sim}{r}'|$$

The operator H is hermitian when the density ρ_o is laterally homogeneous. It is not hermitian when the density possesses a lateral heterogeneity. This is discussed by Saito (1971) and the adjoint operator $\tilde{H}$ of the operator H has been constructed by him. The eigenvalue equation of the adjoint operator is

$$\tilde{H}\,(\tilde{\underset{\sim}{S}}^m_{k\ell}) = (\gamma^m_{k\ell})^2\, \rho_o \tilde{\underset{\sim}{S}}^m_{k\ell} \qquad \text{(II.2-7)}$$

with

$$\int \rho_o \tilde{\underset{\sim}{S}}^m_{k\ell} \cdot \underset{\sim}{S}^{m'}_{k'\ell'}\, dV = 0 \quad \text{if } k \neq k',\ \ell \neq \ell' \text{ or } m \neq m'$$

$\tilde{\underset{\sim}{S}}^m_{k\ell}$ is the adjoint solution of $\underset{\sim}{S}^m_{k\ell}$. If H is hermitian, $\tilde{H} = H$, $\gamma^m_{k\ell} = \omega^m_{k\ell}$, and $\tilde{\underset{\sim}{S}}^m_{k\ell} = \overline{\underset{\sim}{S}}^m_k$, where $\bar{\ }$ denotes complex conjugation.

The straightforward way of introducing anelasticity into the equation of motion is to assume a constitutive relation which contains dissipation factors. The simplest such constitutive relation results from introducing complex moduli of elasticity into the linear stress-strain relation as expressed by equation (II.2-4), Anderson and Archambeau (1964). As an illustration, consider the stress-strain relation of a visco-elastic solid,

$$E_{ij} = \lambda\sigma_{ii}\delta_{ij} + 2\mu\sigma_{ij} + \lambda' \frac{\partial\sigma'_{ii}}{\partial t}\delta_{ij} + 2\mu' \frac{\partial\sigma_{ij}}{\partial t} \qquad \text{(II.2-8)}$$

where $\lambda,\lambda', \mu,\mu'$ are real quantities. In the frequency domain (or in response to sinusoidal disturbance) the stress-strain relation (II.2-8) takes the form

$$E_{ij} = (\lambda+i\omega\lambda')\,\sigma_{ii}\delta_{ij} + 2(\mu+i\omega\mu')\sigma_{ij} \qquad \text{(II.2-9)}$$

which shows that a pure imaginary part in the elastic moduli would account for this specific anelastic behavior. Further, a wider class of anelastic behavior can be represented in this manner. In an anisotropic medium, the more general equation corresponding to equation (II.2-9) is

$$[\,\underset{\sim}{A}(\underset{\sim}{S})]_i = -\partial_j(\Gamma^*_{ijk\ell}\sigma_{k\ell}) \qquad \text{(II.2-10)}$$

where $\Gamma^*_{ijk\ell}$ is a tensor with pure imaginary components and having the same form as the elastic tensor $\Gamma_{ijk\ell}$. In an isotropic material, the operator A takes the form

$$\underset{\sim}{A} = -(\lambda^*+2\mu^*)\,\nabla(\nabla\cdot\underset{\sim}{\ }) + \mu^*(\nabla\times(\nabla\times\underset{\sim}{\ })) - (\nabla\lambda^*)\,(\nabla\underset{\sim}{\ })$$

$$-(\nabla\mu^*)\cdot(\nabla\underset{\sim}{\ } + \underset{\sim}{\ }\nabla) \qquad \text{(II.2-11)}$$

where $(\nabla\underset{\sim}{S} + \underset{\sim}{S}\nabla)/2 = \underset{\sim}{i}\,e_{11}\underset{\sim}{i} + \underset{\sim}{j}\,e_{22}\underset{\sim}{j} + \underset{\sim}{k}\,e_{33}\underset{\sim}{k} + e_{12}(\underset{\sim}{i}\underset{\sim}{j} + \underset{\sim}{j}\underset{\sim}{i})$

$$+e_{13}(\underset{\sim}{i}\underset{\sim}{k} + \underset{\sim}{k}\underset{\sim}{i}) + e_{23}(\underset{\sim}{j}\underset{\sim}{k} + \underset{\sim}{k}\underset{\sim}{j})$$

$e_{11} = \frac{\partial S_x}{\partial x}$, $e_{12} = \frac{1}{2}(\frac{\partial S_x}{\partial x} + \frac{\partial S_y}{\partial y})$, etc. in the dyadic notation.

With this anelastic operator A , the eigenvalue equation describing the Earth's free oscillations becomes

$$H\,(\underset{\sim}{S}^m_{k\ell}) + A\,(\underset{\sim}{S}^m_{k\ell}) = \rho_o(\omega^m_{k\ell})^2\ \underset{\sim}{S}^m_{k\ell} \qquad \text{(II.2-12)}$$

Restricting the treatment to an isotropic stress-strain relation, consider the anelastic behavior as a perturbation. The perturbation expansion for angular frequency and displacement field are

$$\begin{aligned}
\omega^m_{k\ell} &= \omega(o)^m_{k\ell} + \omega(1)^m_{k\ell} + \omega(2)^m_{k\ell} + \cdots \\
\gamma^m_{k\ell} &= \gamma(o)^m_{k\ell} + \gamma(1)^m_{k\ell} + \gamma(2)^m_{k\ell} + \cdots \\
\underset{\sim}{S}^m_{k\ell} &= \underset{\sim}{S}(o)^m_{k\ell} + \underset{\sim}{S}(1)^m_{k\ell} + \underset{\sim}{S}(2)^m_{k\ell} + \cdots
\end{aligned} \qquad \text{(II.2-13)}$$

Substituting equation (II.2-13) into equation (II.2-12), the zeroth order equation is

$$H\,(\underset{\sim}{S}(o)^m_{k\ell}) = \rho_o(\omega(o)^m_{k\ell})^2\ \underset{\sim}{S}(o)^m_{k\ell} \qquad \text{(II.2-14)}$$

i.e., the elasto-gravitational oscillation of a non-rotating Earth. The first order equation is

$$\begin{aligned}
H\,(\underset{\sim}{S}(1)^m_{k\ell}) + A\,(\underset{\sim}{S}(o)^m_{k\ell}) &= \rho_o(\omega(o)^m_{k\ell})^2\ \underset{\sim}{S}(1)^m_{k\ell} \\
&\quad + 2\omega(1)^m_{k\ell}\ \omega(o)^m_{k\ell}\ \rho_o\underset{\sim}{S}(o)^m_{k\ell}
\end{aligned} \qquad \text{(II.2-15)}$$

$\underset{\sim}{S}^{(1)}{}^{m}_{k\ell}$ can be expanded in terms of the zeroth order eigenfunctions as

$$\underset{\sim}{S}^{(1)}{}^{m}_{k\ell} = \sum_{m' \neq m} a^{(1)}_{mm'} \underset{\sim}{S}^{(o)}{}^{m'}_{k\ell} + \sum_{k' \neq k} b^{(1)}_{kk'} S^{(o)}{}^{m}_{k'\ell} + \sum_{\ell' \neq \ell} C^{(1)}_{\ell\ell'} S^{(o)}{}^{m}_{k\ell'} \qquad \text{(II.2-16)}$$

Now take the dot product of equation (II.2-15) with $\underset{\sim}{\tilde{S}}^{(o)}{}^{m}_{k\ell}$, the adjoint solution of $\underset{\sim}{S}^{(o)}{}^{m}_{k\ell}$, and integrate over the volume. By definition of the adjoint solution,

$$\int \underset{\sim}{\tilde{S}}^{(o)}{}^{m}_{k\ell} \cdot H(\underset{\sim}{S}^{(1)}{}^{m}_{k\ell}) dV = \int \underset{\sim}{S}^{(1)}{}^{m}_{k\ell} \cdot \tilde{H}(\underset{\sim}{\tilde{S}}^{(o)}{}^{m}_{k\ell}) dV \qquad \text{(II.2-17)}$$

and equation (II.2-7), the first order equation reduces to

$$\omega^{(1)}{}^{m}_{k\ell} = \int \underset{\sim}{\tilde{S}}^{(o)}{}^{m}_{k\ell} \cdot A \underset{\sim}{S}^{(o)}{}^{m}_{k\ell} dV \Big/ \left(2\omega^{(o)}{}^{m}_{k\ell} \int \rho_o \underset{\sim}{\tilde{S}}^{(o)}{}^{m}_{k\ell} \cdot \underset{\sim}{S}^{(o)}{}^{m}_{k\ell} dV\right) \qquad \text{(II.2-18)}$$

Take dot product of equation (II.2-15) and $\underset{\sim}{\tilde{S}}^{(o)}{}^{m'}_{k\ell}$, $m' \neq m$, and since

$$\int \underset{\sim}{\tilde{S}}^{(o)}{}^{m'}_{k\ell} \cdot H(\underset{\sim}{S}^{(1)}{}^{m}_{k\ell}) dV = \int \underset{\sim}{S}^{(1)}{}^{m}_{k\ell} \cdot \tilde{H}(\underset{\sim}{\tilde{S}}^{(o)}{}^{m'}_{k\ell}) dV$$

$$= \int \rho_o (\gamma^{(o)}{}^{m'}_{k\ell})^2 \underset{\sim}{S}^{(1)}{}^{m}_{k\ell} \cdot \underset{\sim}{\tilde{S}}^{(o)}{}^{m'}_{k\ell} dV \qquad \text{(II.2-19)}$$

equation (II.2-15) becomes

$$[(\gamma^{(o)}{}^{m'}_{k\ell})^2 - (\omega^{(o)}{}^{m}_{k\ell})^2] \int \rho_o \underset{\sim}{S}^{(1)}{}^{m}_{k\ell} \cdot \underset{\sim}{\tilde{S}}^{(o)}{}^{m'}_{k\ell} dV$$

$$= - \int \underset{\sim}{\tilde{S}}^{(o)}{}^{m'}_{k\ell} \cdot A(\underset{\sim}{\tilde{S}}^{(o)}{}^{m}_{k\ell}) dV \qquad \text{(II.2-20)}$$

Substituting equation (II.2-16) into equation (II.2-20) gives

$$a_{mm'} = \int \tilde{\underset{\sim}{S}}(o)^{m'}_{k\ell} \cdot A(\underset{\sim}{S}(o)^{m}_{k\ell})dV \Big/ \{[(\omega(o)^{m}_{k\ell})^2 - (\gamma(o)^{m'}_{k\ell})^2] \times \int \rho_o \tilde{\underset{\sim}{S}}(o)^{m'}_{k\ell} \cdot \underset{\sim}{S}(o)^{m'}_{k\ell} dV\} \qquad \text{(II.2-21)}$$

Similarly, expressions for $b_{kk'}$ and $C_{\ell\ell'}$ are obtained by taking dot products of equations with $\tilde{\underset{\sim}{S}}(o)^{m}_{k'\ell}$ and $\tilde{\underset{\sim}{S}}(o)^{m}_{k\ell'}$ respectively and integrating the resulting equation over the entire volume of the Earth. The second order perturbation equation is then

$$H(\underset{\sim}{S}(2)^{m}_{k\ell}) + A(\underset{\sim}{S}(1)^{m}_{k\ell}) = \rho_o[(\omega(1)^{m}_{k\ell})^2 + 2\omega(o)^{m}_{k\ell}\,\omega(2)^{m}_{k\ell}]\underset{\sim}{S}(o)^{m}_{k\ell} + \rho_o(\omega(o)^{m}_{k\ell})^2\,\underset{\sim}{S}(2)^{m}_{k\ell} + 2\rho_o\,\omega(o)^{m}_{k\ell}\,\omega(1)^{m}_{k\ell}\,\underset{\sim}{S}(1)^{m}_{k\ell} \qquad \text{(II.2-22)}$$

Now take the dot product of equation (II.2-22) with $\tilde{\underset{\sim}{S}}(o)^{m}_{k\ell}$ and integrate over the entire volume, with

$$\int \tilde{\underset{\sim}{S}}(o)^{m}_{k\ell} \cdot H(\underset{\sim}{S}(2)^{m}_{k\ell})dV = \int \underset{\sim}{S}(2)^{m}_{k\ell} \cdot \tilde{H}(\tilde{\underset{\sim}{S}}(o)^{m}_{k\ell})dV = \int \rho_o(\gamma(o)^{m}_{k\ell})^2\,\underset{\sim}{S}(2)^{m}_{k\ell} \cdot \tilde{\underset{\sim}{S}}(o)^{m}_{k\ell}\,dV \qquad \text{(II.2-23)}$$

equation (II.2-22) becomes

$$\int \tilde{\underset{\sim}{S}}(o)^m_{k\ell} \cdot A(\underset{\sim}{S}(1)^m_{k\ell})dV + [(\gamma(o)^m_{k\ell})^2 - (\omega(o)^m_{k\ell})^2]$$

$$\cdot \int \rho_o \underset{\sim}{S}(2)^m_{k\ell} \cdot \tilde{\underset{\sim}{S}}(o)^m_{k\ell} \, dV$$

$$= [(\omega(1)^m_{k\ell})^2 + 2\omega(o)^m_{k\ell} \, \omega(2)^m_{k\ell}] \int \rho_o \tilde{\underset{\sim}{S}}(o)^m_{k\ell} \cdot \underset{\sim}{S}(o)^m_{k\ell} dV \qquad \text{(II.2-24)}$$

or

$$\omega(2)^m_{k\ell} =$$

$$\frac{\{\int \tilde{\underset{\sim}{S}}(o)^m_{k\ell} \cdot A(\underset{\sim}{S}(1)^m_{k\ell})dV + [(\gamma(o)^m_{k\ell})^2 - (\omega(o)^m_{k\ell})^2] \int \rho_o \underset{\sim}{S}(2)^m_{k\ell} \cdot \tilde{\underset{\sim}{S}}(o)^m_{k\ell} dV\}}{2\omega(o)^m_{k\ell} \int \rho_o \tilde{\underset{\sim}{S}}(o)^m_{k\ell} \cdot \underset{\sim}{S}(o)^m_{k\ell} dV}$$

$$- \frac{1}{2} (\omega(1)^m_{k\ell})^2 \Big/ \omega(o)^m_{k\ell} \qquad \text{(II.2-25)}$$

This general result is now applied to the toroidal oscillations of the Earth. The displacement field of an elastically isotropic and laterally homogeneous Earth model is taken as the zeroth unperturbed eigenfunction. The operator H associated with such an Earth model is hermitian. Therefore, $\tilde{H} = H$, $\tilde{\underset{\sim}{S}}^m_{k\ell} = \overline{\underset{\sim}{S}}^m_{k\ell}$, and $\gamma^m_{k\ell} = \omega^m_{k\ell}$. The zeroth order displacement field is then (Alterman, Jarosch, and Pekeris 1959)

$$\underset{\sim}{S}(o)^m_{k\ell} = \underset{\sim}{C}^m_{\ell}(\theta,\phi) \, W_{k\ell}(r) \qquad \text{(II.2-26)}$$

where $\underset{\sim}{C}_\ell^m(\theta,\phi)$ is the vector spherical harmonics defined by

$$\underset{\sim}{C}_\ell^m(\theta,\phi) = (\hat{\underset{\sim}{e}}_\theta \frac{\partial}{\partial\theta} + \hat{\underset{\sim}{e}}_\phi \frac{\partial}{\partial\phi}\frac{1}{\sin\theta}) \times (\hat{\underset{\sim}{e}}_r Y_\ell^m(\theta,\phi)) \qquad \text{(II.2-27)}$$

$\hat{\underset{\sim}{e}}_r$, $\hat{\underset{\sim}{e}}_\theta$, $\hat{\underset{\sim}{e}}_\phi$ are unit vectors in spherical polar coordinates, and

$Y_\ell^m(\theta,\phi) = (-)^m[\frac{(2\ell+1)}{4\pi}\frac{(\ell-m)!}{(\ell+m)!}]^{1/2} P_\ell^m(\cos\theta)e^{im\phi}$ is the spherical harmonic function. $W_{k\ell}(r)$ is solution to the equation

$$\mu_s^{(o)}[\frac{1}{r^2}\frac{d}{dr}(r^2\frac{d}{dr}) - \frac{\ell(\ell+1)}{r^2}]\, W_{k\ell}(r) + \rho_s^{(o)}(\omega_{k\ell}^{(o)})^2 W_{k\ell}(r) = 0 \qquad \text{(II.2-28)}$$

for a layered Earth model where $\mu_s^{(o)}$ and $\rho_s^{(o)}$ are rigidity and density inside the layer of index s, $s=1,2,\cdots N$. The boundary conditions for equation (II.2-28) are continuity of $W_{k\ell}(r)$ and $(\mu^{(o)}\frac{d}{dr}W_{k\ell}(r) - W_{k\ell}(r))$ at layer boundaries. The adjoint displacement field is given by

$$\underset{\sim}{\tilde{S}}(o)^m_{k\ell} = \overline{\underset{\sim}{C}}_\ell^m(\theta,\phi)\, W_{k\ell}(r) \qquad \text{(II.2-29)}$$

Assuming a laterally homogeneous anelasticity in the Earth model,

$$\int \underset{\sim}{\tilde{S}}(o)^m_{k\ell} \cdot A(\underset{\sim}{S}(o)^m_{k\ell})dV = (\omega_{k\ell}^{(o)})^2 \int \frac{\mu^*}{\mu^{(o)}}\rho^{(o)} W_{k\ell}(r)W_{k\ell}(r)\, dV \qquad \text{(II.2-30)}$$

and

$$(\omega_{k\ell}^{(o)}) \int \rho^{(o)}\, \underset{\sim}{\tilde{S}}(o)^m_{k\ell} \cdot \underset{\sim}{S}(o)^m_{k\ell}\, dV = (\omega_{k\ell}^{(o)}) \int \rho^{(o)}[W_{k\ell}(r)]^2 dV$$

Substituting equation (II.2-30) into equations (II.2-18), (II.2-21)

and (II.2-25) we get

$$\omega^{(1)m}_{k\ell} = \frac{\{\int \frac{\mu^*}{\mu^{(o)}} \rho^{(o)}[W_{k\ell}(r)]^2\, dV\}\, \omega^{(o)}_{k\ell}}{2\int \rho^{(o)}[W_{k\ell}(r)]^2\, dV}$$

$$\equiv \frac{1}{2}\gamma^{(1)}_{k\ell}\omega^{(o)}_{k\ell}) \qquad \text{(II.2-31)}$$

and

$$\omega^{(2)m}_{k\ell} = (\omega^{(o)}_{k\ell})\left\{\frac{1}{2}\sum_{i\neq k}\frac{\left|\int \frac{\mu^*}{\mu^{(o)}} W_{i\ell}(r)\, W_{k\ell}(r)\, \rho^{(o)}\, dV\right|^2}{\int \rho^{(o)}[W_{i\ell}(r)]^2 dV)(\int \rho^{(o)}[W_{k\ell}(r)]^2 dV)}\right.$$

$$\left.\cdot \frac{(\omega^{(o)}_{i\ell})^2}{(\omega^{(o)}_{i\ell})^2 - (\omega^{(o)}_{k\ell})^2} + \frac{1}{2(\omega^{(o)}_{k\ell})^2}(\omega^{(1)m}_{k\ell})^2\right\}$$

$$\equiv (\omega^{(o)}_{k\ell})\left\{\frac{\gamma^{(2)}_{k\ell}}{2} + \frac{1}{2}\left(\frac{\gamma^{(1)}_{k\ell}}{2}\right)^2\right\} \qquad \text{(II.2-32)}$$

The attenuation factor $(Q^m_{k\ell})$ of the toroidal oscillation is given by

$$(Q^m_{k\ell})^{-1} = 2\,\mathrm{Im}\left(\frac{\omega^{(1)m}_{k\ell}}{\omega^{(o)m}_{k\ell}}\right) = \gamma^{(1)}_{k\ell} \qquad \text{(II.2-33)}$$

and the frequency shift is given by $\omega^{(2)m}_{k\ell}$.

3. Numerical Calculations and Results

In actual computation, a laterally homogeneous Earth model consisting of seismic velocities V_p, V_s, and density $\rho^{(o)}$ as a function of radius is fed into a normal mode program to generate the displacement function $W_{k\ell}(r)$ and angular frequency $\omega^{(o)}_{k\ell}$ for ${}_kT_\ell$, $k=0,1$; $\ell=2,3,\cdots,99$. (m is degenerate for a laterally homogeneous, non-rotating, spherical Earth model). These, together with an intrinsic Q-model as a function of radius, are used to compute the free oscillation dissipation factor $(Q_{k=0,\ell})^{-1}$ and the frequency shift due to anelasticity $\omega^{(2)}_{k=0,\ell}$. Equations (II.2-31), (II.2-32), and (II.2-33) are employed in these computations. Note from equation (II.2-32)

$$\gamma^{(2)}_{k=0,\ell} = \sum_{i=1}^{\infty} \frac{\left| \int \frac{\mu^*}{\mu^{(o)}} W_{i\ell}(r)\, W_{k=0,\ell}(r)\, \rho^{(o)}\, dV \right|^2}{\left[\int \rho^{(o)} [W_{i\ell}(r)]^2 dV\right]\left[\int \rho^{(o)} [W_{k=0,\ell}(r)]^2 dV\right]} \cdot \frac{(\omega^{(o)}_{i\ell})^2}{(\omega^{(o)}_{i\ell})^2 - (\omega^{(o)}_{k=0,\ell})^2} \qquad \text{(II.3-1)}$$

$\gamma^{(2)}_{k=0,\ell}$ is a summation of positive terms since

$$\omega^{(o)}_{i\ell} > \omega^{(o)}_{k=0,\ell} \qquad i=1,2,\cdots \qquad \text{(II.3-2)}$$

The actually computed value

$$i=1\gamma^{(2)}_{k=0,\ell} = \frac{\left| \int \frac{\mu^*}{\mu^{(o)}} \rho^{(o)} W_{k=1,\ell}(r) W_{k=0,\ell} \, dV \right|^2}{\left(\int \rho^{(o)} [W_{k=1,\ell}(r)]^2 dV \right) \left(\int \rho^{(o)} [W_{k=0,\ell}(r)]^2 dV \right)}$$

$$\cdot \frac{(\omega^{(o)}_{k=1,\ell})^2}{(\omega^{(o)}_{k=1,\ell})^2 - (\omega^{(o)}_{k=0,\ell})^2} \qquad \text{(II.3-3)}$$

is the first term of the series (II.3-1) and is the lower limit of the summation. However, as the number of zeros in $W_{k\ell}(r)$ increases with k , the first term of the series is also the largest.

Two laterally homogeneous Earth models are used in the computation, one characteristic of the Basin and Range mantle province (CIT111) after Archambeau et al (1969) and the other characteristic of an oceanic structure (Oceanic Series 304702). These models are described in Tables II.3-1, II.3-2, and Figure II.3-1.

Five intrinsic Q models are employed for the Basin and Range Earth model. Two of them are frequency independent with their low Q zone corresponding to the low velocity channel of the Earth. The only difference between these two Q models, $Q(H_1)$ and $Q(L_1)$, is in their numerical values inside the low Q zone. This type of frequency-independent Q-model was adopted in the early work to construct intrinsic Q-models in the Earth's interior (Anderson and Archambeau 1964). The next two intrinsic Q models, $Q(\omega)_1$ and $Q(\omega)_2$ are based on a single relaxation mechanism for seismic energy dissipation. They are frequency dependent and, except for a scaling factor, are after Jackson's model 10-04 (Jackson 1969). The last intrinsic Q-model for Basin and

Range Earth model $Q(\omega)_3$, is constructed after Solomon (1972). In this model, the Q is independent of frequency above the low velocity zone and is the result of two relaxation mechanisms (one of which is attributed to partial melting) in the low velocity zone. It is frequency dependent through only one relaxation mechanism below the low velocity zone and above the core-mantle boundary. Only frequency independent Q models, $Q(L_2)$ and $Q(H_2)$, are employed for the oceanic Earth model. The Basin and Range Q-models are listed in Table II.3-3. The oceanic Q-models are listed in Table II.3-4. The frequency independent Q-models are also shown in Figure II.3-2.

The computed free oscillation quality factor $Q_{k=0,\ell}$ for various Earth models and for various intrinsic Q-models is plotted in Figures II.3-3 and II.3-4. The attenuation data for free oscillations and surface waves up to 1970 have been collected by Jackson and Anderson (1970). The toroidal oscillation and Love wave attenuation data reproduced in Figures II.3-3 and II.3-4 with the various computed $Q_{k=0,\ell}$ are from this collection except for the twelve points at the lower right corner, which are from Solomon (1972). The attenuation data included in Figures II.3-3 and II.3-4 are Nowroozi (1968; ${}_oT_\ell$), Alsop et al (1961; ${}_oT_\ell$), MacDonald and Ness (1961; ${}_oT_\ell$), Smith (1961; ${}_oT_\ell$), Solomon (1972; Love wave), Savarenskii et al (1966; Love wave), Bath and Lopez-Arroyo (1962; Love wave), Press et al (1961; Love wave), Satô (1958; Love wave), Wilson (1940; Love wave), Gutenberg (1924; Love wave). It appears that the intrinsic Q-models $Q(H_1)$, $Q(H_2)$, and $Q(\omega)_1$ give seismic attenuation which agrees well with the observed

data. However, noting the wide scatter of seismic attenuation data and some recent results of surface wave attenuation in the western United States (Solomon 1972), the low $Q_{k=0,\ell}$ values produced by the intrinsic Q models, $Q(L_1)$, $Q(L_2)$, and $Q(\omega)_2$, cannot be ruled out as unreasonable. Values of $Q_{k=0,\ell}$ calculated from $Q(\omega)_3$, the most sophisticated among the Q-models, matches well both the long period free oscillation attenuation data and short period Love wave attenuation data in the western United States. Shifts in free oscillation periods calculated from this intrinsic Q-model, $Q(\omega)_3$, are taken to be representative. The period shift

$$\left|{}_{i=1}(DT)_{k=0,\ell}\right| = T_{k=0,\ell}\left|\frac{{}_{i=1}\omega^{(2)}_{k=0,\ell}}{\omega_{k=0,\ell}}\right|$$

$$= T_{k=0,\ell}\ \frac{{}_{i=1}\gamma^{(2)}_{k=0,\ell}}{2} + \frac{1}{2}\left(\frac{\gamma^{(1)}_{k=0,\ell}}{2}\right)^2 \qquad \text{(II.3-4)}$$

and the percentage period shift, $\left|{}_{i=1}(DT)_{k=0,\ell}/T_{k=0,\ell}\right|$, as calculated from various Earth and intrinsic Q-models are plotted in Figures II.3-5 and II.3-6. The maximum values of $|DT/T|$ and the modes at which they occur are listed in Table II.3-5 for various Earth and intrinsic Q models. When appropriate ($\ell \gg 1$), the shift in free oscillation period is also expressed in shift in phase and group velocities of surface waves according to Press (1964). The phase and group velocities of the two Earth models are plotted in Figure II.3-7. The shift in phase and group velocities for various Earth and intrinsic Q-models are plotted in Figures II.3-8 and II.3-9.

TABLE II-3-1

CIT 111 Basin and Range Earth Elastic Model

MODEL INPUT IN STANDARD FORM.

TITLE: BASIN AND RANGE

CODE: 111 NO.PTS: 70

INDEX	RADIUS	DENSITY	VP	VS	GRAVITY
1	0.0	1.26200E 01	1.16375E 01	0.0	0.0
2	4.80000E 02	1.25830E 01	1.16375E 01	0.0	1.78319E 02
3	8.00000E 02	1.25123E 01	1.16375E 01	0.0	2.86197E 02
4	1.07849E 03	1.24202E 01	1.16375E 01	0.0	3.80575E 02
5	1.07849E 03	1.24202E 01	1.10900E 01	0.0	3.80575E 02
6	1.16286E 03	1.23740E 01	1.09300E 01	0.0	4.15572E 02
7	1.30115E 03	1.23151E 01	1.01100E 01	0.0	4.65081E 02
8	1.60202E 03	1.21415E 01	9.95904E 00	0.0	5.54626E 02
9	1.92202E 03	1.19115E 01	9.74884E 00	0.0	6.57413E 02
10	2.24202E 03	1.16353E 01	9.48778E 00	0.0	7.56066E 02
11	2.56202E 03	1.13001E 01	9.16066E 00	0.0	8.49804E 02
12	2.88202E 03	1.09183E 01	8.76934E 00	0.0	9.37662E 02
13	3.20202E 03	1.04731E 01	8.35837E 00	0.0	1.01670E 03
14	3.47900E 03	1.00500E 01	8.04000E 00	0.0	1.08254E 03
15	3.47900E 03	5.51000E 00	1.36710E 01	7.30000E 00	1.08254E 03
16	3.65643E 03	5.41659E 00	1.36182E 01	7.26856E 00	1.05738E 03
17	3.89643E 03	5.29729E 00	1.33198E 01	7.15484E 00	1.03238E 03
18	4.13643E 03	5.17729E 00	1.30254E 01	7.03751E 00	1.01539E 03
19	4.57100E 03	4.94561E 00	1.25500E 01	6.84800E 00	9.98546E 02
20	4.77100E 03	4.84782E 00	1.23300E 01	6.76000E 00	9.95811E 02
21	4.87100E 03	4.79622E 00	1.22100E 01	6.71700E 00	9.94781E 02
22	4.97100E 03	4.74050E 00	1.20800E 01	6.66700E 00	9.94340E 02
23	5.07100E 03	4.68451E 00	1.19400E 01	6.62100E 00	9.94250E 02
24	5.17100E 03	4.62992E 00	1.18000E 01	6.55400E 00	9.94426E 02
25	5.27100E 03	4.57531E 00	1.16800E 01	6.49600E 00	9.94930E 02
26	5.31100E 03	4.55347E 00	1.16500E 01	6.48000E 00	9.95175E 02
27	5.31700E 03	4.55019E 00	1.12800E 01	6.27400E 00	9.95370E 02
28	5.39100E 03	4.50500E 00	1.12300E 01	6.24600E 00	9.95802E 02
29	5.43100E 03	4.48000E 00	1.12000E 01	6.22900E 00	9.96193E 02
30	5.47100E 03	4.45247E 00	1.11700E 01	6.22300E 00	9.96550E 02
31	5.49100E 03	4.43985E 00	1.11600E 01	6.21700E 00	9.96748E 02
32	5.51100E 03	4.42450E 00	1.11450E 01	6.20900E 00	9.96926E 02
33	5.53100E 03	4.40905E 00	1.11300E 01	6.20000E 00	9.97098E 02
34	5.57100E 03	4.37000E 00	1.10850E 01	6.17500E 00	9.97432E 02
35	5.59100E 03	4.34995E 00	1.10550E 01	6.14800E 00	9.97585E 02
36	5.61100E 03	4.33103E 00	1.10300E 01	6.13500E 00	9.97740E 02
37	5.63100E 03	4.31092E 00	1.10000E 01	6.11800E 00	9.97876E 02
38	5.65100E 03	4.29040E 00	1.09700E 01	6.09300E 00	9.97996E 02
39	5.67100E 03	4.26901E 00	1.09600E 01	6.08700E 00	9.98108E 02
40	5.69100E 03	4.24500E 00	1.09400E 01	6.06600E 00	9.98204E 02
41	5.71100E 03	4.22011E 00	1.09300E 01	6.06100E 00	9.98302E 02
42	5.72600E 03	4.19950E 00	1.04300E 01	5.77400E 00	9.98355E 38
43	5.74100E 03	4.17650E 00	1.00000E 01	5.53600E 00	9.98390E 02
44	5.77100E 03	4.13041E 00	9.95000E 00	5.50000E 00	9.98438E 02
45	5.82100E 03	4.04082E 00	9.90000E 00	5.46400E 00	9.98348E 02
46	5.87100E 03	3.93995E 00	9.85000E 00	5.41800E 00	9.97983E 02
47	5.92100E 03	3.81000E 00	9.80000E 00	5.37300E 00	9.97257E 02
48	5.97100E 03	3.68195E 00	9.75000E 00	5.32900E 00	9.96240E 02
49	5.97300E 03	3.67750E 00	9.10000E 00	4.97400E 00	9.96200E 02
50	5.99600E 03	3.63427E 00	8.73000E 00	4.76400E 00	9.95576E 02
51	6.02100E 03	3.59401E 00	8.63000E 00	4.70200E 00	9.94867E 02
52	6.07100E 03	3.53000E 00	8.53000E 00	4.63900E 00	9.93351E 02
53	6.12100E 03	3.48258E 00	8.43500E 00	4.56400E 00	9.91757E 02
54	6.17100E 03	3.45000E 00	8.36000E 00	4.46900E 00	9.90156E 02
55	6.19100E 03	3.44030E 00	8.34000E 00	4.43400E 00	9.89518E 02
56	6.20100E 03	3.43750E 00	8.33500E 00	4.43200E 00	9.89225E 02
57	6.22500E 03	3.43400E 00	8.32500E 00	4.41800E 00	9.88905E 02
58	6.22500E 03	3.43400E 00	7.90000E 00	4.19200E 00	9.88505E 02
59	6.23100E 03	3.43350E 00	7.80000E 00	4.13900E 00	9.86370E 38
60	6.24100E 03	3.43127E 00	7.74000E 00	4.10800E 00	9.88057E 02
61	6.25100E 03	3.43075E 00	7.72500E 00	4.10700E 00	9.87736E 02
62	6.28100E 03	3.42994E 00	7.71900E 00	4.14000E 00	9.86918E 02
63	6.29100E 03	3.42994E 00	7.71500E 00	4.18100E 00	9.86652E 02
64	6.31100E 03	3.43026E 00	7.71500E 00	4.26500E 00	9.86112E 02
65	6.32600E 03	3.43028E 00	7.71900E 00	4.33300E 00	9.85725E 02
66	6.34300E 03	3.42810E 00	7.72000E 00	4.35900E 00	9.85510E 02
67	6.34300E 03	3.42810E 00	6.70000E 00	3.78300E 00	9.85310E 02
68	6.35700E 03	3.42795E 00	6.60000E 00	3.73700E 00	9.85012E 02
69	6.35700E 03	3.42795E 00	6.20000E 00	3.51100E 00	9.85012E 02
70	6.37100E 03	3.42756E 00	6.00000E 00	3.40700E 00	9.84836E 02

TABLE II-3-2

Oceanic Earth Elastic Model

MODEL INPUT IN STANDARD FORM.

TITLE: OCEANIC SERIES

CODE: 304702 NO.PTS: 60

INDEX	RADIUS	DENSITY	VP	VS	GRAVITY
1	0.0	1.26200E 01	1.16375E 01	0.0	0.0
2	4.80000E 02	1.25830E 01	1.16375E 01	0.0	1.78319E 02
3	8.00000E 02	1.25123E 01	1.16375E 01	0.0	2.86197E 02
4	1.07849E 03	1.24202E 01	1.16375E 01	0.0	3.80575E 02
5	1.07849E 03	1.24202E 01	1.10900E 01	0.0	3.80575E 02
6	1.18286E 03	1.23740E 01	1.09300E 01	0.0	4.15572E 02
7	1.30115E 03	1.23151E 01	1.01100E 01	0.0	4.55081E 02
8	1.60202E 03	1.21415E 01	9.95904E 00	0.0	5.54626E 02
9	1.92202E 03	1.19115E 01	9.74884E 00	0.0	6.57413E 02
10	2.24202E 03	1.16353E 01	9.48778E 00	0.0	7.56068E 02
11	2.56202E 03	1.13001E 01	9.16066E 00	0.0	8.49804E 02
12	2.88202E 03	1.09183E 01	8.76934E 00	0.0	9.37662E 02
13	3.20202E 03	1.04731E 01	8.35837E 00	0.0	1.01870E 03
14	3.47900E 03	1.00500E 01	8.04000E 00	0.0	1.08254E 03
15	3.47900E 03	5.51000E 00	1.36710E 01	7.30000E 00	1.08254E 03
16	3.65643E 03	5.41659E 00	1.36182E 01	7.26856E 00	1.05738E 03
17	3.89643E 03	5.29729E 00	1.33198E 01	7.15484E 00	1.03238E 03
18	4.13643E 03	5.17729E 00	1.30254E 01	7.03751E 00	1.01539E 03
19	4.37643E 03	5.05696E 00	1.27788E 01	6.92733E 00	1.00446E 03
20	4.61643E 03	4.92649E 00	1.25211E 01	6.80733E 00	9.97982E 02
21	4.85643E 03	4.80434E 00	1.22317E 01	6.68447E 00	9.94891E 02
22	5.09643E 03	4.67062E 00	1.18912E 01	6.54580E 00	9.94251E 02
23	5.33643E 03	4.53958E 00	1.15279E 01	6.38712E 00	9.95346E 02
24	5.54050E 03	4.40006E 00	1.12034E 01	6.17847E 00	9.97138E 02
25	5.65224E 03	4.29022E 00	1.10055E 01	5.97256E 00	9.98000E 02
26	5.72100E 03	4.20539E 00	1.09000E 01	5.80711E 00	9.98340E 02
27	5.72100E 03	4.20539E 00	1.02600E 01	5.80711E 00	9.98340E 02
28	5.76100E 03	4.14600E 00	9.99000E 00	5.69142E 00	9.98427E 02
29	5.80100E 03	4.07896E 00	9.88667E 00	5.56000E 00	9.98398E 02
30	5.84100E 03	4.00324E 00	9.79667E 00	5.41502E 00	9.98225E 02
31	5.88100E 03	3.91575E 00	9.72000E 00	5.26184E 00	9.97876E 02
32	5.91100E 03	3.83880E 00	9.65500E 00	5.14681E 00	9.97471E 02
33	5.94100E 03	3.75850E 00	9.56000E 00	5.03233E 00	9.96926E 02
34	5.95600E 03	3.71866E 00	9.46000E 00	4.97582E 00	9.96598E 02
35	5.97600E 03	3.67034E 00	9.46000E 00	4.90171E 00	9.96110E 02
36	5.97600E 03	3.67034E 00	9.06700E 00	4.90171E 00	9.96110E 02
37	5.98600E 03	3.65190E 00	8.80000E 00	4.86542E 00	9.95848E 02
38	5.99600E 03	3.63427E 00	8.78000E 00	4.82955E 00	9.95578E 02
39	6.00600E 03	3.61766E 00	8.73000E 00	4.79413E 00	9.95300E 02
40	6.03100E 03	3.58003E 00	8.63500E 00	4.70807E 00	9.94575E 02
41	6.07100E 03	3.53000E 00	8.54821E 00	4.58000E 00	9.93351E 02
42	6.08400E 03	3.51615E 00	8.52000E 00	4.54172E 00	9.92941E 02
43	6.10100E 03	3.49568E 00	8.46300E 00	4.49469E 00	9.92398E 02
44	6.12100E 03	3.48258E 00	8.42000E 00	4.44453E 00	9.91757E 02
45	6.14100E 03	3.46783E 00	8.36700E 00	4.40088E 00	9.91114E 02
46	6.17100E 03	3.45000E 00	8.32010E 00	4.35000E 00	9.90156E 02
47	6.17100E 03	3.45000E 00	7.70000E 00	4.35000E 00	9.90156E 02
48	6.22100E 03	3.43442E 00	7.70000E 00	4.31394E 00	9.88613E 02
49	6.25100E 03	3.43079E 00	7.70000E 00	4.33003E 00	9.87736E 02
50	6.27600E 03	3.42994E 00	7.70000E 00	4.37016E 00	9.87041E 02
51	6.28600E 03	3.42994E 00	7.70000E 00	4.39388E 00	9.86774E 02
52	6.31450E 03	3.43026E 00	7.70000E 00	4.48852E 00	9.86043E 02
53	6.32300E 03	3.43028E 00	7.70010E 00	4.52514E 00	9.85834E 02
54	6.32300E 03	3.43028E 00	8.20100E 00	4.52514E 00	9.85834E 02
55	6.35300E 03	3.42799E 00	8.20010E 00	4.75618E 00	9.84903E 02
56	6.36400E 03	3.42795E 00	8.20010E 00	4.76330E 00	9.84880E 02
57	6.36400E 03	3.42795E 00	6.41000E 00	4.76330E 00	9.84880E 02
58	6.36600E 03	3.42756E 00	6.41000E 00	4.77774E 00	9.84836E 02
59	6.36600E 03	1.03000E 00	1.51000E 00	0.0	9.84836E 02
60	6.37100E 03	1.03000E 00	1.51000E 00	0.0	9.84836E 02

TABLE II-3-3

Basin & Range Intrinsic Q Models

Depth, z (km)	$Q(L_1)$	$Q(H_1)$	$Q(\omega)_1$	$Q(\omega)_2$	$Q(\omega)_3$
0-28	200	200	$Q^{-1}(\omega) \equiv Q^{-1}(\omega; A, \tau_o, E^*, V^*) = A\omega\tau/(1+\omega^2\tau^2)$		$Q^{-1} = 0.1\left[\frac{1000}{\omega\tau_1/(1+\omega^2\tau_1^2) + \omega\tau_2/(1+\omega^2\tau_2^2)}\right]$
28-45	120	130			
45-60	35	55			
60-80	20	43			
80-140	10	36	$\tau = \tau_o \exp[(E^*+PV^*)/RT]$		$\tau_2 = 4\times10^{-4}\tau_1$†
140-146	15	38	$\tau = 0.4$ sec		
146-170	315	325	$E^* = 10$ kcal/mole		
170-180	615	615	$V^* = 4$ cm^3/mole		
180-200	655	655	Pressure Model: Bullen Model B (Bullen 1965)		$Q^{-1} = 0.1\omega\tau_3/(1+\omega^2\tau_3^2)$
200-250	755	755	Temperature Model: MacDonald Model 19 (MacDonald 1959)		$\tau_3 = 2$ sec
250-300	860	860			
300-350	965	965			
350-375	1078	1078			
375-398	1190	1190			
398-400	1443	1443			
400-450	1645	1645			
450-500	1695	1695			
500-550	1745	1745	A=0.032	A=0.060	
550-600	1795	1795			
600-630	1835	1835			
630-645	1858	1858			
645-660	1973	1973			
660-680	2090	2090			
680-700	2110	2110			
700-720	2130	2130			
720-740	2150	2150			
740-760	2170	2170			
760-780	2190	2190			
780-800	2210	2210			
800-840	2240	2240			
840-860	2270	2270			
860-880	2290	2290			
880-900	2310	2310			
900-940	2340	2340			
940-980	2370	2370			
980-1054	2390	2390			
1054-2892	2400	2400			
2892-6371	0	0			

† $\tau_1 = 20\exp\left[-(500E^*+584V^*)/1239+(500E^*+4zV^*)/T\right]$ sec; $E^* = 57$ kcal/mole, $V^* = 1.0$ cm^3/mole; Temperature Model 200029 after Minster & Archambeau (1971)

TABLE II-3-4

Oceanic Frequency-independent Intrinsic Q Models

Depth (km)	$Q(L_2)$	$Q(H_2)$
0-5	0	0
5-48	200	200
48-200	10	35
200-395	80	80
395-446	100	100
446-825	300	300
825-1155	800	800
1155-2892	1600	1600
2892-6371	0	0

TABLE II-3-5

Maximum Percentage Shift of Toroidal Free Oscillation Period Calculated from Various Earth Elastic and Intrinsic Q Models

Earth Elastic Model	Earth Intrinsic Q Model	Free Oscillation Mode at Which Maximum Occurs	Calculated Free Oscillation Period (sec)	Maximum Value of Percentage Shift $\times 10^{-4}$
Oceanic	$Q(L_2)$	${}_0T_{92}$	92.89	-13.104
Oceanic	$Q(H_2)$	${}_0T_{99}$	86.63	-1.0936
Basin & Range	$Q(L_1)$	${}_0T_{62}$	140.43	-5.4140
Basin & Range	$Q(H_1)$	${}_0T_{68}$	129.29	-0.7396
Basin & Range	$Q(\omega)_1$	${}_0T_{30}$	261.68	-0.3815
Basin & Range	$Q(\omega)_2$	${}_0T_{30}$	261.68	-1.3412
Basin & Range	$Q(\omega)_3$	${}_0T_{60}$	144.59	-2.3022

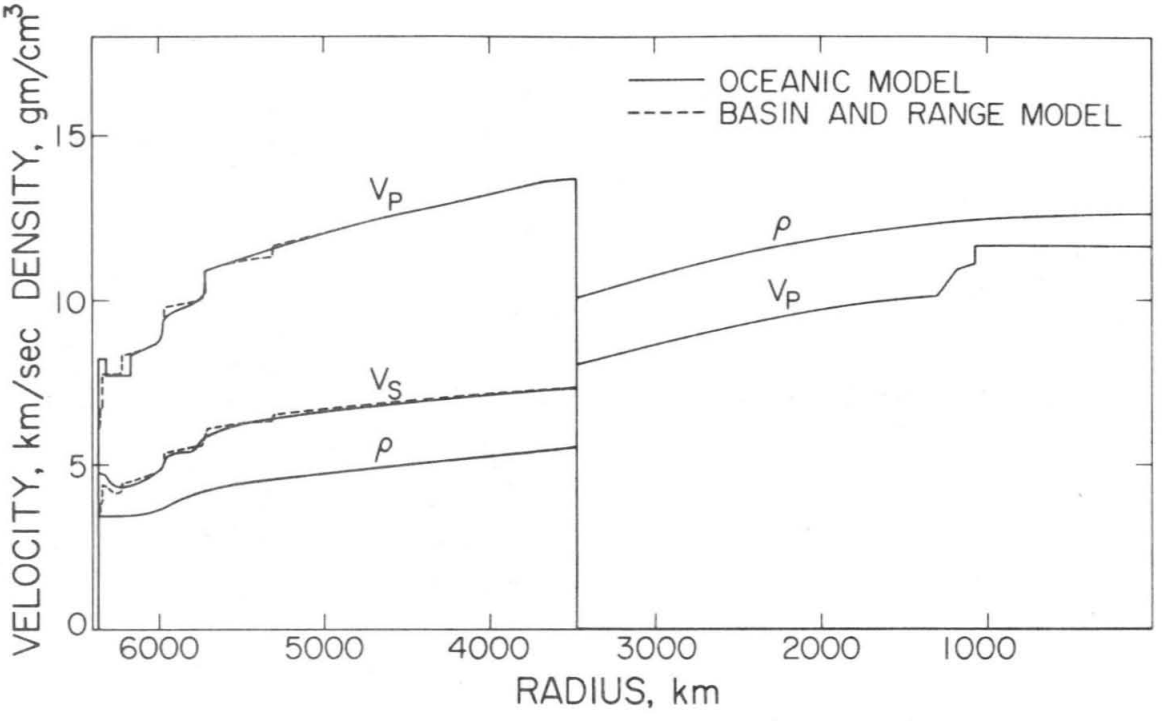

Figure II-3-1. Laterally homogeneous Earth elastic models used in the perturbation calculations.

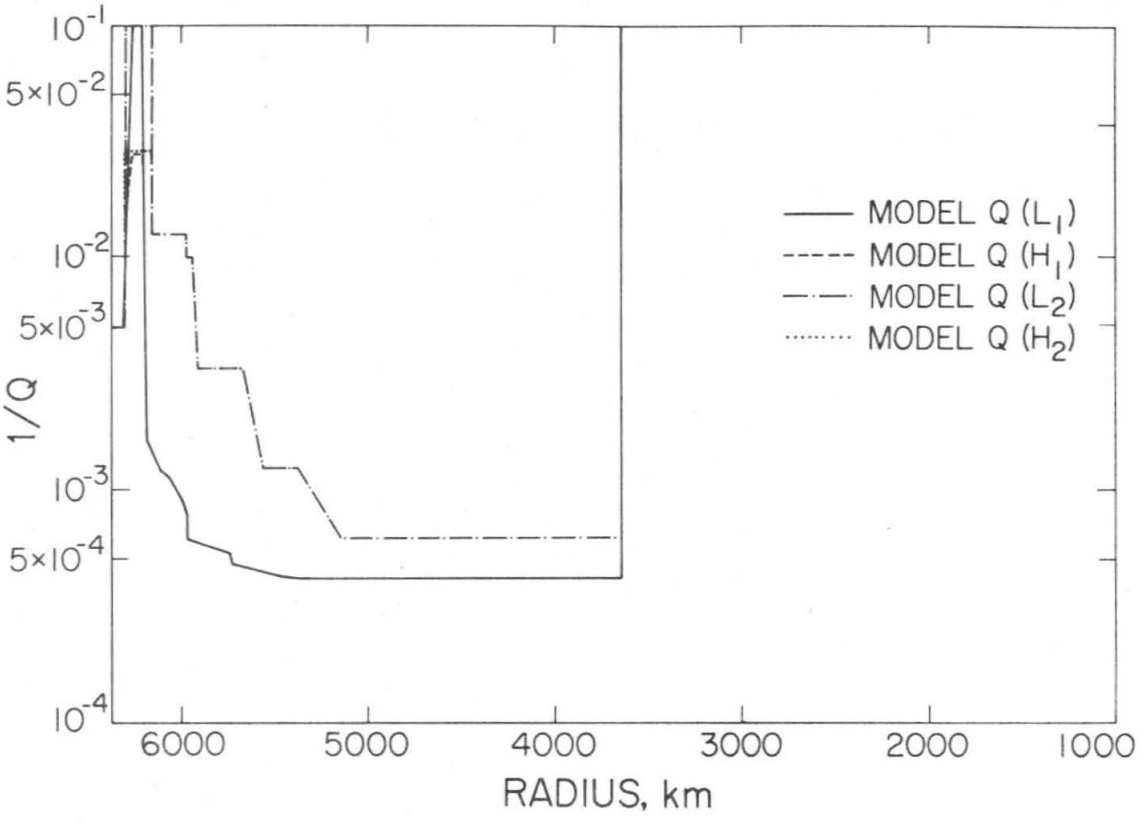

Figure II-3-2. The frequency-independent Earth intrinsic Q models used in the perturbation calculations. Numerical values of these Q models are listed in Tables II-3-3 and II-3-4.

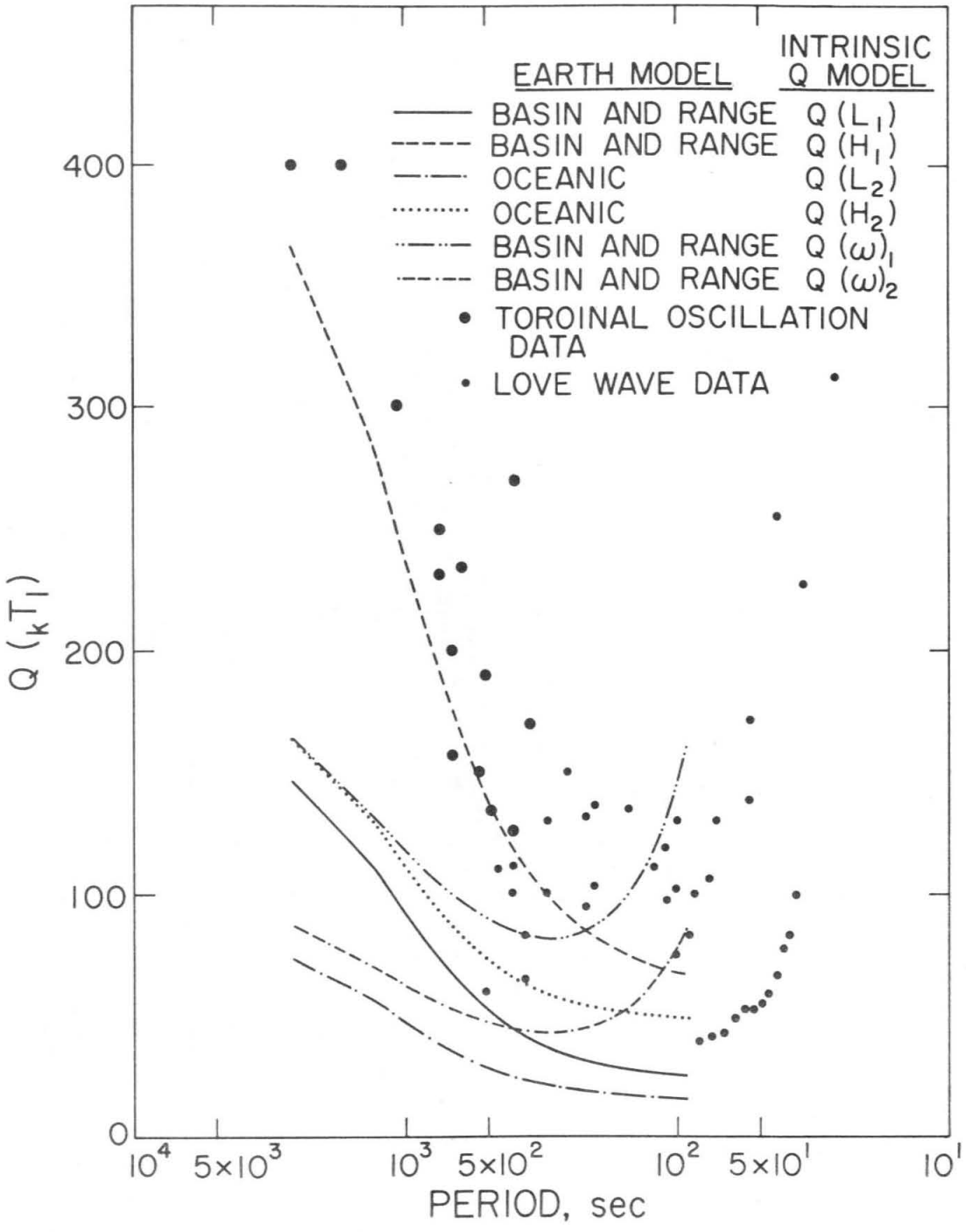

Figure II-3-3. Free oscillation quality factor (fundamental toroidal modes) calculated from various Earth elastic and intrinsic Q models as compared with the observational data. The observational data are from Gutenberg(1924), Wilson(1940), Satô(1958), Alsop et al.(1961), Press et al.(1961), MacDonald and Ness(1961), Smith(1961), Båth and Lopez-Arroyo(1962), Nowroozi(1968), and Solomon(1972).

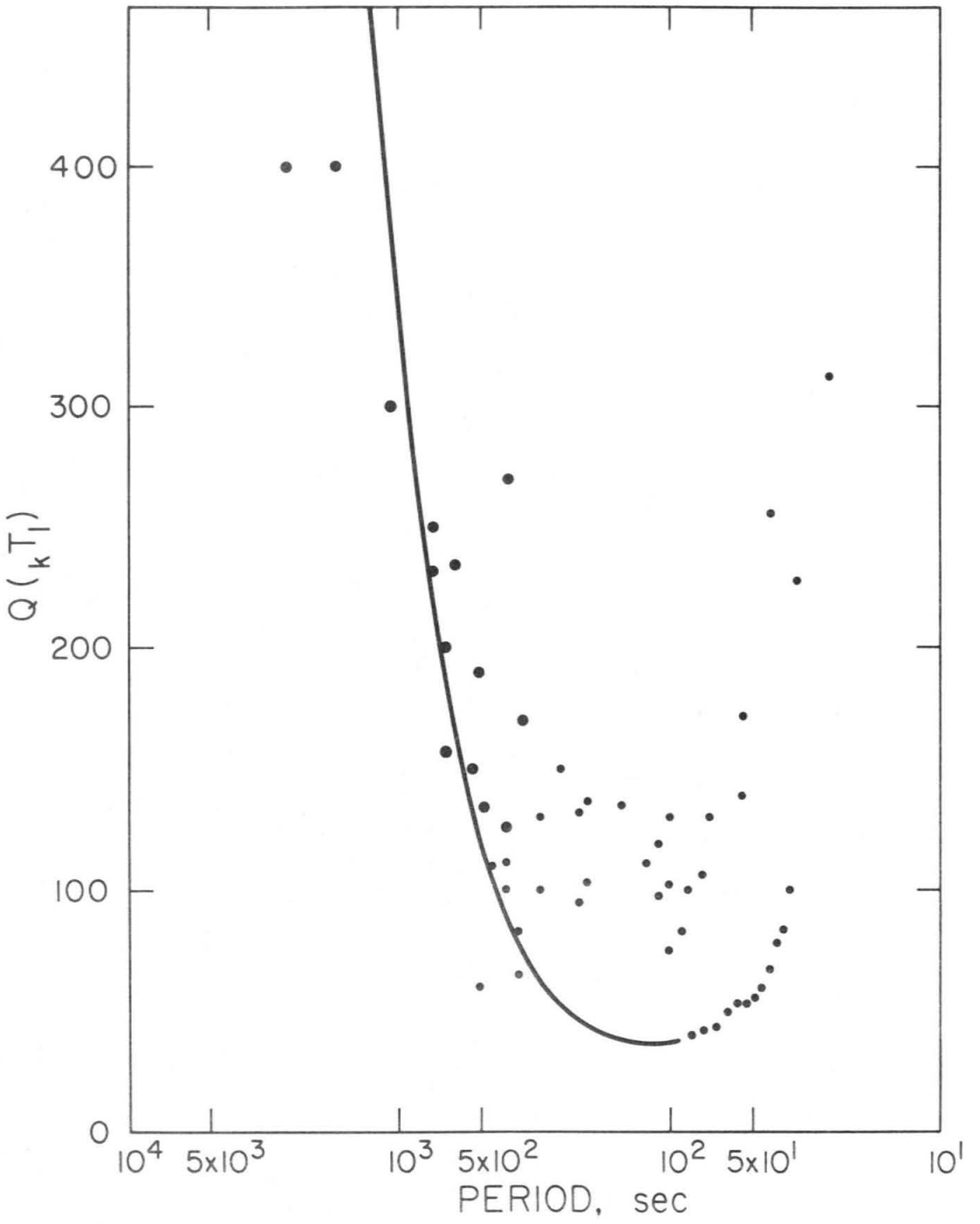

Figure II-3-4. Free oscillation quality factor (fundamental toroidal modes) calculated from the Earth Basin and Range elastic model and the frequency-dependent intrinsic Q model, $Q(\omega)_3$, as compared with the same observational data as those in figure II-3-3. The fit is much better than those in figure II-3-3.

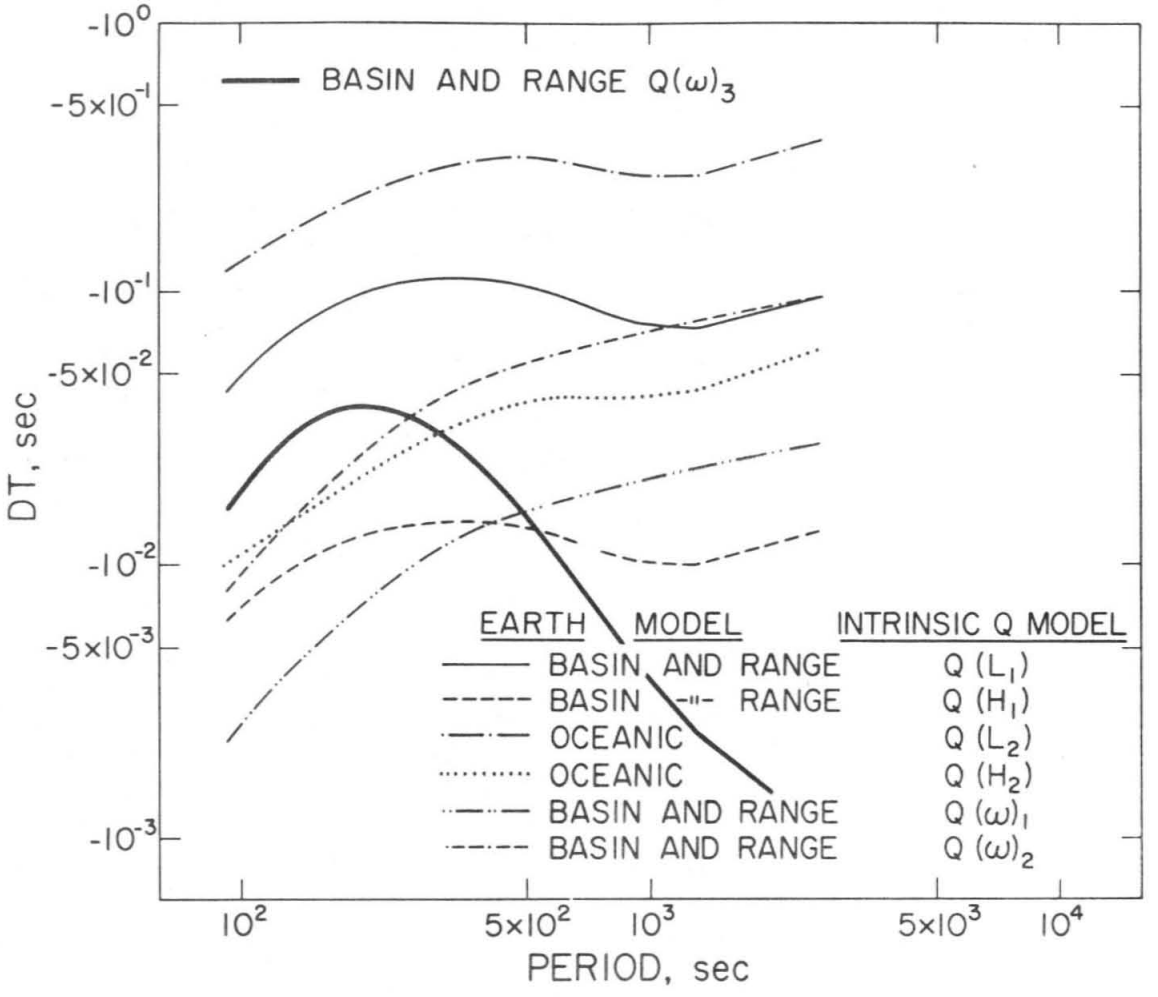

Figure II-3-5. Shift in toroidal free oscillation (fundamental modes) periods, DT, due to anelasticity as calculated from various Earth elastic and intrinsic Q models.

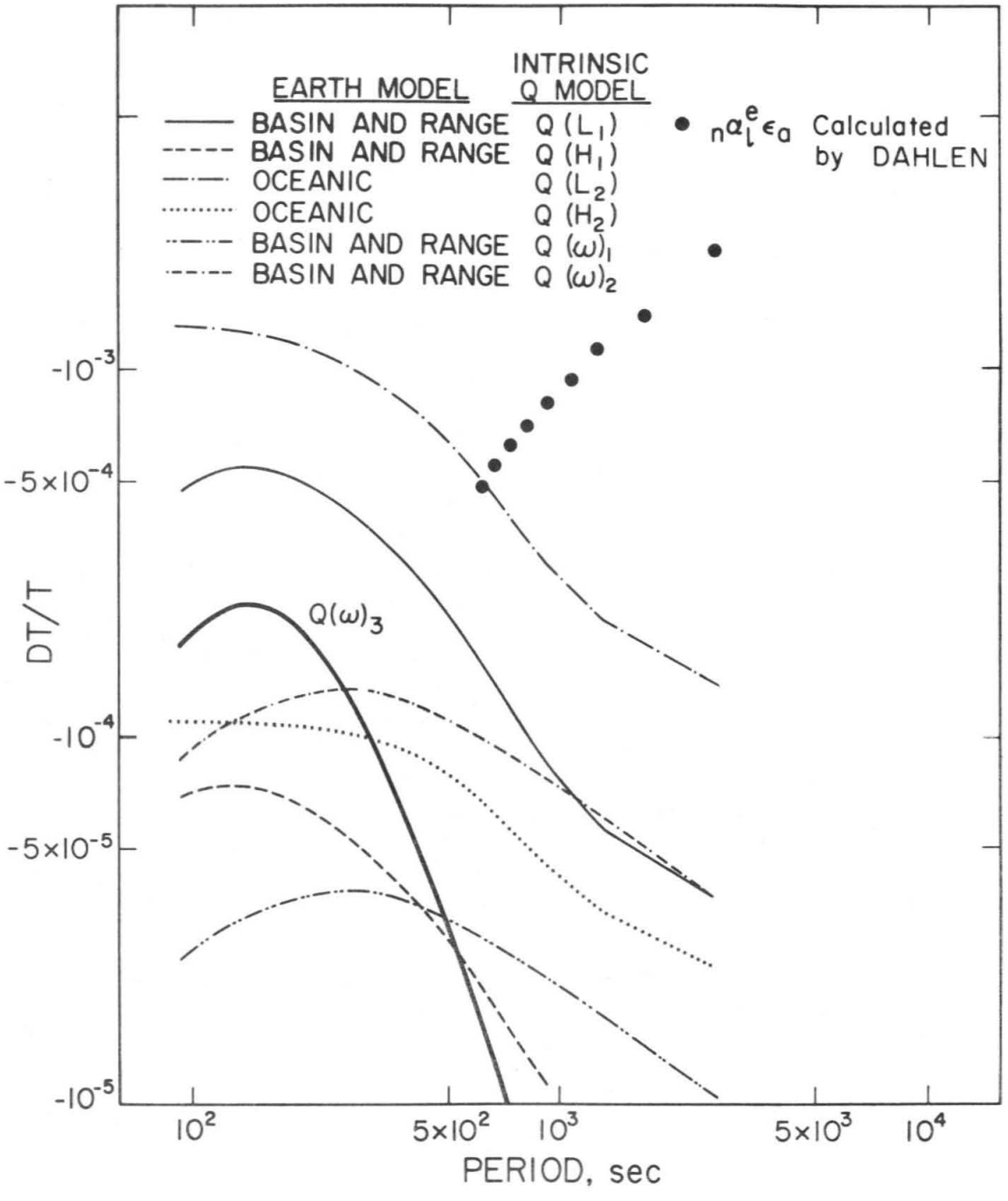

Figure II-3-6. Percentage shift in fundamental toroidal free oscillation periods, DT/T, due to anelasticity as calculated from various Earth elastic and intrinsic Q models. The values $n\alpha_l^e \epsilon_a$ calculated by Dahlen (1968) are the percentage shift of toroidal oscillation periods due to ellipticity alone.

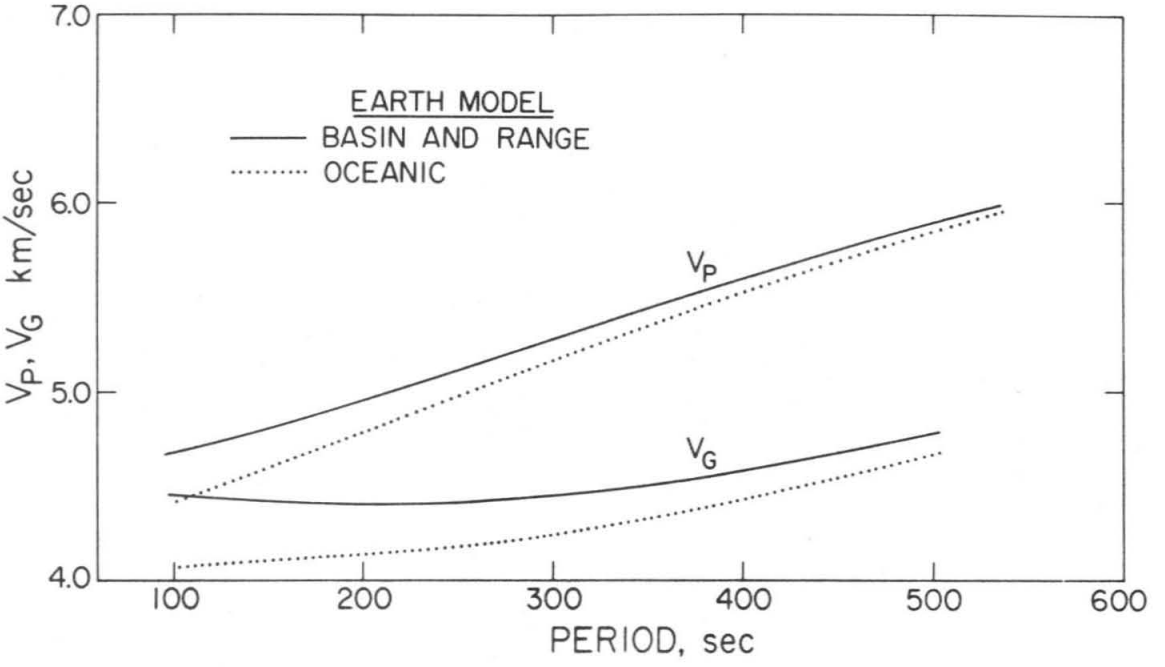

Figure II-3-7. Love wave phase velocity, V_P, and group velocity, V_G, as calculated from the two Earth elastic models used in the perturbation calculations.

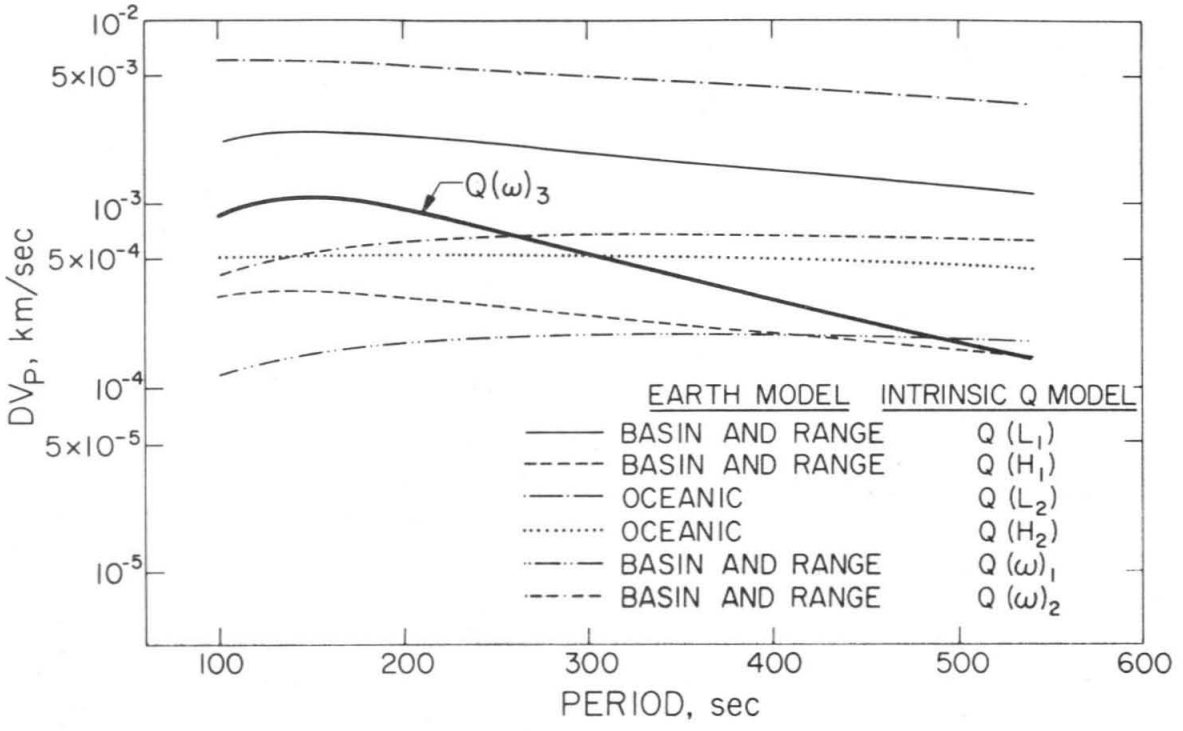

Figure II-3-8. Shift in Love wave phase velocity, DV_P, due to anelasticity calculated from various Earth Elastic and intrinsic Q models.

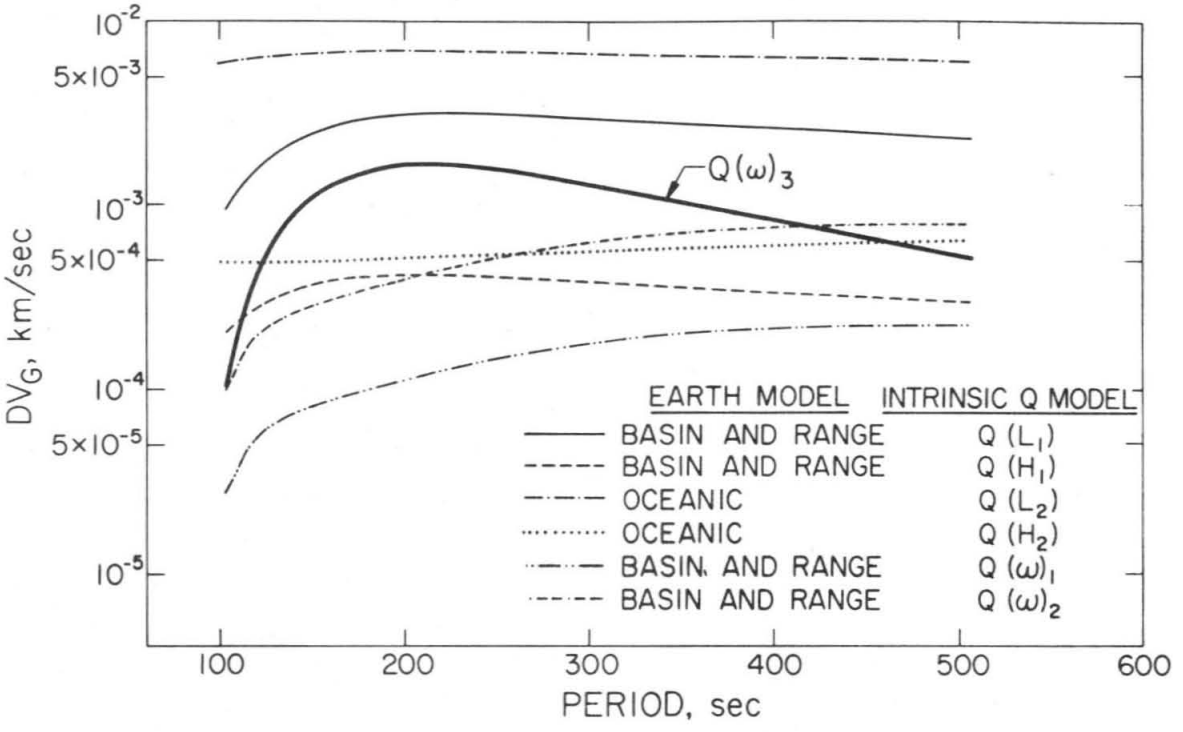

Figure II-3-9. Shift in Love wave group velocity, DV_G, due to anelasticity calculated from various Earth elastic and intrinsic Q models.

4. Discussion

The range of toroidal oscillations for which the maximum percentage period shift occurs depends on the Earth elastic and intrinsic Q-structure model, but in general it is controlled by the low velocity zone where anelastic behavior is an outstanding feature. This is apparent in Table II.3-5, where the longest period (calculated from various Earth elastic and intrinsic Q models) at which the maximum percentage shift occurs is 261.68 seconds. The period at which the maximum percentage shift occurs is 144.59 seconds for the most representative Q model, $Q(\omega)_3$. The longer period free oscillations of ${}_oT_\ell$ have most of their displacement field outside of the low velocity zone. For much shorter period free oscillations ${}_oT_\ell$, the displacement field does not sample much of the low velocity zone.

The maximum percentage shift in Table II.3-5 is -1.31×10^{-3} for an Oceanic Earth model with a slightly extreme intrinsic Q model, $Q(L_1)$. The maximum percentage shift for the more representative intrinsic Q structure, $Q(\omega)_3$, on a Basin and Range Earth model is -2.30×10^{-4}. Are percentage shifts of these magnitudes resolvable from observation? Dziewonski and Gilbert (1972) recently determined the free oscillation periods excited by the 1964 Alaskan earthquake. The resolution of the fundamental toroidal modes ${}_oT_\ell$ reported by them varies between 0.031% and 0.262%, and is generally about 0.1% for the higher frequency toroidal modes ${}_oT_\ell$ at which the anelastic shift becomes important. This kind of resolution, although comparable to the maximum percentage period shift produced by the slightly extreme Q-model,

$Q(L_1)$, is generally five times larger than the maximum percentage period shift produced by the more representative Q-model $Q(\omega)_3$. It is therefore not necessary to correct for anelastic effects for free oscillation periods at the present level of observational accuracy.

The observed free oscillation spectrum generally consists of multiplets in individual modes because the degeneracy in mode number m of ${}_kT_\ell^m$, present for a spherical, nonrotating and laterally homogeneous Earth model, is removed for free oscillation of the real Earth. Data in Dziewonski and Gilbert (1972) are average periods of these multiplets. How does the percentage period shift due to anelasticity compare with the effect of ellipticity, rotation, and lateral heterogeneity? Dahlen (1968) calculated up to ${}_0T_{10}$ for ellipticity and rotational effects. The percentage shifts in period of the central line of the multiplet (m=0) due to ellipticity alone ${}_n\alpha_\ell^e\varepsilon_a$, as calculated by Dahlen (1968), are plotted on Figure II.3-6 together with percentage shifts caused by anelasticity. The trend shows that at modes where anelasticity effects are important, the effect of ellipticity alone on the shift in period of the central line of the multiplet (m=0) is less than the anelastic effects (model $Q(\omega)_3$). The rotational effect, considered alone, does not produce any period shift in the central line (m=0). When rotation and ellipticity are considered together, the effects couple and the total effects are one order of magnitude larger than those produced by anelasticity model $Q(\omega)_3$ (Dahlen 1968; Luh 1973). Luh (1973) calculated the free oscillation modes of an Earth model which includes ellipticity, rotational effects and continent-ocean lateral inhomogeneity. The

effect of the continent-ocean lateral heterogeneity alone is larger by an order of magnitude than the effect of anelasticity model $Q(\omega)_3$ at modes where anelastic effects are important.

The numerical calculation of the present study is carried out only for toroidal oscillations of the Earth. Two reasons are responsible. Firstly, toroidal oscillations do not involve gravity. As a consequence the numerical calculation is simpler for toroidal modes than for spheroidal modes. Secondly, the anelastic effect is more pronounced for toroidal modes than for spheroidal modes. This is because toroidal oscillations involve shear motion only for which seismic dissipation is most effective. However, Dziewonski and Gilbert (1972) reported that the observational accuracy of spheroidal free oscillation periods are generally two orders of magnitude higher than those of the toroidal modes. This can be understood at least partially from the fact that spheroidal modes have higher quality factor than the toroidal modes. It is therefore important to calculate the shifts in free oscillation periods for spheroidal modes, which probably have the same relative importance as for the toroidal free oscillations.

REFERENCES

Alsop, L. E., G. H. Sutton, and M. Ewing, Measurement of Q for very long period free oscillations, J. Geophys. Res. 66, 2911-2915 (1961).

Alterman , Z., H. Jarosch, and C. L. Pekeris, Oscillations of the Earth, Proc. R. Soc. A252, 80-95 (1959).

Anderson, D. L., and C. B. Archambeau, The anelasticity of the Earth, J. Geophys. Res. 69, 2071-2084 (1964).

Archambeau, C. B., E. A. Flinn and D. G. Lambert, Fine structure of the upper mantle, J. Geophys. Res. 74, 5825-5865 (1969).

Backus, G. E., Converting vector and tensor equations to scalar equations in spherical coordinates, Geophys. J. R. Astr. Soc. 13, 71-101 (1967).

Bath, M. and A. Lopez-Arroyo, Attenuation and dispersion of G waves, J. Geophys. Res. 67, 1933-1942 (1962).

Bullen, K. E., An Introduction to the Theory of Seismology, p. 238, third edition, Cambridge Univ. Press, Cambridge, 1965.

Dahlen, F. A., The normal modes of a rotating elliptical Earth, Geophys. J. R. Astr. Soc. 16, 329-367 (1968).

Dziewonski, A. M. and F. Gilbert, "Observation of normal modes from 84 recordings of the Alaskan earthquake of 1964 March 28, Geophys. J. R. Astr. Soc. 27, 393-446 (1972).

Gordon, R. B. and C. W. Nelson, Anelastic properties of the Earth, Rev. Geophys. 4, 457-474 (1966).

Gutenberg, B., Dispersion und Extinktion von seismischen Oberflachenwellen und der Aufbau der obersten Erdschichten, Physik. Z. 25, 377-381 (1924).

Jackson, D.D., Elastic relaxation model for seismic wave attenuation in the Earth, Phys. Earth Planet. Interiors 2, 30-34 (1969).

Jackson, D.D. and D. L. Anderson, Physical mechanisms of seismic-wave attenuation, Rev. Geophys. and Space Phys. 8, 1-63 (1970).

Luh, P.C.H., The normal modes of the rotating, self-gravitating, inhomogeneous Earth, Ph.D. thesis, University of California, San Diego, 1973.

MacDonald, G.J.F., Calculations on the thermal history of the Earth, J. Geophys. Res. 64, 1967-2000 (1959).

MacDonald, G.J.F., and N. F. Ness, A study of the free oscillations of the Earth, J. Geophys. Res. 66, 1865-1912 (1961).

Minster, J. B., and C. B. Archambeau, Thermal models of the Earth, Paper presented at Heat Flow Symposium of I.U.G.G., Moscow, USSR, August 1971.

Nowroozi, A. A., Measurement of Q values from the free oscillations of the Earth, J. Geophys. Res. 73, 1407-1415 (1968).

Press, F., Long-period waves and free oscillations of the Earth in Research in Geophysics, Vol. 2, Solid Earth and Interface Phenomena, pp. 1-26, The M.I.T. Press, Cambridge, 1964.

Press, F., A Ben-Menaham and M. N. Toksöz, Experimental determination of earthquake fault length and rupture velocity, J. Geophys. Res. 66, 3471-3485 (1961).

Saito, M., Theory for the elastic-gravitational oscillation of a laterally heterogeneous Earth, J. Phys. of the Earth (Japan) 19, 259-270 (1971).

Satô, Y., Attenuation, dispersion, and the waveguide of the G waves, Bull. Seis. Soc. Amer. 48, 231-251 (1958).

Savarenskii, E. F., I. L. Nersesov, R. M. Karmaleeva, Observations of long period waves of the Aleutian earthquake of 4 February 1965 recorded by quartz extensometers, Izv. Earth Physics 5, 33-42 (1966) (translation).

Smith, S. W., An investigation of the earth's free oscillation, Ph.D. thesis, California Institute of Technology, 1961.

Solomon, S. C., Seismic-wave attenuation and partial melting in the upper mantle of North America, J. Geophys. Res. 77, 1483-1502 (1972).

Wilson, J. T., The Love waves of the south Atlantic earthquake of August 28, 1933, Bull. Seis. Soc. Amer. 30, 273-301 (1940).